



1-1-2014

# Selection and Evaluation of a Silver Nanoparticle Imaging Agent for Dual-Energy Mammography

Roshan Anuradha Karunamuni

University of Pennsylvania, [r.karunamuni@gmail.com](mailto:r.karunamuni@gmail.com)

Follow this and additional works at: <http://repository.upenn.edu/edissertations>

 Part of the [Biomedical Commons](#)

---

## Recommended Citation

Karunamuni, Roshan Anuradha, "Selection and Evaluation of a Silver Nanoparticle Imaging Agent for Dual-Energy Mammography" (2014). *Publicly Accessible Penn Dissertations*. 1326.  
<http://repository.upenn.edu/edissertations/1326>

This paper is posted at ScholarlyCommons. <http://repository.upenn.edu/edissertations/1326>  
For more information, please contact [libraryrepository@pobox.upenn.edu](mailto:libraryrepository@pobox.upenn.edu).

---

# Selection and Evaluation of a Silver Nanoparticle Imaging Agent for Dual-Energy Mammography

## Abstract

Over the past decade, contrast-enhanced (CE) dual-energy (DE) x-ray breast imaging has emerged as an exciting, new modality to provide high quality anatomic and functional information of the breast. The combination of these data in a single imaging procedure represents a powerful tool for the detection and diagnosis of breast cancer. The most widely used implementation of CEDE imaging is k-edge imaging, whereby two x-ray spectra are placed on either side of the k-edge of the contrast material. Currently, CEDE imaging is performed with iodinated contrast agents. The lower energies used in clinical DE breast imaging systems compared to imaging systems for other organs suggest that an alternative material may be better suited. We developed an analytical model to compare the contrast of various elements in the periodic table. The model predicts that materials with atomic numbers from 42 to 52 should provide the best contrast in DE breast imaging while still providing high-quality anatomical images. Upon consideration, silver was chosen for more detailed study. Through simulation and experimental validation, we determined that not only does silver perform better than iodine when imaged at their respective optimal conditions, but silver is able to provide higher levels of contrast than iodine when imaged with current protocols that are optimal for iodine. Therefore, a silver agent could be translated to the clinic without modification of existing imaging systems or techniques. A prototype silver agent was designed. The agent consists of (i) a silver core for DE contrast, (ii) a silica shell to prevent the release of toxic silver cations, and (iii) a polyethylene glycol layer to improve the biocompatibility of the entire nanostructure. DE imaging with the particles showed a 9-fold increase in contrast when injected into mice, while displaying no acutely toxic effects. The prototype silica-silver nanoparticles represent a first step in developing a biologically stable contrast agent that is specifically suited for DE breast imaging.

## Degree Type

Dissertation

## Degree Name

Doctor of Philosophy (PhD)

## Graduate Group

Bioengineering

## First Advisor

Andrew D. Maidment

## Keywords

dual-energy, mammography, nanoparticle, silver

## Subject Categories

Biomedical

**SELECTION AND EVALUATION OF A SILVER NANOPARTICLE IMAGING  
AGENT FOR DUAL-ENERGY MAMMOGRAPHY**

Roshan Karunamuni

A DISSERTATION

in

Bioengineering

Presented to the Faculties of the University of Pennsylvania

in

Partial Fulfillment of the Requirements for the

Degree of Doctor of Philosophy

2014

Supervisor of Dissertation:

---

Andrew D.A. Maidment, Ph.D.

Associate Professor of Radiology

Graduate Group Chairperson:

---

Jason A. Burdick, Ph.D.

Professor of Bioengineering

Dissertation Committee:

Andrew Tsourkas, Ph.D.

Associate Professor of Bioengineering

Jim Delikatny, Ph.D.

Associate Professor of Radiology

David Cormode, Ph.D.

Assistant Professor of Radiology

## **ABSTRACT**

### **SELECTION AND EVALUATION OF A SILVER NANOPARTICLE IMAGING AGENT FOR DUAL-ENERGY MAMMOGRAPHY**

Roshan Karunamuni

Andrew D.A. Maidment, Ph.D.

Over the past decade, contrast-enhanced (CE) dual-energy (DE) x-ray breast imaging has emerged as an exciting, new modality to provide high quality anatomic and functional information of the breast. The combination of these data in a single imaging procedure represents a powerful tool for the detection and diagnosis of breast cancer. The most widely used implementation of CEDE imaging is k-edge imaging, whereby two x-ray spectra are placed on either side of the k-edge of the contrast material. Currently, CEDE imaging is performed with iodinated contrast agents. The lower energies used in clinical DE breast imaging systems compared to imaging systems for other organs suggest that an alternative material may be better suited. We developed an analytical model to compare the contrast of various elements in the periodic table. The model predicts that materials with atomic numbers from 42 to 52 should provide the best contrast in DE breast imaging while still providing high-quality anatomical images. Upon consideration, silver was chosen for more detailed study. Through simulation and experimental validation, we determined that not only does silver perform better than iodine when imaged at their respective optimal conditions, but silver is able to provide higher levels of contrast than iodine when imaged with current protocols that are optimal for iodine. Therefore, a silver agent could be translated to the clinic without modification of existing imaging systems or techniques. A prototype silver agent was designed. The agent consists of (i) a silver core for DE contrast, (ii) a silica shell to prevent the release of toxic silver cations, and (iii) a polyethylene glycol layer to improve the biocompatibility of the entire nanostructure. DE imaging with the particles showed a 9-fold increase in contrast when injected into mice, while displaying no acutely toxic effects. The prototype silica-silver nanoparticles represent a first step in developing a biologically stable contrast agent that is specifically suited for DE breast imaging.

## TABLE OF CONTENTS

<b>ABSTRACT.....</b>	<b>ii</b>
<b>LIST OF TABLES .....</b>	<b>vi</b>
<b>LIST OF ILLUSTRATIONS.....</b>	<b>vii</b>
<b>CHAPTER 1 .....</b>	<b>1</b>
1. HISTORICAL PERSPECTIVE .....	1
1.1 Non K-edge Imaging .....	1
1.2 K-edge Imaging .....	3
1.3 Current K-edge imaging in Mammography .....	6
2. INDUSTRIAL INNOVATION.....	8
3. CLINICAL IMPACT .....	11
4. COMMERCIAL CONTRAST AGENTS .....	15
5. ALTERNATIVES TO IODINE CONTRAST AGENTS .....	20
6. PREFACE TO DISSERTATION .....	22
<b>CHAPTER 2 .....</b>	<b>24</b>
ABSTRACT .....	24
1. INTRODUCTION.....	25
2. METHODS .....	28
2.1. Formulation of DE Signal Intensity.....	28
2.2. Calculation of Weighting Factor, Contrast and Contrast to Noise Ratio.....	29
3. RESULTS .....	31
3.1. Energy Dependence of W, S <sub>C</sub> , and CNR.....	31
3.2. Maximum CNR for each material .....	35
3.3. Candidate contrast materials for CEDE breast imaging .....	37
4. DISCUSSION .....	39
5. CONCLUSIONS .....	41
<b>CHAPTER 3 .....</b>	<b>42</b>
ABSTRACT .....	42
1. INTRODUCTION.....	43

2.	METHODS .....	46
2.1.	Development of simulation algorithm .....	46
2.2.	Calculation of W and SDNR .....	47
2.3.	Validating the Simulation Algorithm .....	48
2.4.	Comparing SDNR between Ag and I .....	50
3.	RESULTS .....	51
3.1.	Simulation .....	51
3.2.	Validating the Simulation Algorithm .....	60
3.3.	Comparing SDNR between Ag and I .....	62
4.	DISCUSSION .....	64
5.	CONCLUSION .....	68
<b>CHAPTER 4.....</b>		<b>70</b>
ABSTRACT .....		70
1.	INTRODUCTION.....	71
2.	METHODS .....	74
2.1	Synthesis of silver core .....	74
2.2	Silica encapsulation of silver core .....	74
2.3	PEG-stabilization of silica-silver nanoparticles .....	75
2.4	Pharmacokinetic / Biodistribution study .....	75
2.5	DE imaging of mice using PEG-SiAg .....	76
3.	RESULTS .....	77
3.1	Characterization of nanoparticles.....	77
3.2	Blood Clearance / Biodistribution.....	78
3.3	DE imaging of mice – Subcutaneous .....	79
3.4	DE imaging of mice – Intraperitoneal.....	81
4.	DISCUSSION .....	83
<b>CHAPTER 5.....</b>		<b>87</b>
1.	THEORETICAL MODELING .....	87
1.1.	CNR vs. atomic number .....	87
1.2	Limitations of monoenergetic modeling.....	89
2.	TESTING SILVER IN CLINICAL SYSTEM.....	90
2.1	SDNR of silver vs. iodine.....	90
2.2	Limitations of current model .....	93

3. PROTOTYPE SILVER CONTRAST AGENT .....	95
3.1 Testing of silica-silver nanoparticles in mice.....	95
3.2 Proposed redesigns of prototype silver agent.....	97
<b>APPENDIX.....</b>	<b>101</b>
<b>REFERENCES.....</b>	<b>138</b>

## LIST OF TABLES

<b>Table 1.</b> <i>BIRADS categorization of lesions.</i> .....	12
<b>Table 2.</b> <i>Commercially-available iodinated contrast agents. The compound name, ionicity, iodine content and quantitative description of osmolarity are tabulated for four compounds.</i> .....	16
<b>Table 3.</b> <i>Potential contrast materials for DE breast radiography. The materials are listed with their atomic number, maximum <math>S_C</math> (DE contrast), improvement over iodine and current nanoparticle-based research. The improvement over iodine is calculated as the as ratio of the maximum SC of the contrast material to that of iodine. Current nanoparticle-based research applications for each material are also listed.</i> .....	38
<b>Table 4.</b> <i>Values of parameters used in the simulation algorithm</i> .....	46
<b>Table 5.</b> <i>Representative spectral pairs that were chosen to validate the simulation results. They consist of a mixture of LE, HE kV combinations, filter materials and LE dose fraction.</i> .....	49
<b>Table 6.</b> <i>Optimal combinations of parameters to maximize SDNR of silver at breast thicknesses from 2 to 8 cm. The LE kV is maintained at 26 kV, while the HE kV and LE dose fraction is increased as the breast thickness increases.</i> .....	58
<b>Table 7.</b> <i>The optimal imaging conditions to maximize SDNR for iodine identified by the simulation algorithm. Where different, the values used by Hologic are presented in parentheses.</i> .....	58



## LIST OF ILLUSTRATIONS

<b>Figure 1.</b> Depiction of the k-edge in $\mu$ of various materials. The attenuation coefficients of iodine, copper, and water are plotted for energies ranging from 5 to 50 keV. The k-edges of iodine and copper occur at 33 and 9 keV respectively. Due to water's low effective atomic number compared to copper and iodine (7.42 vs. 29 and 53, respectively), the k-edge of water lies outside of this range of energies. ....	4
<b>Figure 2.</b> Hologic DE x-ray breast imaging system installed at the Hospital of the University of Pennsylvania in Philadelphia, USA. ....	10
<b>Figure 3</b> Chemical structure of 4 commercially available iodinated contrast agents, listed in Table 2. ....	17
<b>Figure 4.</b> 2-dimensional attenuation coefficient (2DAC) maps at (20, 25) keV. The blue line represents the breast glandularity values (from 0% glandular (G) to 100% glandular), while the red squares corresponds to materials with atomic numbers from 1 to 80. K-edge imaging positions two spectra so that the contrast material is removed from the breast glandularity values in the 2DAC map. ....	26
<b>Figure 5.</b> 2-dimensional attenuation coefficient (2DAC) maps at (30, 35) keV. The blue line represents the breast glandularity values (from 0% glandular (G) to 100% glandular), while the red squares corresponds to materials with atomic numbers from 1 to 80. K-edge imaging positions two spectra so that the contrast material is removed from the breast glandularity values in the 2DAC map. ....	27
<b>Figure 6.</b> $W$ calculated for energy combinations ranging from 15 to 50 keV. $W$ ranged from 0 to 1, while steadily increasing towards the diagonal of the plot. $W$ increases as the low- (LE) and high (HE) energies are closer together. ....	31
<b>Figure 7.</b> Energy dependence of the linear attenuation coefficients of glandular, adipose tissue, as well as the difference between these two materials (Glandular – Adipose). ....	32
<b>Figure 8.</b> Energy dependence of $S_C$ for (a) Molybdenum, (b) Silver, (c) Iodine, and (d) Gold. $S_C$ is only greater than 0 when the LE and HE bracket the k-edge of the material ....	33
<b>Figure 9.</b> $S_C$ of iodine as a function of the HE and LE for energy pairs that bracket the k-edge (33 keV). ..	34
<b>Figure 10.</b> Energy dependence of CNR for (a) molybdenum, (b) silver, (c) iodine, and (d) gold for a dose distribution of 50% to LE. ....	35
<b>Figure 11.</b> Overlay of the maximum CNR and corresponding dose distribution for materials with Z ranging from 1 to 80. ....	36
<b>Figure 12.</b> Overlay of the optimal weighting factor leads to the maximum CNR (from Figure 11) and the corresponding dose fractions to the LE. ....	37
<b>Figure 13</b> Experimental setup for determining $W$ . Adipose- or glandular-equivalent CIRS materials were placed on a lead sheet with a hole and imaged under geometric magnification. ....	50
<b>Figure 14.</b> Surface plot of $W$ as a function of the mean energy of the LE and HE spectra. The fitted surface is shown alone for better visibility. $W$ is greatest when the two spectra are closest together and the least when the spectra are the furthest apart. ....	52

<b>Figure 15.</b> The effect of breast thickness on $W$ . In this example, a 46 kV HE beam with copper filtration was paired with a 26 kV LE beam with rhodium filtration at a LE dose fraction of 40%. $W$ increases as the breast thickness increases due to beam hardening.....	53
<b>Figure 16.</b> Box plot of SDNR for the various LE filter materials chosen in the simulation algorithm (aluminum, rhodium, and silver). The maximum SDNR is slightly greater for the higher Z filter materials (rhodium, silver) compared to aluminum. The box plots represent data spanning multiple energy pairs, breast thicknesses, and dose fractions.....	54
<b>Figure 17.</b> Box plot of SDNR for the various dose distributions to the LE image. SDNR decreases with increasing dose to the LE image. The box plots represent data spanning multiple energy pairs, filter combinations, and breast thicknesses.....	55
<b>Figure 18.</b> Box plot of SDNR per square root MGD for the breast thicknesses from 2 to 8 cm. Across the range of breast thickness values, the SDNR decreases by 67%. The box plots represent data spanning multiple energy pairs, filter combinations, and dose fractions .....	56
<b>Figure 19.</b> Box plot of SDNR for the breast thicknesses from 2 to 8 cm. As the thickness increases from 2 to 8 cm, the SDNR decreases by 36%. The box plots represent data spanning multiple energy pairs, filter combinations, and dose fractions .....	57
<b>Figure 20.</b> Comparison of simulated SDNR per square root MGD between silver and iodine at breast thicknesses between 2 and 8 cm. Silver performs better than iodine at their respective optimal conditions for every thickness studied. Moreover, silver performed better than iodine when imaged using the optimal conditions for iodine.....	59
<b>Figure 21.</b> The experimentally-obtained values of $W$ are highly correlated with the simulated values. A Pearson correlation coefficient of 0.89 was calculated for the two data sets. Error bars indicate standard deviation.....	61
<b>Figure 22.</b> The experimentally-obtained values of SDNR correlate well with the simulated values. A Pearson correlation coefficient of 0.93 was obtained between the two data sets. ....	61
<b>Figure 23.</b> Example of LE, HE, and DE images of the contrast-embedded step-phantom with silver contrast material. The DE subtraction method removes the signal variation that exists in the background steps while maintaining the signal intensity within the contrast material. ....	63
<b>Figure 24.</b> Comparison of SDNR between Ag and I for the optimal imaging parameters at each LE filter material. Ag performs better than I at their respective optimal imaging conditions, as well as the optimal conditions for iodine. The results are for a 3 cm step phantom. ....	63
<b>Figure 25.</b> Design of prototype silver nanoparticle imaging agent. ....	73
<b>Figure 26.</b> TEM micrographs of (a) polyvinylpyrrolidone-coated silver cores, (b) silica-encapsulated silver cores, and (c) polyethylene glycol-silica-silver nanoparticles (PEG-SiAg) .....	77
<b>Figure 27.</b> Blood clearance of PEG-SiAg nanoparticles after intravenous injection into female mice. The particles are rapidly removed from the bloodstream with an initial half-life of 13-17 minutes. Error bars represent standard deviations.....	78

<b>Figure 28.</b> Biodistribution of PEG-SiAg nanoparticles, 24 hours after intravenous injection into female mice. The majority of the particles are located in the liver and spleen, in addition to accumulation in the lymph nodes and pancreas. The remaining organs showed very little uptake of the silver particles. Error bars represent standard deviation. ....	79
<b>Figure 29.</b> LE (a), HE (b), and DE(c) images of the mouse after administration of PEG-SiAg via subcutaneous injection (yellow arrow). ....	81
<b>Figure 30.</b> LE (a), HE (b), and DE (c) images of a mouse after administration of PEG-SiAg via intraperitoneal injection. The contrast from the silver in the DE image allows for the identification and segmentation of various peritoneal organs. ....	82
<b>Figure 31.</b> Progression of the contrast as a result of the PEG-SiAg in the DE images. (a) 5 minutes, (b) 20 minutes, (c) 40 minutes, and (d) 50 minutes post-injection. The outline of the peritoneal organs decreases over time, until very little contrast is observed 50 minutes after the injection of the particles. ....	83
<b>Figure 32.</b> The maximum CNR plotted against the atomic number of contrast material. Theoretical modeling is used to calculate the maximum possible CNR for every material with atomic number ranging from 1 to 80. ....	88
<b>Figure 33.</b> Comparison of SDNR between Ag and I for the optimal imaging parameters at each LE filter material. Ag performs better than Iodine at their respective optimal imaging conditions, regardless of the filter material. In addition, I imaged at the optimal conditions for I performs worse than Ag at those same conditions. ....	93
<b>Figure 34.</b> LE (a), HE (b), and DE(c) images of the mouse after administration of PEG-SiAg via subcutaneous injection (yellow arrow). ....	97
<b>Figure 35.</b> Design of the silver-gold core shell nanoparticle. The nanoparticle is surface stabilized using a heterobifunctional polyethylene glycol (PEG) ligand. The proximal thiol group attaches directly to the gold surface, while the distal unreactive methyl group is to prevent the non-specific attachment of biological compounds. ....	100

## CHAPTER 1

Dual-energy (DE) x-ray breast imaging is a radiographic technique to improve the detectability of objects of interest by suppressing the background signal variation. The linear attenuation coefficient ( $\mu$ ) of the object of interest must differ from that of the surrounding breast tissue in order to be separated successfully. The differences in  $\mu$  can be utilized by obtaining two images of the breast using two separate x-ray spectra. The images are then combined in order to extract information about the object. For instance, dual-energy (DE) x-ray imaging has been used to segment and quantify tumor vasculature containing an iodinated contrast agent<sup>1</sup>. The overlying anatomic structures can be removed thereby improving the detectability of the iodinated vessel.

### 1. HISTORICAL PERSPECTIVE

The origin of DE x-ray breast imaging can be traced to the development of DE techniques for computed tomography (CT)<sup>2-4</sup>. Two schools of thought emerged from this work: k-edge and non-k-edge imaging. Both approaches use the variation in  $\mu$  with energy to visualize materials of interest in a subtracted background. The approaches differ in the criteria used to compare the  $\mu$  of the objects of interest with the background. Here, a summary of each method is presented along with the major contributors to the field.

#### 1.1 Non K-edge Imaging

Non k-edge imaging is attributed to the work of Alvarez and Macovski in 1976<sup>5</sup>. The technique was originally formulated to improve the soft tissue discrimination in computed tomography. In their analysis,  $\mu$  is represented by constants that specify the contribution of the photoelectric effect and Compton scattering to the total linear attenuation coefficient. The photoelectric effect is heavily influenced by the atomic number and thus gives an indication on the composition of an object. The Compton scatter coefficient is dependent on the electron density, and consequently, the mass density of materials. The representative constants can be determined by making several low-resolution measurements using two spectral sources. Lehmann *et al.*<sup>6</sup> applied this technique to projection radiography in 1981. Low- and high-energy images of the object were combined to determine the amounts of basis materials present in the

object. The basis materials were chosen to be aluminum and polymethylmethacrylate (PMMA), as they bracket the range of atomic numbers expected from a clinical examination and can easily be machined for calibration. Anatomic materials, such as water and bone, can be represented by unique vectors in the aluminum and Lucite basis plane. Using this decomposition technique, Lehmann *et al.* were able to synthesize water- and bone-subtracted chest radiographs of a patient. The water-subtracted images show only bone and calcifications, while the bone-subtracted images enhance the airways and soft-tissue lesions.

The applicability of non k-edge imaging to mammography was first demonstrated by Johns *et al.*<sup>7</sup> in 1984<sup>7, 8</sup>. Johns used a general analytic model employing the basis decomposition method of Lehmann *et al.* to minimize patient dose. Non-k-edge imaging subtraction methods were used to increase the detectability of microcalcifications by suppressing the background anatomical signal variation between adipose and glandular tissue. From the analysis, a dose of 0.42 cGy was deemed necessary to achieve a minimum signal difference-to-noise ratio (*SDNR*) of 5 to detect a cubic calcification with a length of 0.02 cm. This dose could be reduced by a factor of almost 3 if the high energy image is smoothed such that its variance was reduced to one-fourth of its unsmoothed value. These findings were tested and validated using experimental measurements on physical phantoms.

A prototype scanning projection radiography system<sup>7, 9</sup> was used to acquire DE images of excised breast tissue samples obtained from reduction mammoplasty. The samples were placed in an isotonic saline solution to prevent degradation of the tissue and to reduce scatter artifacts arising from an air-tissue transition. Since many of the samples did not contain any calcium, a slab of paraffin wax containing bone chips was placed between the x-ray source and the tissue section to simulate embedded calcifications. The optimal values for beam energy, dose, and high-energy image smoothing factor required for calcification detection were validated with experimental measurements. The images of the tissue sections also demonstrated that non-k-edge DE decomposition methods can increase the detectability of calcium deposits when compared to single-energy images. It was concluded that for a given dose, the *SDNR* of the calcification is higher in the single energy image, yet the detectability is lower due to the confounding effect of soft-tissue signal variation. Thus, dual-energy imaging has the ability to improve the detectability of objects at lower values of *SDNR* by removing the signal variation in the background.

In addition to calcium detection, Johns *et al.*<sup>10</sup> used non-k-edge imaging for the characterization of normal and neoplastic breast tissue. Samples of fat, fibrous, and ductal carcinoma tissue were obtained from patients undergoing reduction mammoplasty procedures and imaged using a high purity germanium source and Deltaray M150-60CX constant-potential generator. The linear attenuation coefficient of the tissue types was calculated from these measurements. The coefficients were expressed in terms of the basis sets (aluminum and Lucite) originally proposed by Alvarez and Lehmann<sup>5, 6</sup>. As expected, fat was less attenuating than the other tissue types at every energy studied. While the non-fat tissue types exhibited similar attenuation profiles, ductal carcinoma tissue was found to be slightly more attenuating than normal fibrous tissue. The mean density of each of these tissue types was determined by measuring buoyancy in phosphate-buffered saline solution. The density values for fat, fibrous and ductal carcinoma tissue were found to be 0.93, 1.04, and 1.04 respectively. The mass attenuation coefficients (linear attenuation coefficient normalized by the density) showed similar ordering of the tissue types although the differences were less pronounced at lower energies. The variation in attenuation coefficient was sufficient for the ductal carcinoma tissue to be segmented from the background fat and fibrous tissue. From the analysis, Johns *et al.* were able to conclude that a dual-energy mammography system would require 0.06 cGy to image a 1 cm infiltrating ductal carcinoma at a signal-to-noise ratio of 5.

### 1.2 K-edge Imaging

In spite of these promising results, non-k-edge imaging will not be further investigated in this dissertation. Compared to k-edge imaging, non-k-edge imaging remains computationally expensive and has not generated ongoing interest in the research community. Thus, the remainder of this dissertation will focus on the development of new k-edge imaging techniques.

Whereas non-k-edge imaging focuses on the ratio of photoelectric and Compton scattering, k-edge imaging relies on energy dependent differences in the total attenuation in order to detect an object of interest. K-edge imaging is performed using beam energies just above and below the photoelectric k-shell absorption edge, or k-edge. The k-edge is a sharp discontinuity in the value of  $\mu$  (increase as energy increases), occurring at the k-shell binding energy of the atom. The use of k-edge imaging in DE imaging

can be further illustrated in Figure 1, where the linear attenuation coefficients of iodine, copper, and water are plotted for energies between 5 and 50 keV. The k-edges are highlighted in yellow and represent sudden deviations in an otherwise smooth energy dependence of  $\mu$ . The k-edges of iodine and copper are at 33 and 9 keV, respectively. The location of the k-edge is a unique characteristic of the material and depends solely on the binding energy of the k-shell electrons. Similar edges are observed for other electron shells (l, m, n) but these edges occur at lower energies that are not relevant in radiographic imaging. Low atomic number materials or compounds, such as water, do not possess a k-edge in this energy range, and possess attenuation coefficients that are continuous and monotonically decreasing. The k-edge of materials such as iodine and copper can be used to increase their detectability in a background of materials with a continuous function of  $\mu$  with energy (such as water or tissue).

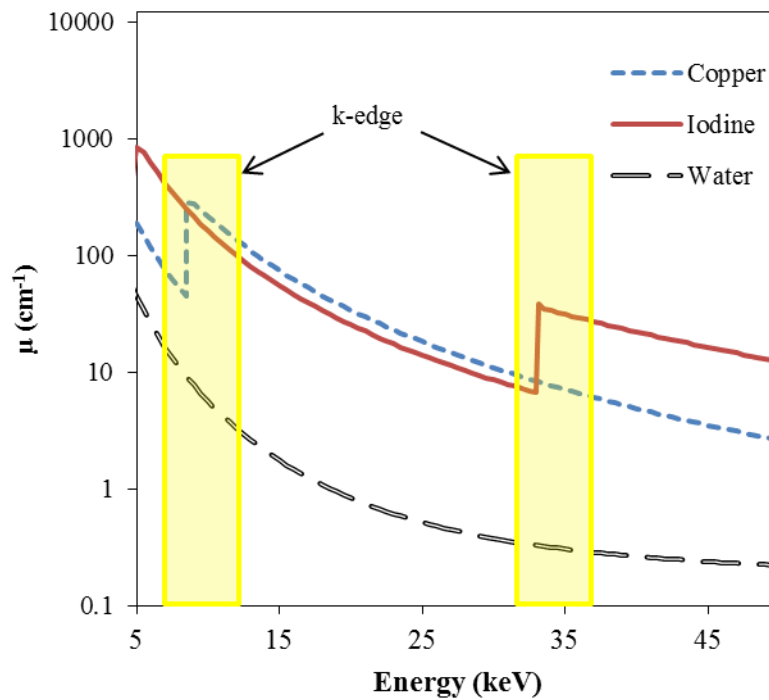


**Figure 1.** Depiction of  $\mu$  of various materials. The attenuation coefficients of iodine, copper, and water are plotted for energies ranging from 5 to 50 keV. The k-edges of iodine and copper occur at 33 and 9 keV respectively. Due to water's low effective atomic number compared to copper and iodine (7.42 vs. 29 and 53, respectively), the k-edge of water lies outside of this range of energies.

The development of k-edge imaging has been attributed to a number of sources. Perhaps the most notable contribution is that of Hounsfield in 1973<sup>11</sup>. He proposed that the iodine concentration in reconstructed CT slices can be estimated quantitatively by subtracting reconstructions made at 100 and 140 kVp. Published soon after, Mistretta *et al.*<sup>12</sup> used image-intensified fluoroscopy to segment iodine, with concentrations as low as 1 mg/cm<sup>2</sup>, from a background of tissue and bone using the Picker thyroid phantom. The phantom is built from PMMA and when filled with iodine, simulates a thyroid scan. The two spectra were obtained by filtering conventional x-ray beams with cerium and iodine to obtain mean energies just above and below the k-edge of iodine. The images were logarithmically subtracted to yield iodine-only images where the background signal variation was adequately suppressed.

Over time, the interest in DE x-ray imaging grew from the chest and abdomen to the breast. In 1989, Chakraborty and Barnes<sup>13</sup> devised a method for the simultaneous acquisition of low- and high-energy images using a theoretical noise analysis model. Instead of switching the x-ray tube voltage, the method relied on exposing an energy sensitive cassette to a constant kV. The cassette consisted of a sandwich of two phosphor plates separated by a copper filter. The front, low-atomic number plate was built from strontium-fluorine-bromine in order to absorb the low-energy x-ray photons while allowing the high-energy photons to pass through. The rear, high atomic number plate was fabricated from barium-fluorine-bromine and designed to absorb the high-energy photons. In this way, the complications involved with kVp-switching such as patient motion and misregistration could be avoided. Boone *et al.*<sup>14, 15</sup> performed a similar theoretical Monte Carlo analysis for optimizing the phosphor plate materials to maximize the signal- to-noise ratio of tissue-embedded microcalcifications. In addition to the combination used by Chakraborty, Boone demonstrated that a yttrium-oxygen-sulfur and gadolinium-oxygen-sulfur phosphor plate combination was effective in DE mammography. Another important discovery from these theoretical calculations was the effect of scatter on DE quantization. Boone found that post-processing scattering techniques can be more useful than mechanical scatter-correction techniques (such as anti-scatter grids) in restoring image quality.



### 1.3 Current *K-edge* imaging in Mammography

As evidenced by the previous examples, the early work in DE x-ray breast imaging was based on theoretical models. The technology required to successfully implement the techniques was not yet available. However, with the recent advancements made in kV-switching x-ray tubes and detector readout times<sup>16–19</sup>, there has been a recent surge in DE research. There are now a multitude of groups from all over the world working on various aspects of DE x-ray breast imaging from optimization of technique parameters to the development of novel x-ray tubes. Carton *et al.*<sup>20–22</sup> published several journal articles on their work on the theoretical and experimental optimization of the visualization of iodine in DE x-ray breast imaging. Carton developed a theoretical model of a DE system whereby the low- and high-energy images are obtained simultaneously using a multi-slit collimator fitted with tin and copper filters. The thickness of these filters was allowed to vary in order to identify the optimal combination. The DE images were obtained using a weighted logarithmic subtraction of the two images. The weighting factor needed to optimally cancel the background anatomical tissue was determined empirically. The weighting factor was found to depend on the filter and breast thickness with values ranging from 0.46 to 0.72. Dose-normalized signal difference to noise ratio (*SDNR*) of iodine was then calculated for the range of filter and breast thicknesses studied. An optimal operating point that maximized the *SDNR* was identified. This point (0.16 mm of tin, 0.23 mm of copper) represents an acceptable tradeoff between the *SDNR*, tube output and dose for all breast thicknesses.

The theoretically-derived optimal conditions were then tested and validated on a prototype XC Mammo-3T (XCounter, Danderyd, Sweden) x-ray breast imaging system. The prototype consisted of the same multi-slit acquisition method using tin and copper filter materials that was simulated in the theoretical model. The choice of filter thicknesses was guided by the theoretical analysis. A structured phantom was designed and built to evaluate the conspicuity of iodinated lesions. The phantom consists of a box filled with various sizes of PMMA spheres and mineral oil. The spheres were designed to simulate a structured background, against which the iodine would be detected. An additional PMMA slab containing embedded disks with known concentrations of iodine was stacked on top of the box. The *SDNR* between the theoretical and experimental values was found to differ by, on average, 1.5%. The theoretical simulation

was able to predict the filter thickness pair that maximized the *SDNR* correctly and optimized the visualization of the embedded iodine disks.

Iordache *et al.*<sup>23</sup> have developed a noise-reduction technique for DE data using a regularized reconstruction method. The method is used to reduce the stochastic noise that arises from the DE subtraction of single-energy images. Iordache employ a regularized simultaneous algebraic reconstruction technique (R-SART) that is constrained for the reconstruction volume and so reduces the noise while preserving the objects of interest. DE Images were obtained on a Senographe DS-based prototype DE image acquisition system (GE, Fairfield, CT, USA). A digital subtraction angiography (DSA) phantom was used to test the effectiveness of the R-SART technique to improve the visibility of iodinated lesions. The DSA phantom consists of a 2.4 cm block of PMMA with embedded disks of varying concentration of iodine. The total thickness of the phantom was increased to 5 cm by using blocks of 50% glandular equivalent CIRS material. The regularization method was shown to increase the *SDNR* of the embedded iodine by 138%. The clinical images were obtained from a pilot study that was run in which patients were injected with iodine at a dose of 320 mg of iodine/kg of bodyweight. The patient used for this study presented a 13 x 6 mm invasive ductal carcinoma with significant iodine uptake. The *SDNR* of the lesion increased by 100% when the R-SART method was applied. Iordache postulated that R-SART could be used to improve the conspicuity of iodinated lesions and characterize iodine uptake.

Fredenberg *et al.*<sup>24</sup> have performed a systematic evaluation of a recently-developed silica (Si)-strip detector for photon counting in DE x-ray breast imaging. The Si-strip detector was recently employed in a photon-counting scanned multi-slit mammography acquisition system that was commissioned for clinical trials by the European Union. The detector is able to separate the incoming photons into 2 separate bins (low- and high-) according to their energy. The images from these bins can be subtracted digitally via weighted logarithmic subtraction to yield DE images. The DE technique was tested using a PMMA phantom consisting of PMMA spheres suspended in mineral oil. An additional PMMA slab with disks of known iodine concentration was then used to simulate embedded iodine lesions. The technique was used to visualize iodine areal concentrations as low as 1.5 mg/cm<sup>2</sup> in the physical phantom. Fredenberg identified several improvements that could be made to the detector so as to improve its application in DE imaging.

One such improvement was to separate charge-shared photons into a third bin that was not used for the DE processing but reserved solely for contributing to the transmission images. Currently, the charge-shared photons are counted in the high-energy bin, regardless of their energy. Through analytic modeling, Fredenberg postulated that by making straightforward changes such as these, they could achieve a 38% increase in the *SDNR* of the iodinated disks.

Chen *et al.*<sup>25</sup> developed and tested an algorithmic method to correct for the degradation of the DE signal that arises from scatter. The algorithm is based on the DE formulation of signal intensity developed by Lemacks *et al.*<sup>26</sup>. Using this method, Chen was able to express the scatter in DE as a function of the transmitted and reference signal intensities which could further be broken down into the linear attenuation coefficients of adipose, glandular and calcium. A sample of *N* pixels was taken in the low- and high-energy images and divided into two sets of independent and dependent measurements. The scatter in the dependent pixels could then be expressed in terms of the independent pixels. Once the *N* simultaneous equations were solved, with appropriate constants, the scatter fields of the low- and high-energy images could be obtained. The algorithmic method for the estimation of scatter was compared to the pinhole-array interpolation method described by Kappadath *et al.*<sup>27</sup>. Kappadath used a lead sheet containing an array of pinholes to obtain spot measurements of the primary beam of x-rays at various locations in the field of view. From these measurements, the scattered radiation at the spot locations can be inferred. The scatter signal in the entire field of view is estimated by fitting a smooth surface to the spot measurements. Although the pinhole method has been shown to remove the confounding effects of scatter in DE imaging, the technique requires extra exposures and is impractical for use in the clinical. Chen found that the estimate of signal intensity between their algorithmic and the pinhole interpolation methods were identical, to within one standard deviation. By reducing the variation in the DE background signal, Chen showed that the algorithm was able to improve the detectability of calcified objects of interest in the breast.

## **2. INDUSTRIAL INNOVATION**

As previously mentioned, the increase in DE x-ray breast research is a result of the development of the technologies necessary to implement the imaging technique. There are now a number of commercially-available DE x-ray breast imaging systems in the world. For example, Hologic (Bedford,

MA, USA) has developed a commercial DE x-ray digital breast imaging system<sup>28</sup>. The system is capable of acquiring both 2- and 3-dimensional (D) images of the breast using a tungsten target. The 2D acquisition consists of low- and high-energy image of the breast obtained sequentially in a total scan time of 5 seconds. The high-energy image is obtained with a voltage of 49 kV using a copper filter. The low-energy image is acquired with a tube voltage that varies from 25 to 39 kV, depending on the breast thickness (1 to 15 cm). A rhodium filter is used for breast thicknesses up to 7 cm, while a silver filter is used for larger breasts. The mAs for both low- and high-energy images is slowly increased as the thickness of the breast increases to allow for sufficient signal intensity to be recorded by the detector. The total dose for the low- and high-energy images ranges from 1.07 mGy for a 1 cm thick breast to 8.5 mGy for 15 cm thick breast. These values roughly correspond to those used in clinical screening protocols.

The 3D acquisition protocol is still in development and consists of 11 low- and high-images that are interleaved in a total scanning angle of 15°. The total scan time for the 3D acquisition is 7.3 seconds. The low- and high-energy peak voltages are fixed at 32 and 49 kV respectively. A copper filter is used for the high-energy images, while an aluminum filter is used for the low-energy acquisitions. The total dose for the 3D acquisition is similar to the 2D acquisition, ranging from 1.51 mGy for a thickness of 1 cm to 9.24 mGy for a thickness of 15 cm. The detector consists of a 0.5 mm thick selenium (Se) layer. The thickness of the Se was increased from 0.2 mm, used in the standard single-energy acquisition systems, to improve the detection efficiency of the DE system at higher energies.

The DE images are obtained using a logarithmic weighted subtraction between the low- and high-energy images. The weighting factor, “k” is applied to the high-energy image and was experimentally determined using the CIRS (Norfolk, Virginia, USA) Model 20 BR3D Phantom. Hologic have conducted several pilot studies to evaluate the performance of the system. They have demonstrated that DE imaging was able to suppress the anatomic background tissue and enhance iodinated tumors that are otherwise obscured by surrounding fibroglandular tissue in single-energy images. The system is currently in clinical trials at sites throughout the world including the Hospital of the University of Pennsylvania (HUP). An image of the system at HUP is shown in Figure 2.



**Figure 2.** *Hologic DE x-ray breast imaging system installed at the Hospital of the University of Pennsylvania in Philadelphia, USA.*

General Electric (GE, Fairfield, CT, USA) has developed a DE x-ray breast imaging system, named SenoBright Contrast Enhanced Spectral Mammography (CESM)<sup>29</sup>. CESM obtained Food and Drug Administration (FDA) 501(k) clearance in 2011, and is currently in use at major mammography centers in the United States as well as France, Spain, Italy, Belgium, Germany, Austria and Japan. GE envisions that by 2020, more than 1 million women worldwide will be examined annually using SenoBright CESM, leading to more productive diagnosis paths for nearly 250,000 women. Concurrently, Philips have developed a DE prototype system based on the MicroDose L30 (Philips, Amsterdam, Netherlands)<sup>30</sup>. Using the silicon-strip photon-counting detector technology developed by Fredenberg<sup>24, 31</sup>, the low- and high-energy images are acquired in a single acquisition by splitting the energy spectrum of the x-ray beam in the detector. In this way, various energy combinations can be tested in a single acquisition so as to maximize the visualization of an iodinated contrast agent.

### 3. CLINICAL IMPACT

Ultimately, the development of DE x-ray breast imaging in research and industry hinges on the success of the technique to deliver positive patient outcomes in the clinic. Clinical trials have, therefore, been essential in providing the impetus for the continued development of the technology. In 2003, Lewin *et al.*<sup>32</sup> published their results on one of the first pilot studies exploring the feasibility of dual-energy mammography for the detection of primary breast cancers. In total, 26 patients were recruited that either required biopsy or were subjectively determined to have a 50% or more chance of malignancy. Low- and high- energy images of the patients were obtained in the medial lateral oblique (MLO) view. The images were acquired using a DE-modified GE Senographe 2000D digital mammography unit (GE, Fairfield, CT, USA). The low- and high-energy kV pairs were determined experimentally by measuring metrics of contrast in an iodine containing phantom covered with BR-12 breast-equivalent material (CIRS, Norfolk, Virginia, USA). After experimental optimization, the high-energy beam was acquired with a rhodium target at 44 kV, while the low-energy beam was selected as either a molybdenum target at 30 kV or a rhodium target at 33 kV. The DE image was calculated as the weighted, logarithmic subtraction between the low- and high-energy images. The weighting factor was determined by experiment to eliminate the variation in signal intensity of the breast-equivalent material phantom. A weighting factor of 0.2 was chosen for spectral pairs with the low-energy molybdenum beam while a value of 0.26 was chosen for those with the low-energy rhodium beam.

Of the 26 patients in the study, 13 presented with invasive cancers. From these 13 patients, 11 resulted in strong enhancement in the DE images. Contrast-to-noise ratios of the tumor to the surrounding background tissue was calculated to be higher than 2.0. The other 2 patients presenting cancers were moderately-to-weakly enhancing in the DE images and were classified to represent false negatives. Of the remaining 13 patients, 1 patient exhibited ductal carcinoma in situ with a duct that was weakly enhancing in the DE image. The remaining 12 patients had benign findings, in which 2 exhibited diffuse enhancement. These 2 finding represent false positives. Overall, this pilot study helped to demonstrate the feasibility of DE mammography to visualize lesions that are otherwise mammographically occult.

In 2005, Chen *et al.*<sup>28</sup> conducted a DE digital breast tomosynthesis (DBT) pilot study, as part of a larger NCI-funded grant studying multimodality breast imaging. The sampling population consisted of 11 women with BIRADS (Breast Imaging Reporting and Data System) 4 or 5 breast lesions. The BIRADS categorization of masses is listed in Table 1. The images were acquired with a GE Senographe 2000D (GE, Fairfield, CT, USA) that was modified to allow for DE acquisitions. The patients were seated and the imaging system was positioned for medial lateral oblique (MLO) projections. The breasts were rendered immobile through light compression, which was maintained between the pre- and post-contrast data sets.

**Table 1.** *BIRADS categorization of lesions.*

<b>BIRADS category</b>	<b>Description</b>
0	Need additional imaging evaluation or prior mammograms for comparison
1	Negative
2	Benign (non-cancerous) finding
3	Probably benign finding (<2% malignant), initial short-interval follow-up suggested
4	Suspicious abnormality (2- 95% malignant), biopsy should be considered
5	Highly suggestive of malignancy (>95% malignant), appropriate action should be taken
6	Known biopsy – Proven malignancy

Suspicious enhancing lesions were observed using DE DBT for 10 out of the 11 cases of pathologically proven breast cancers. Chen demonstrated that the pre- and post- contrast images obtained with the DE imaging protocol provided localization, morphology and border characteristics of breast lesions that were in agreement with digital mammography. The vascular characteristics of the breast lesions identified by DE DBT were consistent with the vascular information provided by magnetic resonance imaging (MRI). MRI imaging is known to be an extremely sensitive technique for imaging the neovasculature associated with carcinoma and is currently used as the clinical standard at several imaging

centers. However, breast MRI is an expensive, time consuming technique that is not universally available. DE imaging is able to provide high quality blood flow information and spatial information in a single, affordable, readily available imaging modality.

Dromain *et al.*<sup>33</sup> conducted a similar but larger study in 2012, recruiting 110 patients, to compare the diagnostic accuracy of DE mammography as an adjunct to conventional mammography and ultrasound. The images were acquired with a prototype DE image acquisition device developed by GE Healthcare. Two views of the breast (MLO and craniocaudal (CC)) were obtained for each patient. The technique parameters for the DE examination were adjusted so that the average glandular dose to the patient in a single view was comparable to a single-view standard diagnostic mammogram. The readers used in this study consisted of seven experienced breast radiologists from five institutions. The radiologists read the conventional mammogram, ultrasound and DE mammogram images independently, and were blinded to the patient's cancer status.

The use of DE mammography improved the per-lesion specificity across all readers from 0.71 to 0.78. All the readers used in this study recorded improved clinical performance and the average area under the receiver operated characteristic (ROC) curve increased from 0.83 to 0.87. The area under the ROC curve provides a measure of discrimination and quantifies the ability of a test to correctly classify those with and without disease. The increase in the area under the ROC curve implies that DE mammography improved the visibility and differentiation of suspicious findings due to the accurate depiction of tumor angiogenesis. Using a separate analysis, the combination of mammography and DE mammography was compared with that of mammography and ultrasound. The latter combination corresponds to the current clinical practice in the diagnostic setting. The results demonstrated that lesion visibility using a combination of standard and DE mammography was similar or better than the clinical standard in 80% of the cases. DE mammography has the potential to increase breast cancer detection rates, improve staging of cancers, and improve patient selection for biopsy.

In 2013, Jochelson *et al.*<sup>34</sup> reported the results of a pilot study to determine the feasibility of performing bilateral DE mammography. The performance of this technique was compared to that of



conventional mammography and breast MRI for detection of known breast cancers. The DE images were obtained using a GE DS digital mammography unit (GE, Fairfield, CT, USA) that had been upgraded to allow for a low- and high-energy image to be obtained for each view. The voltage was selected based on the breast thickness and glandularity. The low-energy peak voltage varied from 26 to 30 kV while the high-energy voltage varied from 45 to 49 kV. In total, 52 patients were imaged using DE mammography, MRI, and conventional mammography. DE mammography and MRI both depicted 96% of the primary tumors, which was higher than obtained with conventional mammography (81%). The cancers that were missed by DE mammography were not of a particular size, ranging from 1 to 20 mm, with a median of 7 mm. DE mammography was found to be less sensitive than MRI in detecting additional foci of breast cancer. DE mammography identified 7 additional sites of breast cancer compared to the 22 found by MRI. However, DE mammography did result in fewer false positives, indicating a greater specificity compared to MRI. When comparing staging using the two techniques, MRI was able to identify 100% of the patients requiring mastectomy, while DE mammography helped identify 73%.

Froeling *et al.*<sup>35</sup> have also published results to determine the correlation between the contrast agent kinetics observed in MRI using chelated gadolinium contrast agents with that observed in DE DBT using iodinated contrast agents. In total, 21 patients were recruited with BIRADS 4 or 5 breast lesions. Each patient was imaged using conventional mammography, ultrasound, contrast-enhanced MRI and DE DBT. DE DBT was performed using a Philips spectral tomosynthesis prototype based on the Philips MicroDose L30 (Philips, Amsterdam, Netherlands) system. The prototype system is equipped with a 21-row crystalline silicon detector that is capable of splitting the energy spectrum of the incoming x-ray beam into low- and high-energy bins. The DE DBT images were obtained in the MLO view, with the patients sitting upright. The total acquisition time per patient was 15 seconds. The signal-intensity time curves were compared for the MRI and DE DBT techniques. The two modalities showed significant correlation, with a Spearman's rho coefficient of 0.49. These results together with the data presented by Jochelson *et al.*<sup>34</sup> demonstrated that DE DBT could be used as an alternative to contrast-enhanced MRI to deliver information regarding the uptake and washout of contrast agent in tumors.

#### 4. COMMERCIAL CONTRAST AGENTS

Iodine is currently the only contrast material that has been used in clinical studies with DE x-ray breast imaging. Iodinated imaging agents are the most widely used contrast agents in radiography<sup>1, 36–39</sup>. The development, design, and refinement of these agents has continued unabated nearly a hundred years since the first water-soluble iodinated radiographic agents were tested by Swick<sup>40, 41</sup> in 1928. The compound, Iopax (or Uroselectan), was used for intravenous urography and was the first major step in the use of radio-opaque materials to diagnose disease. Although the compound was rapidly removed from circulation by the kidneys, Iopax resulted in side-effects of nausea and vomiting after administration. In 1968, Almen<sup>42</sup> identified the ionicity and osmolarity of the contrast agents as important determining factors in their toxicity. Almen postulated that by preventing the dissociation of the contrast material in solution, the hemodynamic alteration due to the osmotic properties of the compound could be averted. Almen's work with the metrizamide group of contrast agents lead to the development of the compound Amnipaque, which represents the first water soluble, nonionic contrast agent used in radiography.

Swick and Almen's pioneering work has led to the precisely-engineered molecules that are commercially available today. A subset of these compounds are tabulated in Table 2 and their structures are presented in Figure 3<sup>43</sup>. These molecules are typically small tri-iodobenzene compounds with several added substitutions for improved water solubility. Iodinated x-ray contrast agents are chemically inert and resist biological degradation *in vivo* over long periods of time<sup>41</sup>. The compounds display a low affinity to plasma proteins and are excreted without noticeable metabolism, deiodination, or biotransformation<sup>41</sup>. The molecules remain undissociated in the body and are filtered through the kidneys via glomerular filtration<sup>44</sup>.

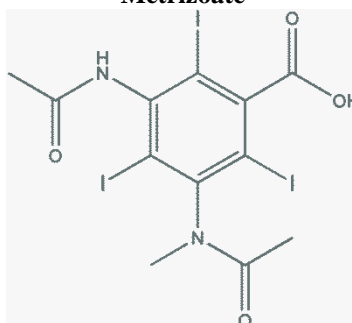
A three-compartment pharmacokinetic model (plasma, extravascular fluid, kidneys) has been widely used to study the effect of a bolus injection of iodinated contrast material. After injection, there is a sharp fall in the plasma concentration of the compound as equilibrium is reached between the vascular and extravascular spaces<sup>45</sup>. Once equilibrium has been reached (roughly 10 minutes after injection), the decrease in plasma concentration is due to filtration by the kidneys and follows an exponential decay. Typically, the greatest enhancement is observed 15 to 120 seconds after the bolus injection<sup>45</sup>. Due to these

rapid clearance times, all of the DE x-ray breast imaging studies mentioned in the previous “Clinical Impact” section were performed within 3 to 4 minutes post-injection.

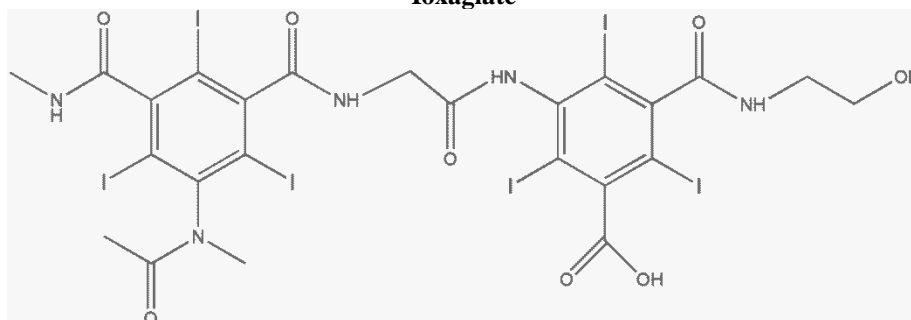
**Table 2.** *Commercially-available iodinated contrast agents. The compound name, ionicity, iodine content and quantitative description of osmolarity are tabulated for four compounds.*

Compound	Type	Iodine Content (mg/mL)	Osmolarity
Metrizoate	Ionic	370	High
Ioxaglate	Ionic	320	Low
Iohexol	Non-ionic	350	Low
Iodixanol	Non-ionic	320	Low

**Metrizoate**



**Ioxaglate**



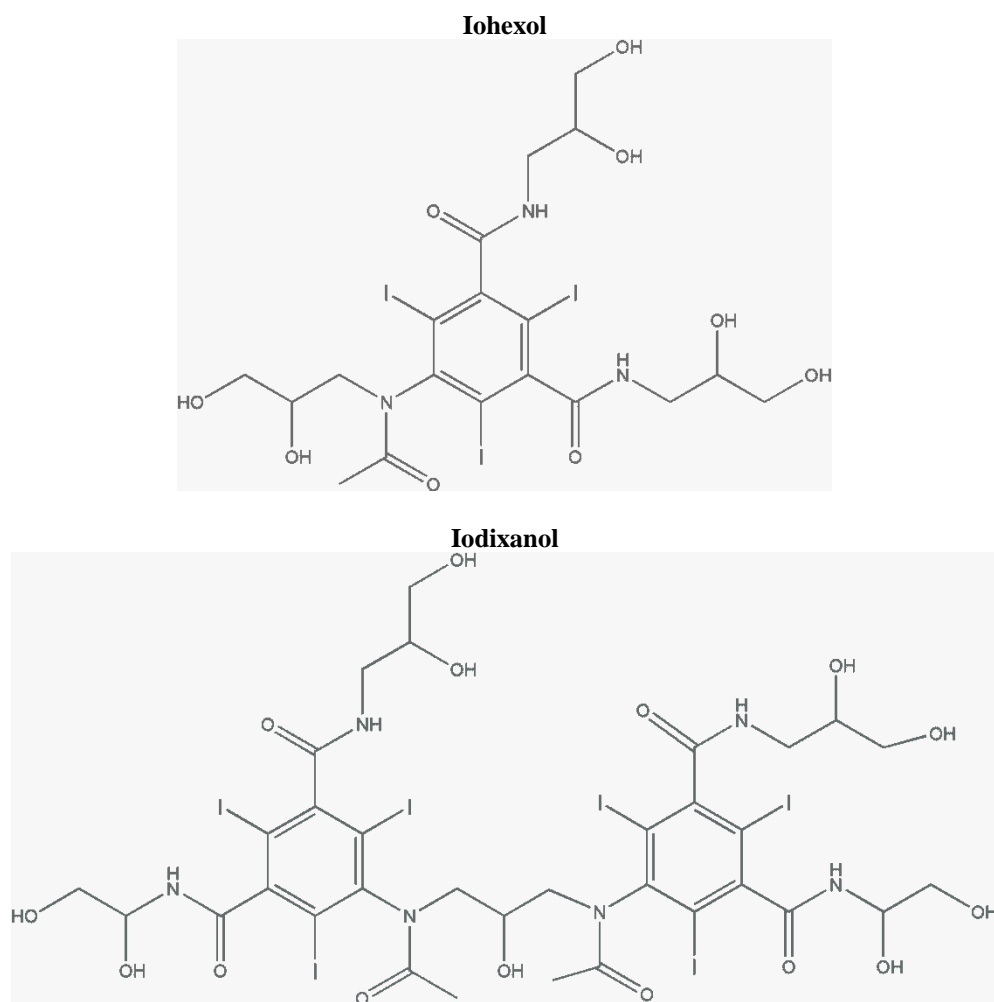


**Figure 3.** Chemical structure of 4 commercially available iodinated contrast agents, listed in Table 2.

Despite their seemingly inert characteristics, iodinated contrast agents have been linked with several adverse effects. The effects can vary from anaphylactic reactions to dose-dependent renal toxicity. Anaphylactic reactions such as acute bronchospasm and profound hypertension may occur with small volumes of contrast material. An exact biochemical mechanism for the anaphylactic reactions has not yet been determined. Acute reactions have been found to occur in 5 to 8% of patients that are administered ionic contrast agents<sup>46</sup>. Many of these reactions are minor; however, severe life-threatening reactions occur with 0.05 to 0.1% of ionic contrast administrations. It is generally accepted that nonionic contrast media cause fewer instances of anaphylactic reactions than their ionic counterparts<sup>47</sup>. Large, multicenter surveillance studies have determined that nonionic contrast material carry five times lower risk of reaction

than ionic material. One of the major groups at risk for these types of reactions is those patients with known histories of allergies. Large population studies have determined that the risk of a contrast-mediated adverse reaction is two to five times higher in patients with known allergies, particularly asthmatics<sup>48</sup>. One such study showed that pediatric patients administered with nonionic contrast material intravenously demonstrated a 0.18% incidence of acute allergic-like reactions<sup>47</sup>. Out of these patients, 25% had a history of asthma. The regular prevalence of asthma in children in the United States is 9%<sup>49</sup>.

In addition, iodinated contrast materials have long been linked with instances of renal failure or contrast-media nephrotoxicity (CMN). CMN is defined as an increase in serum creatinine of more than 25% within 3 days following the administration of the contrast material<sup>50</sup>. CMN is characterized by several functional and structural changes to the renal tubules. The contrast materials interfere with the reabsorption of water and sodium by the renal tubules, resulting in changes in the tubular regulatory mechanisms and intratubular pressure<sup>37, 51</sup>. These changes can trigger the tuboglomerular feedback (TGF) mechanism which in turn leads to a decrease in glomerular filtration rate (GFR) and increase in renal vascular resistance. The TGF feedback mechanism is heightened with high-osmolar contrast material and is responsible for almost 50% of renal dysfunction caused by these compounds<sup>51</sup>.

Low-osmolar contrast materials have been shown to result in structural changes to the cell lining of the renal tubules. The high viscosity of these compounds results in longer periods of time spent in the tubules and greater exposure to the epithelial cells. Increased exposure means that the contrast material is more likely to be actively internalized by the epithelial cells, resulting in lysosomal changes and vacuolization by the cells<sup>52, 53</sup>. Structural changes can also occur in the renal medulla. Interference with sodium transport in this region results in the necrosis of the medullary thick ascending loop of Henle<sup>54</sup>. Apoptosis along the thick ascending loops can be detected as early as 15 minutes after the administration of contrast material<sup>54</sup>.

The incidence of CMN in patient populations varies greatly with existing renal function. In healthy patients, the incidence of CMN varies from 0 to 10%<sup>55</sup>. In patients with pre-existing renal complications, the incidence of CMN jumps to 12 to 27%, as reported by several prospective controlled

studies<sup>56, 57</sup>. In some cases, incidence rates as high as 50% was reported in patients with diabetic nephropathy using low-osmolar contrast media. Renal impairment, especially diabetic nephropathy, prolongs the elimination half-life of the contrast material, leading to longer exposure with damaged kidney tissue. In addition, intra-arterial administration<sup>37, 58</sup> of contrast media has been shown to result in a higher incidence of CMN compared to intravenous injection. Dehydration and cardiac failure have also been identified as potential risk factors for CMN. These can lead to reduced renal perfusion, which in turn increases the exposure of the renal tubules to the contrast material.

As previously mentioned, the average blood half-life of iodinated contrast material is on the order of 30 minutes. The rapid clearance of the contrast material necessitates that large amounts of iodine are injected into the body to ensure sufficient contrast. The large amount of injected contrast material subsequently leads to the unwanted side-effects of CMN. To tackle this shortcoming, several researchers have made efforts to encapsulate the iodinated contrast material within nanoparticle carriers to increase the contrast load (atoms of iodine) per delivery vehicle. Samei *et al.*<sup>59</sup> developed a long-circulating liposomal-based nanoparticle agent as a delivery mechanism for iodinated contrast agents. In their formulation, a lipid mixture of 1, 2-dipalmitoyl-sn-glycero-3-phosphocholine, cholesterol, and 1, 2-distearoyl-sn-glycero-3-phosphoethanolamine N-[methoxy(polyethylene glycol)-2000] is incubated with 370 mg/mL of Iopamidol (Bracco, Italy). The concentration of the encapsulated iodine was measured to be 65 mg/mL. The iodine-loaded liposomes were injected into Fisher mice carrying subcutaneously transplanted samples of tumor tissue from donor rats. The mice were imaged using a small-animal micro-CT scanner. Substantial enhancement was observed in the tumor and a signal difference of 332 Hounsfield units (HU) between the tumor and background was measured. The liposomes also preserved the enhancement of the tumor for up to 4.2 hours after the injection, prolonging the elimination half-life of the iodine molecule.

Bhavane *et al.*<sup>60</sup> used a similar liposomal delivery method to image atherosclerotic plaques in a mouse model using dual-energy computed tomography. The nanoparticle formulation consisted of hydrating liposomes with 400 mg/mL of iodixanol solution. The final concentration of iodine in the liposome encapsulation varied from 32 to 82 mg/mL depending on the hydrophilic surface ligands used to coat the nanoparticle. The liposomes were injected into C57BL/6 mice and imaged using a custom-built

dual source micro-CT scanner. The DE images were acquired using peak voltages of 40 and 80 kV. The DE decomposition method was able to localize the iodinated liposomes within the atherosclerotic plaque and separate this signal from the surrounding tissue.

The stability of the liposomes *in vivo* will need to be further investigated. Leakage of contrast material through the liposomal layer could result in the same CMN toxic effects that are observed with the administration of the conventional iodine agent. Degradation of the liposomal carriers would result in a concentrated delivery of contrast material to the renal tissue which in turn may enhance the effects of CMN. In addition, the loading efficiency of the liposomes ranges from 8 to 20%, resulted in large amounts of wasted material. Methods to increase the efficiency of the formulation of the liposomes will need to be developed before the technique can be scaled up successfully.

## **5. ALTERNATIVES TO IODINE CONTRAST AGENTS**

In light of these limitations, several materials have been investigated as alternatives to iodine for radiographic contrast imaging. Gold is the most promising choice, as evidenced by the numerous groups working on developing gold nanoparticles as CT contrast agents. Hainfeld<sup>61</sup> was the first to image surface-stabilized gold nanoparticles in mice successfully using x-ray imaging. Gold has a higher atomic number than iodine, and should therefore provide better contrast for x-ray imaging. Hainfeld states that gold provides roughly 2.7 times greater contrast per unit weight of material than iodine at an energy of 100 keV. The higher atomic number, and thus higher k-edge, means that gold can be imaged at much higher energies than iodine while still preserving contrast from the surrounding soft tissue. Higher imaging energies reduce interference from bone, and take advantage of lower soft tissue absorption, which in turn reduces patient dose.

Hainfeld injected 1.9 nm spherical gold nanoparticles at a concentration of 270 mg/mL into Balb/C mice. The animals were imaged using a conventional mammography unit. Vascular enhancement was observed within 2 minutes after injection of the nanoparticles. The particles were excreted via the kidneys and the bladder. Little enhancement was observed in the liver or spleen. The renal microvasculature showed large amounts of contrast, with blood vessels as fine as 100  $\mu\text{m}$  easily distinguishable. The animals

were also implanted with subcutaneous tumors consisting of mammary carcinoma cells. The contrast between the tumor and muscle was preserved up to 24 hours after the injection of the particles. These results demonstrated that gold nanoparticles possess blood half-lives several orders of magnitude larger than conventional iodinated contrast agents, while showing no toxic effects.

Hainfeld was also able to conjugate targeting ligands on to the surface of gold nanoparticles<sup>62</sup>. Antibody fragments targeting the extracellular portion of the HER2 receptor were conjugated onto the surface of 15 nm gold nanoparticles. HER2 is a cell surface protein that is over-expressed in 30% of all breast cancers<sup>62</sup>. By conjugating the targeting ligand to the nanoparticle, Hainfeld was attempting to demonstrate the feasibility of using targeted nanoparticles to delineate and type tumors *in vivo*. The nanoparticles were injected intravenously into immunocompromised mice. The mice were subcutaneously injected with either HER2 positive or negative breast cancer cell lines (BT474 or MCF-7). 20 hours after the injection of the nanoparticles, the mice were sacrificed to minimize motion artifacts during the subsequent 40 minute imaging procedure. Hainfeld states that there is no evidence to suggest that euthanization resulted in the redistribution of gold.

The mice were imaged using the Scanco Medical AG  $\mu$ CT40 or Scanco VivaCT 40 micro-CT scanners. All the mice exhibited radiodense peripheries with high concentrations of gold around the tumor. This is to be expected as the periphery of the tumor contains the highest concentration of blood vessels. The gold content of the organs was measured, through a combination of micro-CT and atomic absorption spectroscopy. The amount of gold in the tumors was roughly 22 times higher than in the surrounding muscle. Tumor enhancement was 34% higher in HER2 positive tumors compared to HER2 negative tumors. The enhancement ratio was higher (56%) when considering only the periphery of the tumor instead of the entire volume. The selective absorption of the targeted nanoparticles in HER2 positive tumors suggests that the attachment of the antibody was successful in targeting the nanoparticle against the HER2 surface receptor. Through these results, Hainfeld has demonstrated that micro-CT can be used for the localization of targeted gold nanoparticles. The combination of technique and imaging agent can be used for the delineation of tumor boundaries in surgery, radiotherapy planning, tumor typing and detection of lymph node involvement.



Bismuth has also been investigated as an alternative to iodine for CT imaging. Similar to gold, bismuth (atomic number, 83) has a higher atomic number and therefore higher attenuation coefficient than iodine. Rabin *et al.*<sup>63</sup> were the first to propose the use of polymer-coated bismuth sulfide nanoparticles as intravenous imaging agents in CT. The bismuth-sulfide nanocrystals were grown by reduction of bismuth and sodium citrate in the presence of polyvinylpyrrolidone, which acts as the capping agent. The resulting crystals had a rectangular platelet shape, with dimensions ranging from 10 to 50 nm. 250  $\mu$ L of nanocrystals were injected into Balb/c mice at a bismuth concentration of 114 mg/mL. The vascular system showed immediate enhancement post-injection, as evidenced by the CT number which increased from -27 to 530 HU. The enhancement allowed for clear delineation of the cardiac ventricles and the major arterial and venous structures. In order to achieve the same levels of contrast with iodine, roughly 2.6 times more material would have to be used. The blood half-life of the bismuth-sulfide nanoparticles was found to be 140 minutes, an order of magnitude longer than commercially available iodine imaging agents. In addition, the bismuth-sulfide nanocrystals showed similar toxicity to iodine in animal models. The results helped identify bismuth as an alternative to iodine for CT imaging.

## **6. PREFACE TO DISSERTATION**

While gold and bismuth remain intriguing avenues for high energy diagnostic imaging, their application in DE x-ray breast imaging is limited. The k-edge of these materials lies outside of the mammographic energy range and therefore cannot be used in k-edge DE x-ray breast imaging.

This dissertation describes the development of a contrast agent specialized for DE x-ray breast imaging. The development will include the identification of candidate materials, chemical synthesis and purification of a contrast agent, testing in animal models, and optimization in clinical imaging systems. The research stems from the gap in the literature regarding specialized contrast materials for DE x-ray breast imaging. This work details the framework and methodology needed to design, test and develop a breast-specific DE imaging agent. The dissertation describes the implementation of a silver contrast agent in DE x-ray breast imaging. The subsequent chapters are ordered to reflect this sequence:

Chapter 2: Develop an analytic model to identify candidate materials for DE x-ray breast imaging.

Chapter 3: From the candidate materials, silver was chosen for further evaluation and testing. The contrast of silver was compared to iodine in a clinical DE imaging system. A simulation algorithm was developed to identify the optimal technique parameters for each material so that they could be compared.

Chapter 4: Design, synthesis, and testing of a silver-based nanoparticle contrast agent for *in vivo* applications.

Chapter 5 summarizes the major discussion points and accomplishments accumulated over the course of the dissertation work. In addition, this chapter addresses the limitations, pitfalls, and directions in which this project can be continued.

## CHAPTER 2

### ABSTRACT

Contrast-enhanced (CE) dual-energy (DE) x-ray breast imaging uses a low- and high-energy x-ray spectral pair to eliminate soft-tissue signal variation and thereby increase the detectability of exogenous imaging agents. Currently, CEDE breast imaging is performed with iodinated contrast agents. These compounds are limited by several deficiencies, including rapid clearance and poor tumor targeting ability. The purpose of this work is to identify novel contrast materials whose contrast-to-noise ratio (CNR) is comparable or superior to that of iodine in the mammographic energy range. A monoenergetic DE subtraction framework was developed to calculate the DE signal intensity resulting from the logarithmic subtraction of the low- and high-energy signal intensities. A weighting factor is calculated to remove the dependence of the DE signal on the glandularity of the breast tissue. Using the DE signal intensity and weighting factor, the CNR for materials with atomic numbers ( $Z$ ) ranging from 1 to 79 are computed for energy pairs between 10 and 50 keV.

A group of materials with atomic numbers ranging from 42 to 63 were identified to exhibit the highest levels of CNR in the mammographic energy range. Several of these materials have been formulated as nanoparticles for various applications but none, apart from iodine, have been investigated as CEDE breast imaging agents. Within this group of materials, the necessary dose fraction to the LE image decreases as the atomic number increases. By reducing the dose to the LE image, the DE subtraction technique will not provide an anatomical image of sufficient quality to accompany the contrast information. Therefore, materials with  $Z$  from 42 to 52 provide nearly optimal values of CNR while requiring achievable energy pairs and operating at dose fractions that provide good anatomical images. This work is intended to inspire further research into new materials for optimized CEDE breast functional imaging.

## 1. INTRODUCTION

Contrast-enhanced (CE) dual-energy (DE) x-ray breast imaging encompasses an emerging group of modalities designed to provide quantitative functional information together with high-resolution anatomic images. This unique combination of information in a single imaging procedure represents a powerful breast imaging tool for morphological and vascular characterization of breast lesions<sup>20–22, 28, 33–35</sup>. DE imaging is used to increase the conspicuity of exogenous radiographic imaging agents by suppressing the anatomical signal variation in the body. In the breast, this involves the suppression of the signal variation that arises from differences in soft tissue (adipose and glandular) composition across the breast. By reducing the effect of this soft tissue “anatomical noise”, it is possible to segment and quantify the signal from an exogenous imaging agent. This is performed by using two distinct energy windows (low- and high-) to emphasize the variation in attenuation of the various materials with energy. By employing an imaging agent whose linear attenuation k-edge lies within the energy range used, it is possible to separate the contrast material from the surrounding tissue.

K-edge imaging has been extensively applied in dual-energy radiography to separate high atomic number (Z) contrast materials from surrounding tissue<sup>12, 64, 65</sup>. The concepts of k-edge imaging can be visualized using 2-dimensional attenuation coefficient (2DAC) maps, as shown in Figure 4. The 2DAC maps plot pairs of attenuation coefficients for various materials at a particular combination of energies. The blue solid line is the linear attenuation coefficient of admixtures of adipose and glandular breast tissue ranging from 100% adipose (A) to 100% glandular (G). The red squares represent potential contrast materials with atomic numbers ranging from 1 to 80, with certain materials of interest [molybdenum (*Mo*), silver (*Ag*), iodine (*I*), gold (*Au*)] explicitly shown. Atomic number multiples of 10 are shown to serve as a guide. In general, as the atomic number increases, the attenuation coefficients at both energies increase. The discontinuities in the graph, which are drawn as dashed lines, arise from the fact that the k-edge of the indicated materials fall between the 2 energies. The ability to accurately separate materials at a particular combination of energies can be directly correlated to their distance from the blue A-G line on the 2DAC map. Thus, as the distance between the potential contrast material and the breast tissue values increases, the ability to separate the contrast agent from the anatomical tissue improves. As an example, Figure 4 shows a

2DAC map for an energy pair of (20, 25) keV. All four materials of interest are positioned close to the breast tissue values. However, materials with Z between 43 and 46 are separated from the breast tissue values. When the energy pair is changed to (30, 35) keV as shown in figure 2, materials between 51 and 54, including iodine, are distinct from the breast tissue values. Thus, the latter energy pair is better suited for an iodinated contrast agent than the former, as expected.

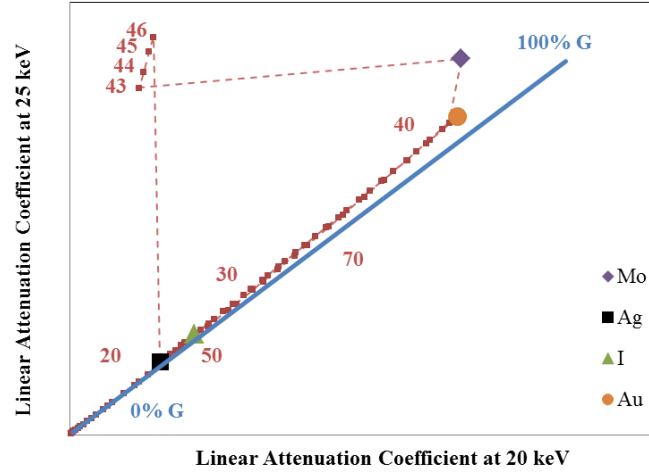


**Figure 4.** 2-dimensional attenuation coefficient (2DAC) maps at (20, 25) keV. The blue line represents the breast glandularity values (from 0% glandular (G) to 100% glandular), while the red squares corresponds to materials with atomic numbers from 1 to 80. K-edge imaging positions two spectra so that the contrast material is removed from the breast glandularity values in the 2DAC map.

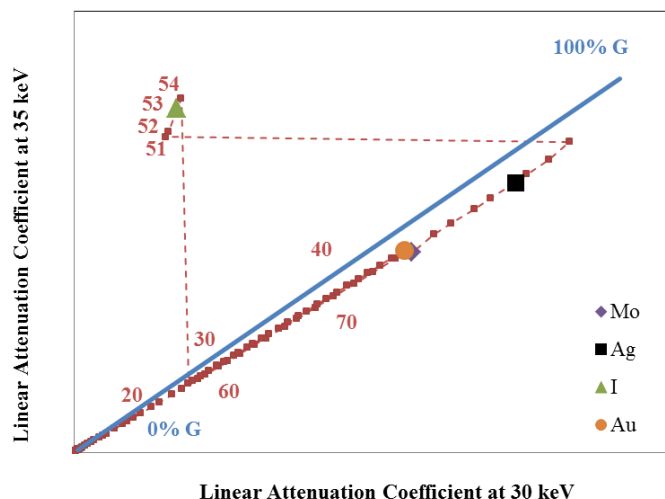


**Figure 5.** 2-dimensional attenuation coefficient (2DAC) maps at (30, 35) keV. The blue line represents the breast glandularity values (from 0% glandular (G) to 100% glandular), while the red squares corresponds to materials with atomic numbers from 1 to 80. K-edge imaging positions two spectra so that the contrast material is removed from the breast glandularity values in the 2DAC map.

Currently, CEDE breast imaging is performed with an iodinated contrast agent. These agents are typically small tri-iodobenzene compounds with substitutions for improved water solubility<sup>66</sup>. They are extremely stable and chemically inert, resisting biodegradation *in vivo* over long periods of time. These agents are administered intravenously to identify tumorigenic neovasculature. They are, however, plagued by several deficiencies. The non-specific nature of the contrast agent results in random vascular permeation and their relatively low molecular weight facilitates rapid renal clearance. Therefore, the percentage of the injected dose that reaches the tumor site is low because these agents are rapidly filtered by the kidneys and removed from the blood circulation. Additionally, iodinated agents have been linked to contrast media nephropathy in patients with preexisting renal insufficiency, such as diabetes mellitus<sup>67, 68</sup>.

As a result, there has been much effort to develop improved imaging agents for DE radiography<sup>61, 69–73</sup>. Several materials (gold, ytterbium, and tantalum) have been identified as potential alternatives. However, previous analysis and experimentation has been directed at x-ray energies (80 to 140 kVp) for applications

other than breast radiography. Thus, there exists a need to identify materials that are specifically optimized for CEDE x-ray breast imaging. To this end, we have developed an analytical framework to compare various contrast materials quantitatively for application in CEDE breast radiography. This framework is based on the logarithmic subtraction of low- and high-energy images to create a DE image. Metrics are proposed to quantify the contrast and contrast-to-noise ratio (CNR) for potential imaging agents and to identify those agents that would perform better than iodine. This work is intended to inspire further research in novel contrast materials in the hope that an agent optimized for DE breast imaging may be discovered.

## 2. METHODS

### 2.1. Formulation of DE Signal Intensity

The number of x-ray photons passing through a given material can be expressed in terms of the linear attenuation coefficient ( $\mu$ ) and thickness ( $t$ ). In the simplistic case of a monoenergetic beam of x-rays, the photon fluence ( $N$ ) after passing through a material can be written using the Beer-Lambert Law as:

$$N = N_0 \exp\left(-\sum \mu t\right) \quad (1)$$

where  $N_0$  is the initial photon fluence. The product of the linear attenuation coefficient and thickness is summed over all the materials present in the beam path. The signal intensity resulting from the photons can be expressed in terms of the logarithm of  $N$ :

$$SI = \ln(N) = \ln(N_0) + \left(-\sum \mu t\right) \quad (2)$$

In the case of CEDE x-ray breast imaging, the principal materials that contribute to the attenuation of the photons are (a)dipose, (g)landular, and (c)ontrast agent. Thus, the signal intensities for both low- (LE) and high- (HE) energy photons can be written as:

$$SI^{LE} = \ln(I^{LE}) = \ln(I_0^{LE}) + (-\mu_a^{LE} t_a - \mu_g^{LE} t_g - \mu_c^{LE} t_c) \quad (3)$$

$$SI^{HE} = \ln(I^{HE}) = \ln(I_0^{HE}) + (-\mu_a^{HE}t_a - \mu_g^{HE}t_g - \mu_c^{HE}t_c) \quad (4)$$

If the total thickness of tissue ( $t_T$ ) is assumed to consist of solely adipose and glandular components, it can be expressed as:

$$t_T = t_a + t_g. \quad (5)$$

By replacing  $t_a$  in Equations 3 and 4, the signal intensities at each energy can be described in terms of  $t_T$ ,  $t_g$ , and  $t_c$ .

$$SI^{LE} = \ln(I_0^{LE}) - \mu_a^{LE}t_T + t_g(\mu_a^{LE} - \mu_g^{LE}) - \mu_c^{LE}t_c \quad (6)$$

$$SI^{HE} = \ln(I_0^{HE}) - \mu_a^{HE}t_T + t_g(\mu_a^{HE} - \mu_g^{HE}) - \mu_c^{HE}t_c \quad (7)$$

The DE signal intensity ( $SI^{DE}$ ) can be expressed as the weighted subtraction between the low- and high-energy signal intensities, using a weighting factor,  $W$ :

$$SI^{DE} = SI^{HE} - W \times SI^{LE}. \quad (8)$$

Consequently,  $SI_{DE}$  can be separated into a linear combination of  $t_T$ ,  $t_g$ , and  $t_c$ . (9a)

$$SI^{DE} = \ln(N_0^{HE}) - W \times \ln(N_0^{LE}) + t_T \times [-\mu_a^{HE} + W \times \mu_a^{LE}] + \dots$$

$$t_g[(\mu_a^{HE} - \mu_g^{HE}) - W \times (\mu_a^{LE} - \mu_g^{LE})] + \dots \quad (9b)$$

$$t_c[\mu_c^{HE} - W \times \mu_c^{LE}]. \quad (9c)$$

## 2.2. Calculation of Weighting Factor, Contrast and Contrast to Noise Ratio

The first component of  $SI^{DE}$  (9a) is a function of the initial photon fluence and the total thickness of tissue. The initial photon fluence can be assumed to be constant across the image, given that the variation in the distance from the x-ray source to individual detector elements is small. Under mammographic compression, the total thickness of tissue varies by roughly 5% across the image of the breast, and therefore is ignored in



this study <sup>74</sup>. Thus, (9a) can be assumed to be invariant across the area of the image and simply provides a constant offset to  $SI^{DE}$ .

The second component (9b) describes the relationship between  $SI^{DE}$  and the thickness of glandular tissue in the beam. By choosing  $W$  as

$$W = \frac{\mu_a^{HE} - \mu_g^{HE}}{\mu_a^{LE} - \mu_g^{LE}}, \quad (10)$$

we can eliminate this dependence. The only remaining term that varies across the image is the third component (9c). This component quantifies the linear relationship between  $SI^{DE}$  and  $t_c$ . The DE contrast,  $S_c$ , can be defined as the change in  $SI^{DE}$  with respect to  $t_c$ :

$$\frac{d(SI^{DE})}{d(t_c)} = S_c = -\mu_c^{HE} + \frac{\mu_a^{HE} - \mu_g^{HE}}{\mu_a^{LE} - \mu_g^{LE}} \times \mu_c^{LE}. \quad (11)$$

The noise ( $\sigma_{bkg}$ ) in the background signal can be obtained from (9a), and formulated as

$$\sigma_{bkg} = \left( \frac{1}{I_0^{HE} \exp(-\mu_a^{HE} t_T)} + \frac{W^2}{I_0^{LE} \exp(-\mu_a^{LE} t_T)} \right)^{1/2}. \quad (12)$$

A total dose of 1.0 mGy was assumed for the LE and HE images, at a breast thickness of 5 cm. The dose distribution between the LE and HE images was allowed to vary. From (11) and (12), the contrast-to-noise ratio (CNR) is calculated as:

$$CNR = \frac{S_c}{\sigma_{bkg}} \quad (13)$$

### 3. RESULTS

#### 3.1. Energy Dependence of $W$ , $S_C$ , and $CNR$

$W$  is calculated for LE and HE pairs between 10 and 50 keV, and plotted in Figure 6.  $W$  is independent of the contrast material chosen and solely depends on the linear attenuation coefficients of adipose and glandular tissue.  $W$  assumes values between 0 and 1, and increases as the separation between the LE and HE decreases. This can be easily explained by studying the variation of the linear attenuation coefficients of adipose and glandular tissue with energy (see Figure 7). As the energy increases, the difference in attenuation coefficient between the two materials decreases. Thus,  $W$ , the ratio between the differences, is least when the LE and HE are furthest apart and 1 for the trivial case when the LE is equal to the HE.

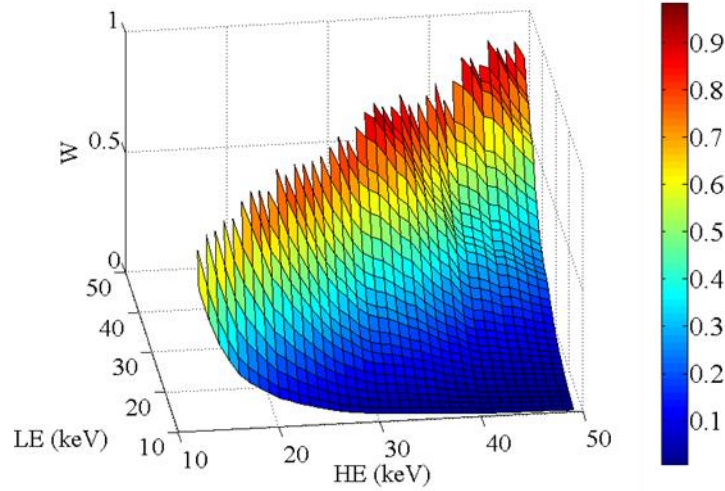


**Figure 6.**  $W$  calculated for energy combinations ranging from 15 to 50 keV.  $W$  ranged from 0 to 1, while steadily increasing towards the diagonal of the plot.  $W$  increases as the low- (LE) and high (HE) energies are closer together.

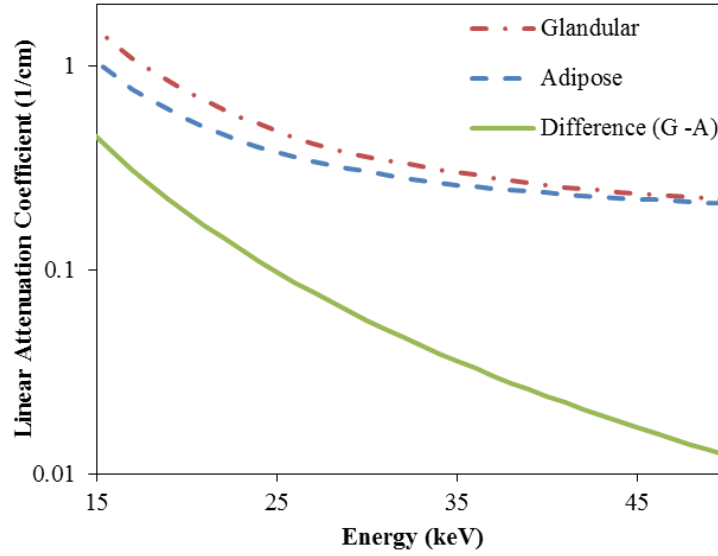


**Figure 7.** Energy dependence of the linear attenuation coefficients of glandular, adipose tissue, as well as the difference between these two materials (Glandular – Adipose).

Figure 8 shows the energy dependence of  $S_C$  for Mo ( $Z = 42$ ), Ag ( $Z = 47$ ), I ( $Z = 53$ ), and Au ( $Z = 79$ ). The graphs show that  $S_C$  is only large when the LE and HE are positioned on opposite sides of the k-edge of the material. As expected, Au shows no contrast for any combination of LE and HE studied because the k-edge of gold (80 keV) lies outside of the energy range. These results demonstrate that while materials, such as gold, may have application in higher energy and temporal-subtraction imaging, their application in DE breast imaging is limited. In addition,  $S_C$  shows a greater dependence on the HE value than the LE value. This can be observed in Figure 9 where a contour map of  $S_C$  of iodine is overlaid with arrows indicating the gradient vectors of  $S_C$ . The direction of the arrows indicates the direction of the gradient vector, while the length indicates the magnitude. As the arrows have no substantial component in the LE direction, it can be deduced that the location of the HE has a greater influence on  $S_C$  than the location of the LE. This was found to be true regardless of contrast material.

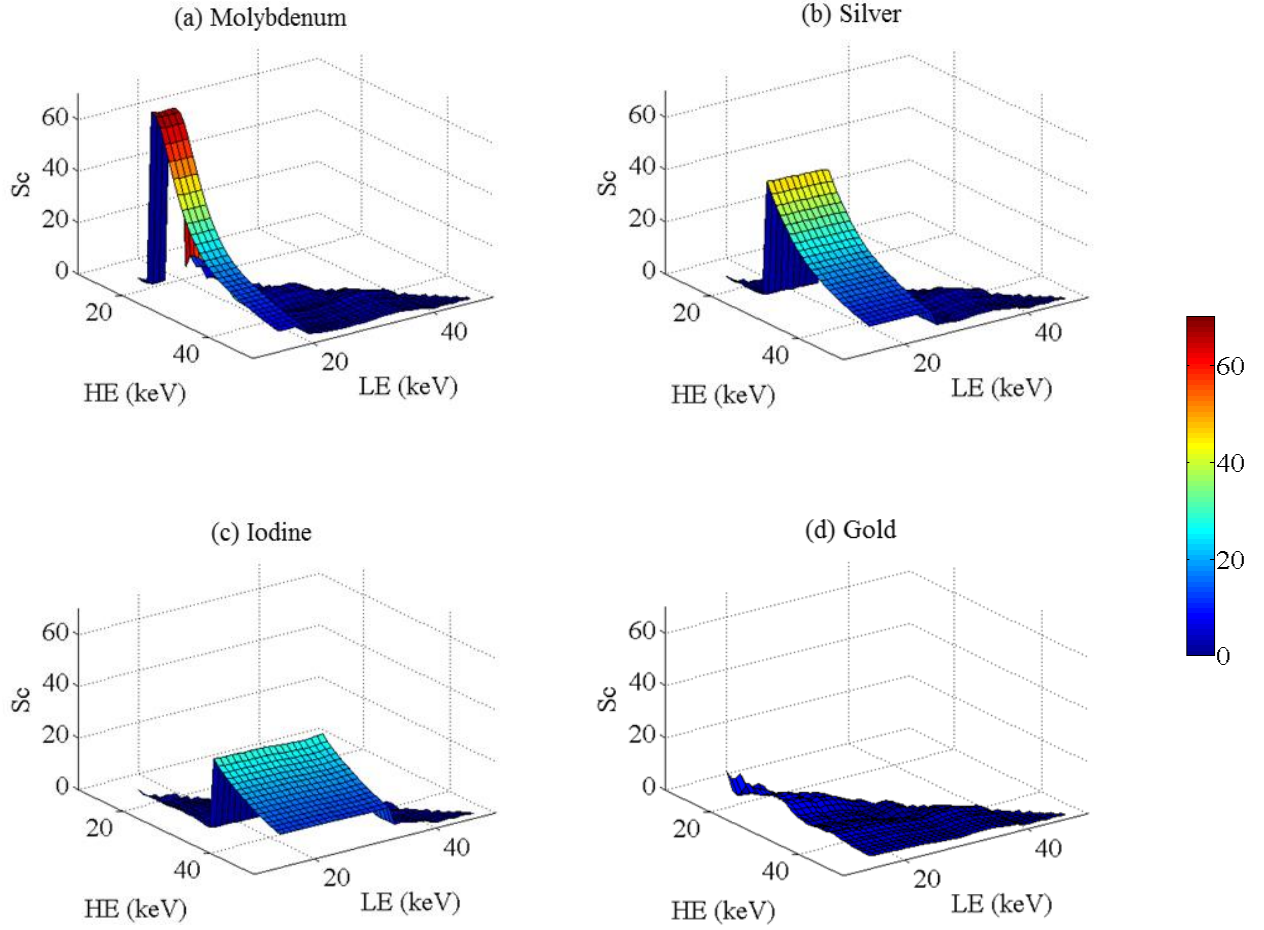


**Figure 8.** Energy dependence of  $S_C$  for (a) Molybdenum, (b) Silver, (c) Iodine, and (d) Gold.  $S_C$  is only greater than 0 when the LE and HE bracket the  $k$ -edge of the material

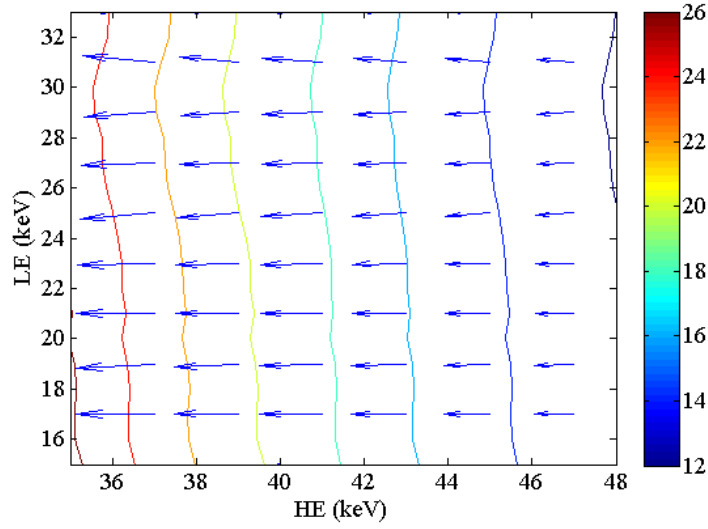


**Figure 9.**  $S_C$  of iodine as a function of the HE and LE for energy pairs that bracket the k-edge (33 keV).

The dependence of  $CNR$  on energy and material is demonstrated in Figure 10. The graphs are plotted for a breast thickness of 5 cm, with a dose fraction of 0.5 to the LE image. Similar to  $S_C$ , a large value of  $CNR$  is only obtained for energy pairs that bracket the k-edge of the material. As expected,  $CNR$  is not observed for materials such as Au whose k-edge lies outside of the energy range. However, the variation in  $CNR$  with material is less than that of  $S_C$ . For example the maximum  $S_C$  for Ag is 1.6 times that of I, whereas the maximum  $CNR$  of Ag is 1.04 times that of iodine at a dose fraction of 0.5. This discrepancy between  $S_C$  and  $CNR$  is a result of the energy dependence of the image noise. The noise in the DE image increases substantially for lower values of both LE and HE because of the poor penetration through the breast, resulting in fewer x-rays being detected. This penalizes materials with lower atomic number because the optimal energies are lower.

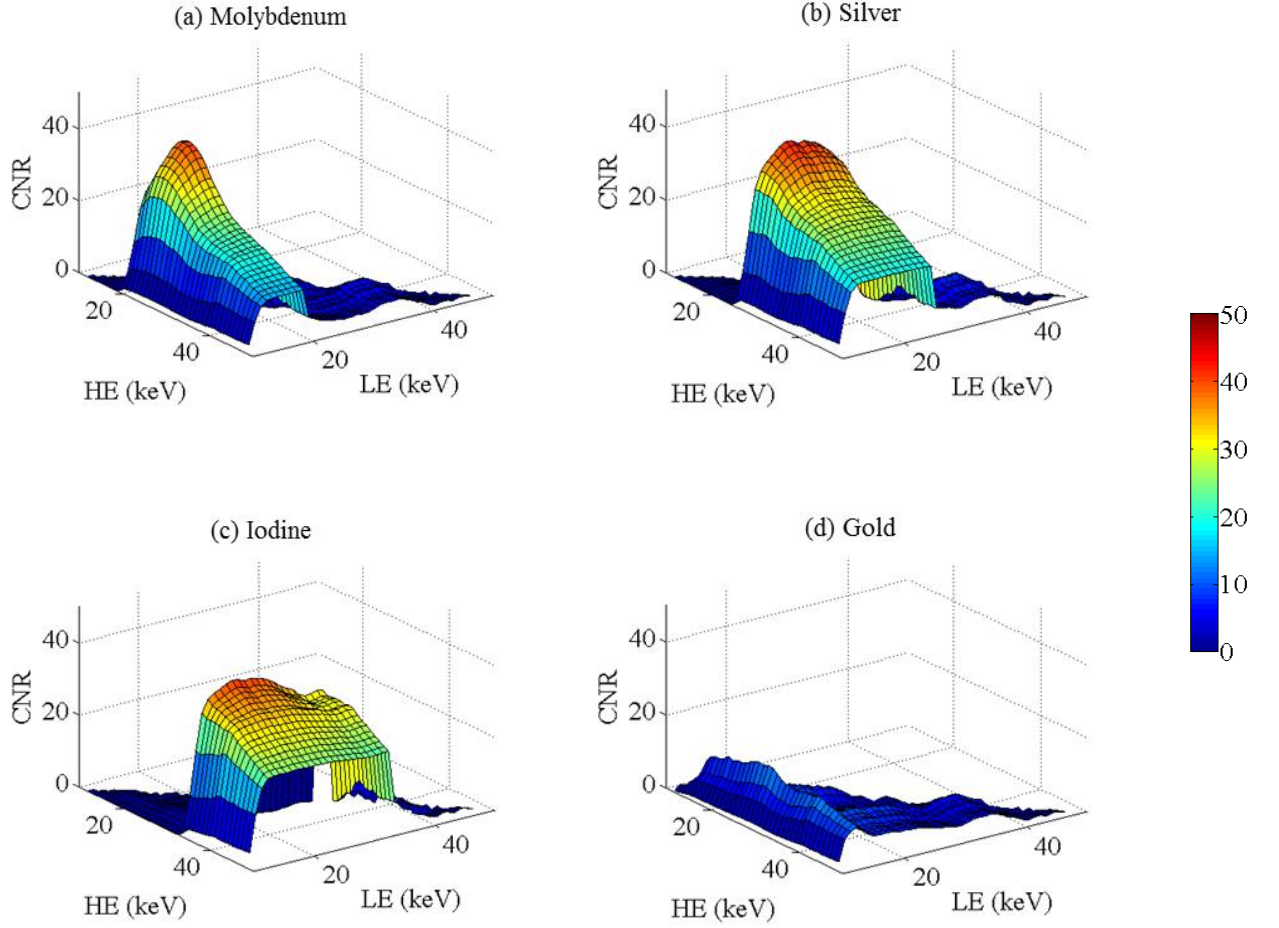


**Figure 10.** Energy dependence of CNR for (a) molybdenum, (b) silver, (c) iodine, and (d) gold for a dose distribution of 50% to LE.

### 3.2. Maximum CNR for each material

The maximum CNR for every material in the range of  $Z = 1$  to 80 is shown in Figure 11. The corresponding dose fractions that result in these optimal points are overlaid. The graph can be divided into two main regions: R1) atomic numbers less than 33 or greater than 63, and R2) atomic numbers between 34 and 62. The materials in R1 exhibit very little contrast due to the absence of a k-edge in the energy range studied. The optimal dose fraction in this range has values between 0.1 and 0.5, which minimizes the noise. The more interesting materials are found in R2. The CNR slowly increases and reaches a plateau for materials with atomic numbers between 42 and 63. Within this plateau, the maximum CNR differs by less than 15%.

The absolute maximum occurs at  $Z = 59$ , Praseodymium, with a dose fraction of 0.2 to the LE at an (LE, HE) energy pair of (18, 42). The dose fraction within R2 reaches its maximum value of 0.7 at an atomic number of 34. As the atomic number increases, the optimal dose fraction decreases until it reaches its minimum value of 0.1 at an atomic number of 63.

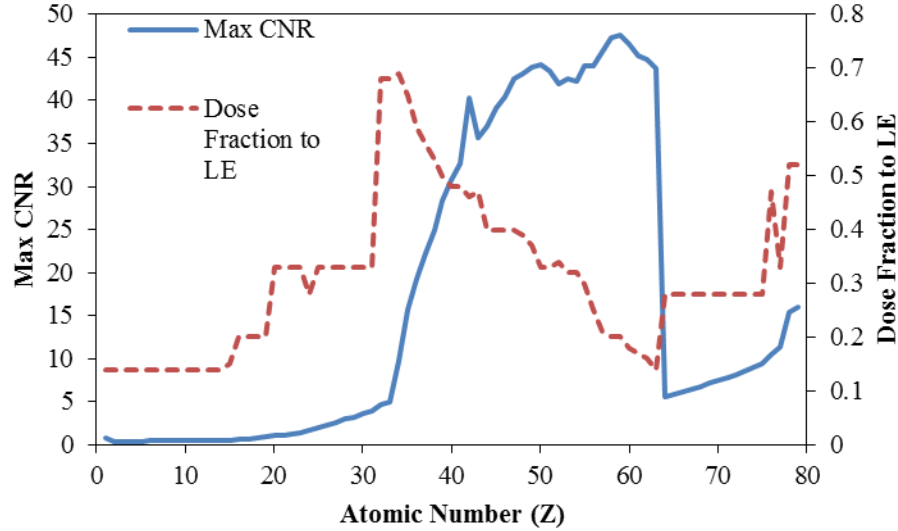


**Figure 11.** Overlay of the maximum CNR and corresponding dose distribution for materials with  $Z$  ranging from 1 to 80.

The trend observed for the dose fraction to the LE image within R2 can be explained by analyzing the variation in  $W$ . Figure 12 is an overlay of the optimal dose fraction (from Figure 11) and the corresponding values of  $W$ . The optimal LE for the materials within the plateau of R2 was consistently calculated to be 18 keV. The static location of the optimal LE is a result of the simulation attempting to minimize the noise in the LE image. A LE value of 18 keV represents an optimal point that achieves this goal. The HE was found to be optimized directly above the k-edge of the material. Thus, as the atomic number (and k-edge) increases, the separation between the LE and HE increases resulting in decreasing values of  $W$ . As  $W$  decreases, the optimization algorithm opts to allocate a greater portion of the total dose to the HE image to

reduce the DE noise in the background (Equation 12). Decreasing the dose fraction to the LE image ensures that the noise will reach a minimum value, and thus maximize the *CNR*.

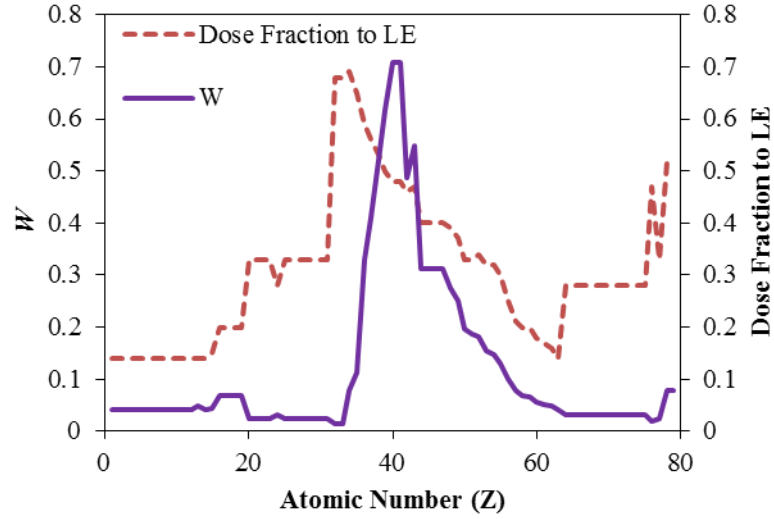


**Figure 12.** Overlay of the optimal weighting factor leads to the maximum *CNR* (from Figure 11) and the corresponding dose fractions to the LE.

### 3.3. Candidate contrast materials for CEDE breast imaging

Table 3 lists some of the materials that make up the plateau of maximum *CNR* in Figure 11. Listed for each material are the atomic number, k-edge, maximum *CNR*, optimal dose fraction, optimal energy pair and current nanoparticle-based research applications. As observed from the current nanoparticle-based imaging research, none of these materials, apart from clinically-used iodine, have been investigated for application as DE imaging agents. Nanoparticles are particularly beneficial for use as contrast agents due to the ability to finely tune their physical and functional characteristics and so directly control their interactions in the body <sup>75</sup>. For example, nano-silver represents the largest (25%) and fastest growing category of nanotechnology-based consumer products <sup>76</sup>. The majority of these applications make use of the broad-spectrum antimicrobial and unique optical scattering properties of silver <sup>77–82</sup>. There has been little interest



to date in developing silver nanoparticles as x-ray imaging agents, but the data presented here suggests silver offers comparable *CNR* to iodinated contrast agents with more achievable energy pairs and appropriate dose fractions. Similarly, molybdenum lies within the plateau of materials in R2. Molybdenum oxide nanoparticles have been utilized as hosts for ion insertion with applications as catalysts, gas sensors, fuel cell membranes, electrochromic windows and lithium-ion batteries <sup>83</sup>. However, *Mo* nanoparticles have yet to be investigated as potential CEDE imaging agents.

**Table 3.** *Potential contrast materials for DE breast radiography. The materials are listed with their atomic number, maximum  $S_C$  (DE contrast), improvement over iodine and current nanoparticle-based research. The improvement over iodine is calculated as the as ratio of the maximum SC of the contrast material to that of iodine. Current nanoparticle-based research applications for each material are also listed.*

Material	Z	K-edge	Maximum CNR	Optimal fraction to LE	dose	Optimal energy pair (LE,HE)	Current nanoparticle-based research applications
Molybdenum	42	20.0	40.3	0.46		(18,23)	catalysts, fuel cell membranes <sup>83</sup>
Rhodium	45	23.2	39.0	0.40		(18,26)	Catalysis <sup>84</sup>
Palladium	46	24.4	40.4	0.40		(18,26)	asymmetric catalysis <sup>85</sup>
Silver	47	25.5	42.6	0.40		(18,26)	antimicrobial, optical scattering <sup>77-82</sup>
Tin	50	29.2	44.1	0.33		(18,30)	gas microsensors, Li-ion batteries <sup>86</sup>
Tellurium	52	31.8	41.9	0.34		(18,32)	Semiconductor in electronic and optoelectronic <sup>87</sup>
Iodine	53	33.2	42.6	0.32		(18,34)	x-ray contrast agents <sup>38</sup>
Barium	56	37.4	44.1	0.25		(18,38)	capacitors, non-linear optics <sup>88</sup>

#### 4. DISCUSSION

CEDE breast x-ray imaging represents an exciting new imaging tool in the detection and characterization of breast lesions<sup>20–22, 28, 33–35</sup>. The technique suppresses the variation in anatomical signal intensity to improve the detection and quantification of exogenous imaging agents. Currently, CEDE imaging is performed with iodinated contrast agents to visualize tumor vasculature. These agents are, however, prone to certain deficiencies such as off-target accumulation, toxicity, and low circulation times. Our work is intended to identify novel contrast materials whose contrast is comparable or superior to that of iodine in the mammographic energy range so that an agent optimized for DE breast imaging may be discovered.

The DE signal intensity is formulated as the weighted logarithmic subtraction between the LE and HE images. The signal intensities of the LE and HE images are expressed in terms of the linear attenuation coefficients and thicknesses of the adipose, glandular and contrast material. The resulting weighting factor and *CNR* can be explicitly formulated using these factors. The formulation is similar to the subtraction weighting factor, *R*, and dual-energy signal-to-noise ratio described by Brettle *et al.*<sup>89</sup>. There are, however, several important distinctions. Brettle’s analysis was geared towards the isolation of microcalcifications from the soft-tissue background using dual-energy mammography. In addition, their analysis combined the attenuation of the adipose and glandular tissue into a singular compartment, called breast tissue. On the other hand, our analysis is focused on the visualization of an external contrast agent using k-edge imaging. The breast background is broken down into adipose and glandular tissue, and the weighting factor is calculated to remove the signal variation that arises from various admixtures of these tissue components.

In the calculation of *W*, the total breast thickness under compression is assumed to be constant across the image. This has several practical consequences. The amount of compression applied during the dual-energy examination may need to be increased to ensure that the variation in thickness across the breast is minimal. However, increasing the compression force is likely to alter the blood kinetic profiles of the contrast agent and restrict the delivery of the contrast agent to the breast as an organ. Alternatively, a thickness-dependent weighting factor can be used to subtract regions towards the edge of the breast that may be otherwise

poorly subtracted due to the uneven thickness of tissue. It is important to note that  $W$ , as calculated in this monoenergetic model, is independent of the thickness of the breast. This is not true for polyenergetic spectra where secondary effects such as beam hardening can alter the effective attenuation coefficients of materials depending on thickness. Thicker materials will appear to have lower effective attenuation coefficients than their thinner counterparts.

This study also ignores the influence of scatter. Scattered x-ray photons can give the appearance of a lower thickness of tissue in the beam path. Thus, as long as the scatter is constant across the breast, the proposed subtraction technique is able to remove the anatomical signal variation effectively. Constant scatter would simply add an offset in Equation 9a and would therefore not affect the calculation of  $W$ . Scatter does, however, play an important role in the calculation of the maximum  $CNR$  for various materials. The fraction of primary x-ray photons that are scattered is lower at lower energies, and would therefore not be constant across the various materials. As previously mentioned, the framework is built upon the assumption of a monoenergetic x-ray source. The translation of this work into polyenergetic x-ray beams would require some modification to the framework to account for the variation in attenuation coefficients of adipose, glandular, and contrast material with energy. The findings presented here can serve as a reference for a more detailed analytical comparison of contrast materials using polyenergetic spectra.

The analysis identified a group of materials from atomic numbers 42 to 63 that maximize  $CNR$  in DE breast imaging. As the atomic number increases, the HE value increases, and the dose fraction decreases. Iodine, with  $Z = 53$ , lies within the midpoint of these materials. The optimal imaging protocol for iodine requires an energy pair of (LE, HE = 18, 34) and a dose fraction of 0.32 to LE. In a practical sense, high mean energies, such as 34 – 49 keV, require high kV together with substantial filtration to achieve a suitable HE spectrum<sup>90</sup>. The resulting reduction in photon fluence requires the tube current-time product (mAs) to be increased to accommodate for the reduced fluence. Clinical acquisition systems have limitations on tube loading and exposure time which may prevent optimal high energy spectra being achieved for high  $Z$  materials. In addition, maximizing  $CNR$  for high  $Z$  materials requires that a low dose fraction to the LE image be used. Low dose LE images will be intrinsically noisy and will limit the anatomical information that can be provided by DE breast imaging.

Following this logic, lower Z materials from the plateau region may be more favorable based upon more achievable energy pairs, and dose fractions that provide good quality anatomic images. As iodine is currently the standard in CE breast imaging, despite possessing several limitations, it can be treated as the highest feasible atomic number contrast agent. Therefore, contrast agents with atomic numbers between 42 and 52 should be superior for CEDE breast imaging. These materials need to be further investigated in terms of toxicity, delivery mechanism and ease of fabrication to identify novel contrast agents specifically designed for DE imaging in the breast.

## **5. CONCLUSIONS**

This work identifies novel contrast materials that are potentially superior to iodine for CEDE x-ray breast imaging. Iodinated agents display excellent stability in the body while resisting degradation over long periods of time. However, they are limited by rapid clearance, poor tumor targeting ability and contrast media-induced toxicity. Through analytical modeling, a group of materials with atomic numbers ranging from 42 to 63 was identified to maximize *CNR* values in the mammographic energy range. Several of these materials have been investigated in nanoparticle-based applications but none, other than iodine, have been investigated for applicability as imaging agents in CEDE x-ray breast imaging. Of these materials, those with lower Z, between 42 and 52, may be more favorable by offering more achievable energy pairs and appropriate LE dose fractions. These results represent the first step in the development of new contrast agents optimized for DE x-ray breast imaging.

## CHAPTER 3

### ABSTRACT

Through prior monoenergetic modeling, we have identified silver as a potential alternative to iodine in dual-energy (DE) x-ray breast imaging. The purpose of this study is to compare the performance of silver and iodine contrast agents in a commercially-available DE imaging system through a quantitative analysis of signal difference-to-noise ratio (SDNR). A polyenergetic simulation algorithm was developed to model the signal intensity and noise. The model identified the influence of various technique parameters on *SDNR*. The model was also used to identify the optimal imaging techniques for silver and iodine, so that the two contrast materials could be objectively compared. The major influences on the *SDNR* were the low-energy dose fraction and breast thickness. An increase in the value of either of these parameters resulted in a decrease in *SDNR*. The *SDNR* for silver was, on average 43% higher than iodine when imaged at their respective optimal conditions, and 40% higher when both were imaged at the optimal conditions for iodine. A silver contrast agent should provide benefit over iodine, even when translated to the clinic without modification of imaging system or protocol. If the system were slightly modified to reflect the lower k-edge of silver, the difference in *SDNR* between the two materials would be increased. These data are the first to demonstrate the suitability of silver as a contrast material in a clinical CEDE image acquisition system.

## 1. INTRODUCTION

Contrast-enhanced (CE) dual-energy (DE) x-ray breast imaging provides quantitative functional information with high-resolution anatomical data in a single imaging procedure. DE images can be used to identify tumor neovasculature and morphology, and consequently aid in the detection and diagnosis of breast cancer<sup>20–22, 28, 33–35</sup>. The most widely-used approach for DE imaging is k-edge imaging. In this technique, two distinct energy windows [low (LE) - and high-energy (HE)] are placed on either side of the k-edge of the contrast material. Through a weighted subtraction of the LE and HE images, it is possible to suppress the anatomical background signal and enhance the visualization of the contrast agent. The total dose of the two images is judiciously allocated so as to maximize the visibility of the contrast agent while providing an anatomical image of diagnostic quality. DE x-ray breast imaging has been shown to aid visualization of lesions that are otherwise mammographically occult as well as to provide functional blood flow information consistent with magnetic resonance imaging – the current gold standard in functional breast imaging<sup>28, 32–35</sup>. This has led to the development of several DE imaging systems by Hologic (Hologic, Bedford, MA, USA), GE (General Electric, Fairfield, CT, USA), and Philips (Royal Philips, Amsterdam, Netherlands)<sup>28–30</sup>.

Currently, CEDE breast imaging is performed with an iodinated contrast agent. These agents are typically small molecules consisting of tri-iodinated benzene rings with substitutions for improved solubility. They are extremely stable in the body and can resist degradation over long periods of time. However, they are plagued by several limitations. Due to their small size, these agents are rapidly filtered by the kidney, and therefore necessitate immediate post-injection imaging<sup>61</sup>. Filtration by the kidneys can lead to contrast-media induced nephropathy in patients with preexisting renal insufficiency, such as diabetes mellitus<sup>67, 68</sup>. The non-specific nature of the contrast agents results in random vascular permeation and low tumor-targeting potential. These limitations can be overcome with the use of a nanoparticle-based imaging agent. Nanoparticles can be targeted with surface ligands to attach to specific cell surface antigens, and provide functional information on the target<sup>75, 91, 92</sup>. The nanoparticle surface can also be modified to prolong circulation times and thereby increase the dose delivered to the target site<sup>75, 93–95</sup>.

We have previously developed a theoretical framework to identify new, candidate materials for DE x-ray breast imaging<sup>96</sup>. The framework quantifies the DE contrast-to-noise ratio (CNR) as a function of atomic number ( $Z$ ). The results demonstrated an optimal group of materials with  $Z$  from 42 to 63 in which the maximum CNR varies by less than 15%. However, there are certain caveats to be considered before experimentally testing any of these materials. The theoretical model is based on a monoenergetic source of x-rays and demonstrated that as  $Z$  increases, the optimal HE values increase, while the allocation of dose to the LE image decreases. From a practical perspective, substantial filtration is necessary to obtain HE spectra with high mean energy. This results in infeasibly large tube current-time products (mAs) to ensure clinical image quality. In addition, LE images acquired with low doses will result in noisier anatomic images that will limit the effectiveness and applications of the imaging technique. Upon consideration of these constraints, contrast materials with lower atomic numbers are more suitable for testing. As iodine ( $I$ ,  $Z=53$ ) is currently the standard in DE breast imaging and notably suffers from these limitations, it can be treated as the highest feasible atomic number for use as a contrast material.

Theoretical modeling and practical considerations have narrowed the list of potential DE contrast materials to those with atomic numbers ranging from 42 to 52. Silver ( $Ag$ ,  $Z=47$ ) was chosen based upon the following additional considerations.  $Ag$  represents a viable choice because of the large amount of literature already available on the development and manufacture of  $Ag$  nanoparticles<sup>77, 97-99</sup>. In addition, the prevalent use of silver filters in CEDE imaging means that the LE spectrum can be filtered to remove the energies above the k-edge of  $Ag$  contrast material. This is important because DE contrast can only be observed when the LE and HE spectra are predominantly on opposite sides of the k-edge of the imaging agent.

Nano- $Ag$  represents the largest (25%) and fastest growing category of nanotechnology-based consumer products<sup>76</sup>. Many of these applications make use of the broad-spectrum antimicrobial and optical scattering properties of  $Ag$ <sup>77-82, 100, 101</sup>. For example, Kumar *et al.*<sup>100</sup> embedded  $Ag$  nanoparticles in household paint to develop an antimicrobial coating that can be directly applied to wood, glass, and polymers. The surfaces coated with the  $Ag$ -embedded paint showed excellent antimicrobial effects on both Gram-positive and Gram-negative human pathogens. McFarland *et al.*<sup>101</sup> used  $Ag$  nanoparticles in

combination with dark-field microscopy for the quantitative sensing of streptavidin with a subpicomolar limit of detection. To our knowledge, there has been no work reported to date where the potential role of Ag nanoparticles as a radiographic agent is demonstrated.

In this work, we explore the feasibility of a Ag-based agent for DE x-ray breast imaging. The primary goal of this manuscript is to determine if a Ag agent could outperform an iodinated contrast agent on a commercially available imaging system with little or no modification to the existing system design. The imaging system investigated in this work is the prototype Hologic Dimensions CEDE x-ray acquisition system (Hologic, Bedford, MA, USA). The technique parameters, including LE and HE kV, filter material, and mAs are pre-selected based upon the breast thickness. These parameters were determined by Hologic (Hologic, Bedford, MA, USA) using simulations and experimental validation using iodinated inserts in a CIRS phantom (Computerized Imaging Reference Systems Inc., Norfolk, VA, USA). The total dose of the LE and HE image pair is set to equate roughly to a standard two-view mammographic exam.

For this chapter, a computational algorithm was developed in MATLAB (The MathWorks, Inc., Natick, MA, USA) to identify the set of image parameters, particular to this system, that optimize the signal difference-to-noise ratio (*SDNR*) for a Ag and I contrast agent. The algorithm was constrained by the values of HE and LE kV, filters, and dose utilized by the imaging system. Thus, the findings presented here are not those of an optimization search, in the strictest sense. The algorithm was designed to test the performance of a Ag agent on an existing imaging system to determine the ease with which a potential agent could be transferred to the clinic. The algorithm was validated by comparing simulated metrics of DE *SDNR* with experimentally obtained values. The algorithm was then used to identify parameters with which to compare the performance of Ag and I using physical phantoms experimentally.



## 2. METHODS

### 2.1. Development of simulation algorithm

A simulation algorithm was developed in MATLAB (The MathWorks, Inc., Natick, MA, USA) to identify the set of clinically-feasible technique factors and image processing parameters that maximized the *SDNR* for various imaging agents. The values of kV, filter materials, and filter thicknesses chosen for the search reflect those that are available on the prototype Hologic CEDE Dimensions system (Hologic, Bedford, MA, USA – see Table 4).

**Table 4.** *Values of parameters used in the simulation algorithm*

Parameter	Values
Target	tungsten
Low Energy (kV)	23 to 35
High Energy (kV)	36 to 49
Filter Materials (thickness in $\mu\text{m}$ )	<u>Low Energy:</u> silver (50), rhodium (50), and aluminum (700) <u>High Energy:</u> copper (300)
Detector	selenium, energy-integrating, 200 $\mu\text{m}$
Breast Thickness	2 to 8 cm

Four constraints are placed on the simulation algorithm:

1. The total mean glandular dose to the breast was set to match the Hologic system as a function of breast thickness;
2. The allocation of the dose between the low- and high-energy images (dose fraction) was expressed as a percentage of the total dose allocated to the LE image. The dose fraction was allowed to vary from 10% (majority of the dose in HE) to 90% (majority of the dose in LE);

3. The maximum mAs is 240. Techniques which produce LE or HE images above this value were eliminated from further study;
4. A minimum signal threshold was required. Techniques which produced LE or HE images below the threshold were eliminated from further study.

The spectra (LE and HE) were generated using Boone's interpolating polynomials method<sup>102</sup>. The spectra were then attenuated using the Beer-Lambert law through a combination of the filter material, air and 0.7 mm of beryllium. The source-to-image distance is 70 cm on the Hologic system. The spectra were then scaled appropriately to ensure that the total mean glandular dose to the breast from the LE and HE images matched the Hologic dose (constraint 1). The mAs required to achieve this dose was then calculated. The mAs and signal intensity were tested to ensure they were within the limitations of the physical system (constraints 3 and 4). If the mAs and signal intensity criteria were met for the DE spectral pair, the simulation algorithm calculated the DE weighting factor,  $W$ , and the  $SDNR$ . In total, 26,460 unique combinations of imaging parameters were studied.

## 2.2. Calculation of $W$ and $SDNR$

The signal intensity ( $SI$ ) recorded by the energy-integrating detector is given by:

$$SI = \sum_{E=1}^{kV} (I_d \times E \times \Delta E) \quad (1)$$

where  $I_d$  is the spectral photon fluence incident on the detector,  $E$  is the energy (keV),  $\Delta E$  is the size of the energy bins, and  $kV$  is the applied tube potential difference. The standard deviation,  $\sigma$ , of the signal intensity is calculated as:

$$\sigma = SI^{0.46} \quad (2)$$

The power term of 0.46 was obtained from Marshall *et al.*<sup>103</sup>. A value of 0.5 would correspond to a Poisson distribution of  $SI$ . The DE weighting factor is calculated as:

$$W = \frac{\ln(SI_{HE}^a) - \ln(SI_{HE}^g)}{\ln(SI_{LE}^a) - \ln(SI_{LE}^g)} \quad (3)$$

The superscripts,  $a$  and  $g$ , refer to adipose and glandular tissue, respectively. This formulation is adapted from our previous theoretical model to account for polyenergetic spectra<sup>96</sup>. The DE  $SI$  ( $SI^{DE}$ ) is calculated from the LE and HE  $SI$  as:

$$SI_{DE} = SI_{HE} - W \times SI_{LE} \quad (4)$$

This calculation is performed for breast tissue with and without added contrast material (superscripts:  $cont$  and  $bkg$  respectively). The resulting imaging contrast is quantified using  $SDNR$ :

$$SDNR = \frac{SI_{DE}^{cont} - SI_{DE}^{bkg}}{\sigma_{DE}^{bkg}} \quad (5)$$

The DE standard deviation ( $\sigma^{DE}$ ) is calculated as:

$$\sigma_{DE} = \sqrt{\sigma_{HE}^2 + W^2 \times \sigma_{LE}^2 - 2 \times W \times cov(\ln(SI_{HE}^{bkg}), \ln(SI_{LE}^{bkg}))} \quad (6)$$

The expression of  $\sigma^{DE}$  is the propagation of error resulting from the weighted subtraction of the LE and HE signal intensities. The covariance term ( $cov$ ) was experimentally measured by imaging a 4 cm block acrylic phantom using combinations of LE and HE spectral pairs. The resulting values of  $\sigma^{DE}$ ,  $\sigma^{HE}$ , and  $\sigma^{LE}$  were used with Equation 6 to obtain the covariance. A representative value of the covariance, averaged over the spectral pairs, was used for the analysis. The effect of filter material, dose fraction and breast thickness on the values of  $W$  and  $SDNR$  of a Ag contrast agent were then studied.

### 2.3. Validating the Simulation Algorithm

The results of the simulation algorithm were validated using physical phantoms. Ten spectral pairs were chosen to be experimentally measured on the prototype Hologic Dimensions CEDE system (see Table 5). These were chosen to encompass a variety of LE and HE kV pairs, filter materials and LE dose fractions.  $W$  and  $SDNR$  were obtained experimentally and compared to the values obtained from the simulation.

**Table 5.** *Representative spectral pairs that were chosen to validate the simulation results. They consist of a mixture of LE, HE kV combinations, filter materials and LE dose fraction.*

Spectral Pair	High Energy (kV)	Low Energy (kV)	Low energy filter	LE dose fraction (%)
1	36	28	aluminum	70
2	42	28	aluminum	60
3	49	28	aluminum	60
4	36	26	rhodium	90
5	42	26	rhodium	50
6	49	26	rhodium	40
7	42	32	silver	40
8	42	35	silver	80
9	49	32	silver	70
10	49	35	silver	60

$W$  was measured using phantoms consisting of blocks of 100% adipose- and 100% glandular-equivalent CIRS (Computerized Imaging Reference Systems Inc., Norfolk, VA, USA) materials. The phantom materials were placed upon a lead sheet having a 10 mm diameter aperture to reduce the influence of scatter. Similarly, the assembly was imaged using a geometric magnification of 1.4 to reduce the number of scattered photons further (see Figure 13). The raw signal intensities were measured in a region of interest after the system-specific flat-fielding algorithm was applied.  $W$  was then calculated using Equation 3.



**Figure 13** *Experimental setup for determining  $W$ . Adipose- or glandular-equivalent CIRS materials were placed on a lead sheet with a hole and imaged under geometric magnification.*

To measure  $SDNR$ , the lead sheet was removed and a 50  $\mu\text{m}$  strip of Ag foil was placed on the surface of a 4 cm step phantom set directly on the breast support. LE and HE images were acquired for each spectral pair and subtracted to create DE images. Regions of interest in the DE image were chosen in the background and Ag foil to correspond to  $SI_{bkg}^{DE}$  and  $SI_{cont}^{DE}$ , respectively.  $SDNR$  was calculated using Equations 4-6.

#### *2.4. Comparing $SDNR$ between Ag and I*

A solution of Omnipaque (General Electric Healthcare, Little Chalfont, United Kingdom) iodinated contrast material was diluted to a final concentration of 16 mg/mL. An equal volumetric concentration of a silver solution was obtained by dissolving the required amount of silver nitrate in water. The two solutions were used to compare the  $SDNR$  of Ag and I contrast materials in a specially fabricated contrast-embedded step phantom. The phantom measures 3 x 4 x 10 cm (height x width x length). The phantom was positioned such that the x-ray path length from the focal spot to the detector is equal to the

height of the phantom (3 cm). A 4 mm hole was bored along the longitudinal direction to accommodate a Tygon (Saint-Gobain, La Defense, Courbevoie, France) R-3603 plastic tube (inner diameter: 3/32", outer diameter: 5/32") containing the contrast agents to be imaged against varying glandular percentages (from 0% to 100% glandularity, in 25% increments).

Using the simulation, the maximum  $SDNR$  at a thickness of 3 cm was determined for each of the three LE filter materials. This was performed for both I and Ag yielding 6 optimal spectral pairs. For each filter material, four imaging conditions were then carried out: (i) Ag at optimal Ag imaging conditions, (ii) I at optimal I imaging conditions, (iii) Ag at optimal I imaging conditions, and (iv) I at optimal Ag imaging conditions

### 3. RESULTS

#### 3.1. Simulation

If the simulation were to include all the possible combinations available on the prototype Hologic Dimensions CEDE system, as determined by constraints 1 and 2 in section 2.1, it would be possible to obtain values of  $SDNR$  for 26,460 unique combinations of imaging parameters. However, many of these combinations would be infeasible because they would either require impractical mAs or result in insufficient  $SI$ . Therefore, the mAs and  $SI$  criteria in constraints 3 and 4 require that 76% of these combinations be eliminated. The following results were obtained using the remaining 6,366 combinations of spectral pairs.

##### 3.1.1. Weighting Factor

Weighting factor,  $W$ , is calculated using Equation 3. From its formulation,  $W$  would be expected to show a dependence on the separation between the LE and HE spectra. This is demonstrated in Figure 14 where  $W$  is plotted as a function of the mean energies of the LE and HE spectra. The 6,366 data points were fit to a 2<sup>nd</sup> order polynomial surface with a root mean square error of 0.03.  $W$  is shown to decrease as the separation between the two spectra increases. This can be explained by an examination of the dependency of  $W$  on the signal intensities of adipose and glandular tissue. The natural logarithm of the signal intensity

is primarily dependent upon the linear attenuation coefficient of the material. Thus, Equation 3 can be thought of as the difference in linear attenuation coefficient between adipose and glandular tissue at the high energy divided by the difference at the low energy. As the energy increases, the difference in linear attenuation coefficient between these two materials decreases. These data agree with previous monoenergetic calculations that show that  $W$  is smaller when the LE and HE values are further apart.

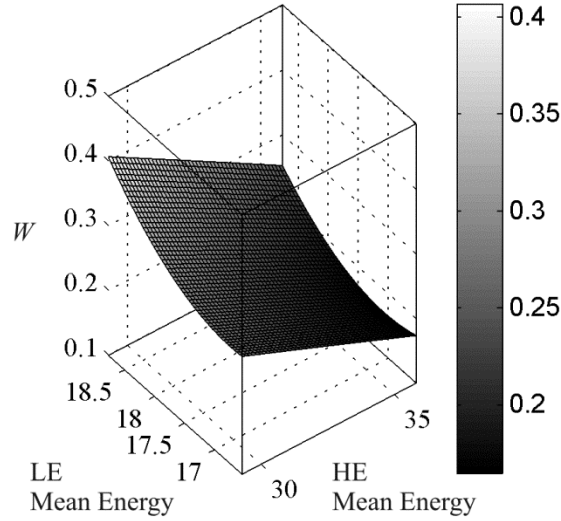


**Figure 14.** Surface plot of  $W$  as a function of the mean energy of the LE and HE spectra. The fitted surface is shown alone for better visibility.  $W$  is greatest when the two spectra are closest together and the least when the spectra are the furthest apart.

The relationship between  $W$  and the LE and HE mean energies can be used to explain the variation in  $W$  with all of the algorithm parameters. For example, Figure 15 shows  $W$  plotted for breast thicknesses ranging from 2 to 8 cm for a spectral pair of 46 kV HE with copper filtration and a 28 kV LE with rhodium filtration at a LE dose fraction of 40%.  $W$  increases with increasing breast thickness due to beam hardening; as breast thickness increases, a greater proportion of the low-energy photons are attenuated. While beam hardening affects both LE and HE spectra, the increase in mean energy is more noticeable in the LE spectrum due to the higher proportion of low-energy photons. As a result, the mean energy of the LE

spectrum increases faster than that of the HE spectrum. The reduction in spectral separation with increasing thickness results in an increase in the value of  $W$ .

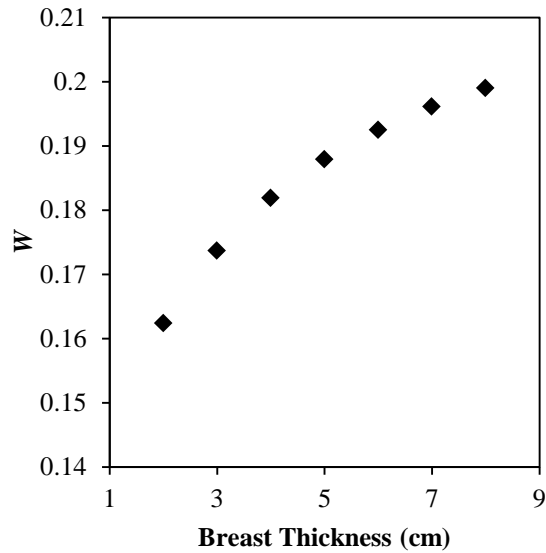


**Figure 15.** *The effect of breast thickness on  $W$ . In this example, a 46 kV HE beam with copper filtration was paired with a 26 kV LE beam with rhodium filtration at a LE dose fraction of 40%.  $W$  increases as the breast thickness increases due to beam hardening.*

### 3.1.2. $SDNR$

The  $SDNR$  for a Ag contrast agent was calculated using Equation 5. When  $SDNR$  was plotted against the mean energies of the LE and HE spectra, as in Figure 14, no correlation was observed. The effect of other compounding factors, such as dose and noise, mask any relationship that may otherwise exist. Therefore, the influence of individual imaging parameters on  $SDNR$  was studied to identify trends in the data.

The first parameter examined is the choice of filter material. The HE filter is always set to copper, as this is the only option available on the Hologic image acquisition system. Thus, the simulation exclusively selected copper for the HE spectrum and any reference to filter material or thickness from this point forward corresponds to the LE filter. The effect of the three filter material choices on the  $SDNR$  is



illustrated as a box plot in Figure 16. For these data points, the central mark is the median, the edges of the box are the 25<sup>th</sup> and 75<sup>th</sup> percentile, and the whiskers extend to the most extreme data. The data for each filter material encompass multiple energy pairs, dose fractions, and breast thicknesses. The data for aluminum, rhodium, and silver comprise 1753, 2349, and 2265 spectral pairs respectively. Both the mean and the maximum *SDNR* are slightly greater for the higher Z filter materials (rhodium, silver) when compared to aluminum. This can be attributed to the fact that the rhodium and silver filters are better able to position the mean energy of the LE spectrum immediately below the k-edge of Ag contrast material.

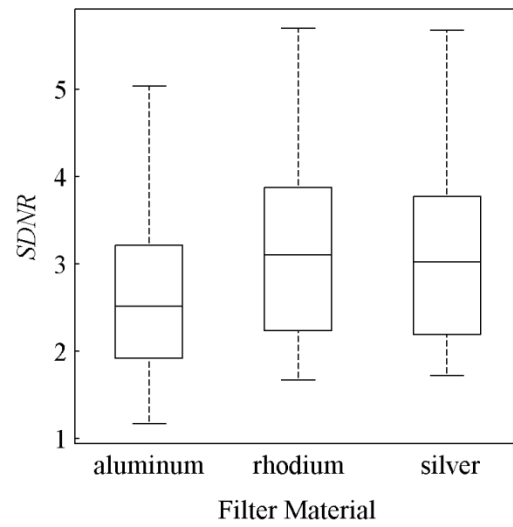


**Figure 16.** Box plot of *SDNR* for the various LE filter materials chosen in the simulation algorithm (aluminum, rhodium, and silver). The maximum *SDNR* is slightly greater for the higher Z filter materials (rhodium, silver) compared to aluminum. The box plots represent data spanning multiple energy pairs, breast thicknesses, and dose fractions

The effect of the LE dose fraction on the *SDNR* is illustrated as a box plot in Figure 17 using the same convention as Figure 16. Over the range plotted, the *SDNR* decreases with increasing dose to the LE image. While the drop in *SDNR* is gradual when the dose fraction is between 30 and 50%, the decrease is more drastic for larger dose distributions to the LE image. By increasing the dose fraction to the LE image,

the information obtained at the HE is reduced. In DE breast imaging, the HE image contains the majority of the signal arising from the contrast media. This HE information is necessary to provide sufficient  $SDNR$  of the contrast agent in the DE image. Dose fractions less than 30% are not shown as none of the imaging parameter combinations passed the mAs and  $SI$  criteria in constraints 3 and 4 (section 2.1). However, if these constraints are removed, we note that the  $SDNR$  reaches a maximum at a dose fraction of 20-30% and then decreases due to the small LE signal at a dose fraction of 10%.

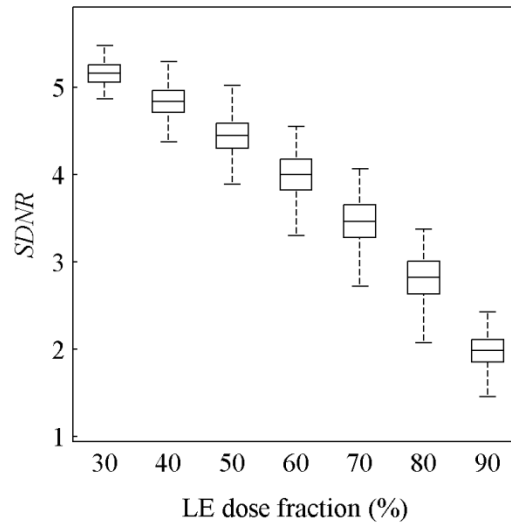


**Figure 17.** Box plot of  $SDNR$  for the various dose distributions to the LE image.  $SDNR$  decreases with increasing dose to the LE image. The box plots represent data spanning multiple energy pairs, filter combinations, and breast thicknesses.

In this study, the breast thickness was allowed to vary from 2 to 8 cm. In order to eliminate the influence of dose when comparing the various breast thicknesses,  $SDNR$  can be normalized by the square root of the mean glandular dose (MGD). Figure 18 plots the  $SDNR$  per square root MGD for all breast thicknesses. The  $SDNR$  per square root MGD decreases with increasing breast thickness. This decrease can be attributed in part to beam hardening. Although the mean energy of the LE and HE spectra both increase when passing through thicker breasts, the effect is greater for the LE spectrum, which results in a decrease

in the difference of mean energies between the two spectra. The reduction in spectral separation results in an increase in the proportion of the LE spectrum being positioned above the k-edge of Ag. This in turn reduces the effectiveness of the spectral pair to utilize the k-edge to obtain DE contrast.

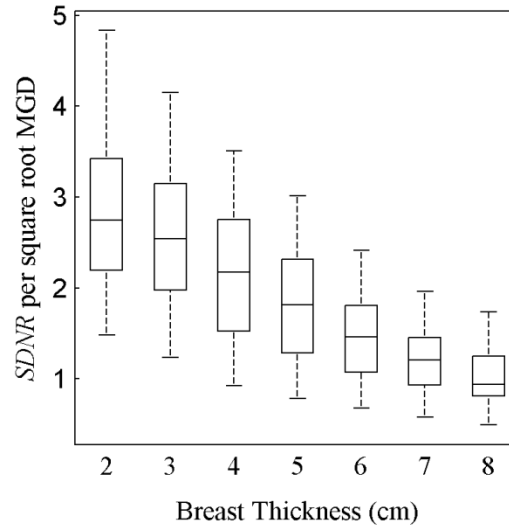


**Figure 18.** Box plot of  $SDNR$  per square root  $MGD$  for the breast thicknesses from 2 to 8 cm. Across the range of breast thickness values, the  $SDNR$  decreases by 67%. The box plots represent data spanning multiple energy pairs, filter combinations, and dose fractions

Figure 18 does not, however, display the clinical performance of the system as the dose is increased for thicker breasts to allow for adequate penetration through the tissue. The absolute  $SDNR$  value, shown in Figure 19, does not decrease as dramatically as the  $SDNR$  per square root  $MGD$ . Over the range of breast thicknesses studied, the absolute  $SDNR$  decreases by 35%, while the  $SDNR$  per square root  $MGD$  decreases by 63%. The doses selected by Hologic ensure that the clinical acquisition system is able to strike a balance between radiation dose and maintaining  $SDNR$  over a broad range of breast thicknesses.

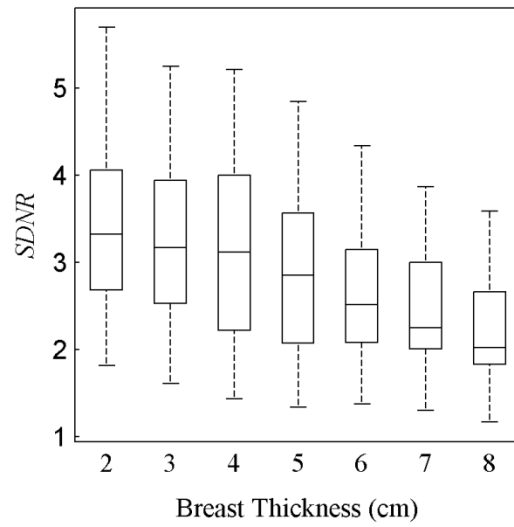


**Figure 19.** Box plot of  $SDNR$  for the breast thicknesses from 2 to 8 cm. As the thickness increases from 2 to 8 cm, the  $SDNR$  decreases by 36%. The box plots represent data spanning multiple energy pairs, filter combinations, and dose fractions

### III.A.3. $SDNR$ for $Ag$ vs. $I$ at all breast thicknesses

The single best (optimal) technique for each of  $Ag$  and  $I$  was selected for each breast thickness. The  $SDNR$  per square root MGD for either contrast material was obtained for each of these imaging parameter sets to yield 4 separate values: (i)  $Ag$  at optimal  $Ag$  imaging conditions, (ii)  $I$  at optimal  $I$  imaging conditions, (iii)  $Ag$  at optimal  $I$  imaging conditions, and (iv)  $I$  at optimal  $Ag$  imaging conditions. The optimal techniques for  $Ag$  and  $I$  are tabulated in Table 6 and Table 7, respectively. For  $Ag$ , the LE kV is maintained at 26 kV while the HE kV and LE dose fraction increase for increasing breast thickness. In the case of  $I$ , the HE kV is maintained at 49 kV while the LE kV and LE dose fraction increase for larger breasts.

**Table 6.** Optimal combinations of parameters to maximize *SDNR* of silver at breast thicknesses from 2 to 8 cm. The *LE kV* is maintained at 26 kV, while the *HE kV* and *LE dose fraction* is increased as the breast thickness increases.

Breast Thickness	HE kV	LE kV	LE filter	LE dose fraction
2	44	26	rhodium	30
3	45	26	rhodium	30
4	49	26	rhodium	30
5	49	26	rhodium	40
6	49	26	rhodium	60
7	47	26	rhodium	70
8	49	26	silver	70

**Table 7.** The optimal imaging conditions to maximize *SDNR* for iodine identified by the simulation algorithm. Where different, the values used by Hologic are presented in parentheses.

Breast Thickness (cm)	HE kV	LE kV	LE filter	LE dose
2	49	26	rhodium	30 (50)
3	49	26	rhodium	30 (50)
4	49	26 (28)	rhodium	30 (50)
5	49	26 (29)	rhodium	30 (50)
6	49	27 (31)	rhodium	50
7	49	28 (30)	rhodium (silver)	60
8	49	29 (32)	rhodium (silver)	60 (70)

The values of *SDNR* per square root MGD for each of the optimal techniques are plotted as a histogram for breast thicknesses between 2 and 8 cm in Figure 20. Over the range of breast thicknesses studied, the maximum *SDNR* for Ag is greater than I at their respective optimal imaging conditions. Ag has the greatest advantage for thinner breasts; at 2 cm, the *SDNR* per square root MGD for Ag is 28% higher than that of I. This advantage is reduced for thicker breasts; at 8 cm, the *SDNR* per square root MGD for Ag

is only 3% higher than that of I. This is due in part to the fact that the HE kV must be increased with increasing breast thickness to ensure that a sufficient number of x-rays pass through the breast and are recorded by the detector. Increasing the HE kV results in the mean energy of the spectrum being located further away from the k-edge of Ag, which in turn decreases the *SDNR*. This effect is not as prominent with I due to its higher k-edge and the optimal HE spectra was the maximum kV available on the Hologic system.

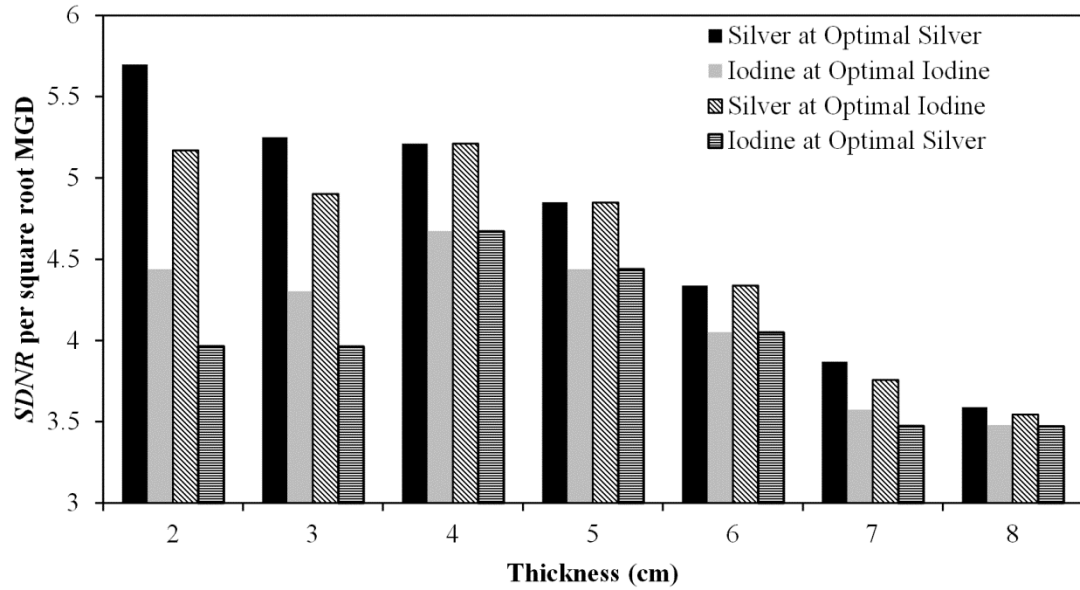


**Figure 20.** Comparison of simulated *SDNR* per square root MGD between silver and iodine at breast thicknesses between 2 and 8 cm. Silver performs better than iodine at their respective optimal conditions for every thickness studied. Moreover, silver performed better than iodine when imaged using the optimal conditions for iodine.

Interestingly, the *SDNR* per square root MGD for Ag at the optimal imaging conditions for I is consistently greater than the optimal *SDNR* for I using the same imaging conditions. Thus, despite the fact that the clinical system under study was explicitly designed for iodinated contrast agents, our results suggest that Ag performs better as a contrast agent than I for every thickness from 2 to 8 cm even when

using the imaging parameters that are optimal for I. Thus, a Ag contrast agent should be directly translatable to the clinic without any modification of the existing image acquisition systems or protocols.

### *3.2. Validating the Simulation Algorithm*

The simulation was validated by testing in physical phantoms using the ten spectral pairs tabulated in Table 5. These spectral pairs encompass a range of LE and HE kV, filter material, and dose fraction. They do not represent optimal imaging conditions, and were specifically chosen to provide a sufficiently, broad distribution of  $W$  and  $SDNR$  values with which to validate the simulation. The values of  $W$  and  $SDNR$  for Ag at each of the spectral pairs were obtained from the simulation. The spectral pairs were then used along with the method described in Section 2.3 to obtain experimental values of  $W$  and  $SDNR$ .

The simulated and experimentally obtained values of  $W$  are plotted parametrically in Figure 21. The data were fit to a linear regression (shown as a dashed line) with a Pearson correlation coefficient of 0.94. The slope of the fit is 1.02, while the y-intercept is 0.10. Similarly, the experimentally obtained values of  $SDNR$  using the contrast-embedded step phantom are compared to those obtained from the simulation algorithm in Figure 22. A Pearson correlation coefficient of 0.95 was obtained, and the slope and y-intercept of the linear fit are 0.18 and 7.83. The high Pearson correlation coefficients obtained for both  $W$  and  $SDNR$  indicate that the simulation algorithm is able to correctly predict the trends in signal intensity observed in the prototype Hologic Dimensions CEDE system. The algorithm does not, however, perfectly predict the signal intensity values and will need to include additional processes such as detector gain in a future refinement.

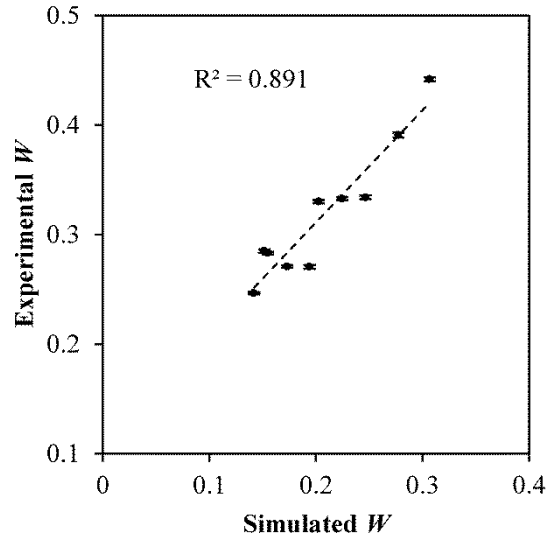


**Figure 21.** The experimentally-obtained values of  $W$  are highly correlated with the simulated values. A Pearson correlation coefficient of 0.89 was calculated for the two data sets. Error bars indicate standard deviation.

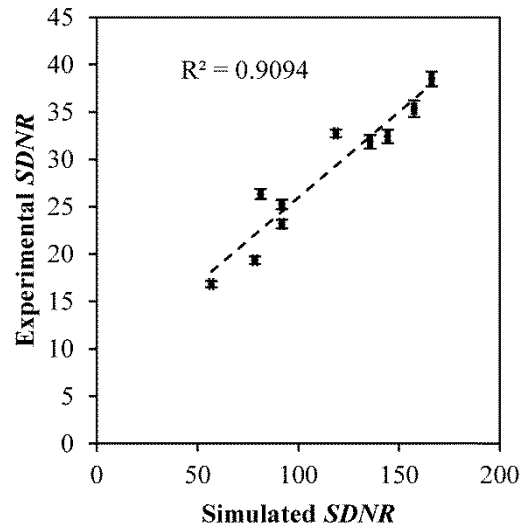


**Figure 22.** The experimentally-obtained values of  $SDNR$  correlate well with the simulated values. A Pearson correlation coefficient of 0.93 was obtained between the two data sets.



### 3.3. Comparing *SDNR* between Ag and I

Six optimal spectral pairs were identified to compare the *SDNR* between Ag and I contrast agents. The optimal imaging technique parameters for either contrast material were insensitive of the LE filter. The optimal technique for Ag is a 45 kV HE spectrum with a 26 kV LE spectrum at a dose fraction of 30%. While, that for I, is a 49 kV HE spectrum and a 26 kV LE spectrum at a dose fraction of 30%.

*SDNR* was calculated using the method in section 2.2 for equal volumetric concentrations of Ag and I using spectral pairs that comprised the optimal Ag and I imaging conditions for each of the three LE filter materials (aluminum, rhodium, and silver). An example of the LE, HE, and DE images of the contrast-embedded step phantom obtained for one spectral pair are shown in Figure 23. The contrast material is observed within the plastic tubing as a region of low-intensity pixel values. The values of *SDNR* obtained for each contrast material are plotted in Figure 24. When imaged at their respective optimal conditions, Ag outperforms I regardless of the filter material chosen. On average, the *SDNR* for Ag is 43% higher than that of I. The superiority of Ag is such that the lowest *SDNR* for Ag is still 34% higher than the highest *SDNR* for I. The superior *SDNR* of Ag can be attributed to the lower k-edge, which means that the HE spectrum is better positioned for optimal DE subtraction. A theoretical study using monoenergetic models <sup>96</sup> demonstrated that DE contrast is very sensitive to the placement of the HE value; the contrast decreases rapidly as the HE value is moved further from the k-edge of the contrast material. However, it is difficult to obtain HE spectra with mean energies in the range of 34 – 38 keV (above the k-edge of I) using a mammographic x-ray imaging system. In order to achieve suitable HE spectra, the imaging system would require kV values in excess of 50 kV with thicker filtration than is currently used in mammography.

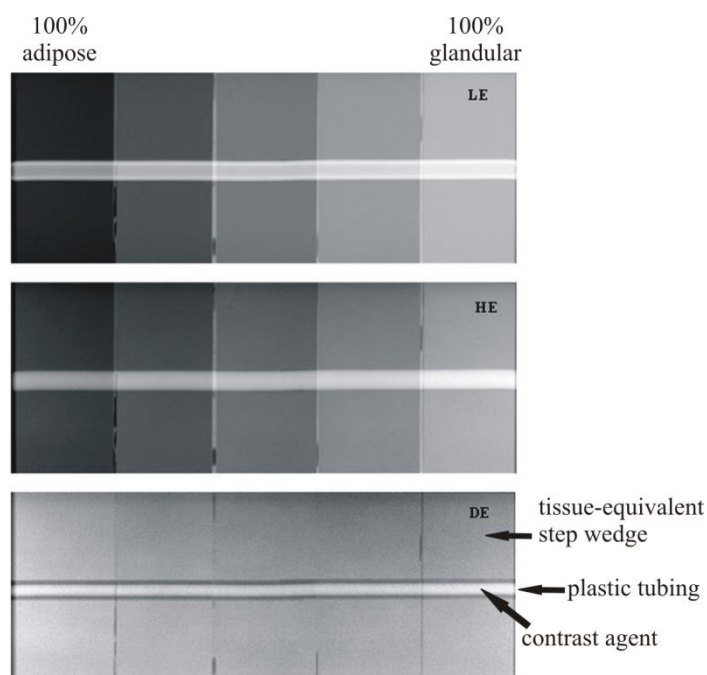


**Figure 23.** Example of LE, HE, and DE images of the contrast-embedded step-phantom with silver contrast material. The DE subtraction method removes the signal variation that exists in the background steps while maintaining the signal intensity within the contrast material.

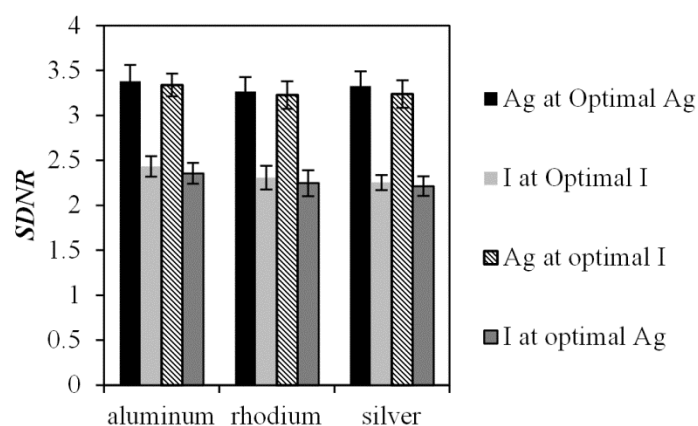


**Figure 24.** Comparison of SDNR between Ag and I for the optimal imaging parameters at each LE filter material. Ag performs better than I at their respective optimal imaging conditions, as well as the optimal conditions for iodine. The results are for a 3 cm step phantom.

Ag also performs better than I when imaging at the optimal conditions for I. For example, using the rhodium filter, the *SDNR* for Ag is 40% higher than that of I even though both were imaged at the optimal conditions for the latter. The maximum *SDNR* for I occurs at a HE kV value of 49. This is needed to ensure that a large portion of the spectrum is above the k-edge of I. However, even at the maximum kV value, a substantial portion of the HE spectrum is below the k-edge of I, and thus not contributing to the *SDNR*. When using a 49 kV HE spectrum with the copper filtration available on the Hologic CEDE system, 99% of the spectrum (in terms of the number of photons) is above the k-edge of Ag while only 78% is above the k-edge of I. The remaining 22% of the spectrum that lies below the k-edge of I cannot contribute to the *SDNR*, providing Ag with an advantage, even at the best possible conditions for I.

#### 4. DISCUSSION

Our previous monoenergetic study<sup>96</sup> identified several potential contrast materials as alternatives to I in CEDE breast imaging. That study predicted that materials with Z from 42 to 52 would provide the maximum contrast in DE imaging while still allocating a sufficient dose fraction to the LE image for clinically-acceptable anatomical images. Upon further consideration, Ag (Z = 47) was chosen due to the abundant availability of literature on the development of Ag nanoparticles, as well as the prevalent use of silver filters in CEDE imaging. The former is important as it provides a solid base from which to develop a prototype contrast agent, while the latter implies that the LE spectrum can be filtered to provide a mean energy as close to the k-edge of Ag as possible.

The purpose of this study is to test the applicability of a Ag contrast agent, predicted by the theoretical model, in a commercially-available dual-energy breast imaging system. This is an important predicate step before significant effort is expended on developing novel contrast agents. The model is constrained in that it does not attempt to search all the possible technique parameters (such as filter materials) that could be used but is restricted to those that are available on the system being studied. This was done to determine whether a Ag agent could replace an iodinated agent using an existing CEDE imaging system that was explicitly designed for iodine contrast imaging. The system under investigation in this work is the prototype Hologic Dimensions CEDE x-ray acquisition system. A polyenergetic simulation algorithm was developed to model the signal intensity and noise of the clinical system. The simulation

algorithm was then used to provide insight into the influence of imaging parameters on *SDNR* as well as identify techniques with which to compare the *SDNR* of Ag and I objectively.

The DE weighting factor,  $W$ , is plotted in Figure 14 for the various combinations of mean energies available on the prototype Hologic system. The polyenergetic model of  $W$  follows the same trend as the monoenergetic model;  $W$  decreases as the separation between the LE and HE values increases. It is important to note that, similar to the monoenergetic calculation,  $W$  does not change with the choice of contrast agent and is only dependent on the linear attenuation coefficient of adipose and glandular tissue. However, secondary effects such as scatter will introduce a thickness dependency on the overall attenuation of tissue, and consequently on the value of  $W$ . These effects are not included in the current simulation algorithm and may need to be taken into consideration for further refinement.

The simulation algorithm was also used to analyze the influence of the technique parameters on the *SDNR* of a potential Ag contrast agent. The choice of filter material was not shown to exert as important a role as previously thought. While the k-edge filters present in the system (silver and rhodium) exhibited slightly higher mean and maximum values of *SDNR* than the non-k-edge filter (aluminum), the difference between the two groups was minimal. The thicknesses of the silver and rhodium filters used on the Hologic machine are not sufficient to completely remove x-ray photons above their respective k-edges. However, excessively thick high-Z filter materials would require infeasibly large values of mAs to allow the spectra to penetrate the filter with sufficient fluence. However, given that the optimal LE spectra for Ag were limited to 26 kV, it may be possible to consider thicker filter thicknesses while compensating with high LE kV values.

The major influences on the *SDNR* of Ag were found to be the LE dose fraction and the breast thickness. An increase in the values of either of these parameters resulted in a decrease in the value of *SDNR*. By allocating a larger dose to the LE image, the technique is unable to utilize the contrast information that is present in the HE image and therefore results in a reduction in *SDNR*. Thus, while it is common practice to equally distribute the dose between the LE and HE images, our results suggest that the information contained in the HE image is more important to the *SDNR* of the contrast agent. However,

additional practical considerations such as the quality of the anatomical image for diagnostic purposes must be taken into consideration before accepting the use of a lower dose fraction to the LE image. Therefore, a compromise must be struck between obtaining a good quality anatomical image to aid in the diagnosis, and the visualization and characterization of contrast-enhanced anatomical structures.

As previously mentioned, an increase in the breast thickness also results in a decrease in the value of *SDNR*. This is due to the increase in the mean energy of the HE spectrum as a result of beam hardening and the kV value being increased to penetrate through thicker tissue. As the HE spectrum is positioned further away from the k-edge of Ag, the ability of the DE technique to fully utilize the k-edge for contrast decreases. However, this effect can be reduced by increasing the allocated dose for thicker breasts – a practice that is clinically implemented. By following the dose scheme utilized by Hologic for their CEDE examinations, it is possible to maintain the *SDNR* of a Ag contrast over a substantial range of breast thicknesses, with only a slight degradation observed for thicker breasts (see Figure 19).

The simulation algorithm identified the techniques that maximized the *SDNR* for Ag and I contrast agents over the range of breast thicknesses studied (Table 6 and Table 7, respectively). For Ag, the optimal HE kV value is increased from 44 to 49 as breast thickness increases, while the LE kV value is maintained at 26. A rhodium filter is optimal, except for the largest breast thickness studied where a silver filter is preferred. The LE image, consisting of a 26 kV tungsten spectra filtered with rhodium is a classic example of a soft-tissue anatomical image obtained clinically. Therefore, the LE image would provide excellent anatomical and spatial localization of structures, (calcifications, lesions), while the DE image can be used for quantitative analysis of contrast agent uptake. The optimal LE kV value agrees with the previous theoretical modeling using monoenergetic simulations [19] that showed an optimal contrast LE value of 18 keV; roughly the mean energy of a 26 kV spectrum.

Conversely, the optimal HE kV for I is maintained at 49, while the LE kV value is increased from 26 to 29 as breast thickness increases. A rhodium filter is used throughout. The higher k-edge of I requires the HE kV value to be set to the maximum in an effort to ensure that the majority of the HE spectrum is above the k-edge of I. As a result, the LE kV value is forced to increase for thicker breasts. While this

increase is not substantial, the LE anatomical image at thicker breasts may not provide the same level of detail as their thinner counterparts because the difference in attenuation between adipose and glandular tissue is reduced for higher LE kV values. The optimal technique parameters for  $I$ , as determined by the model, also presents an interesting opportunity to evaluate the technique parameters currently used by Hologic. By and large, the optimal simulated technique parameters agreed with those used clinically. There are, however several instances, where the techniques differ. The minimum LE dose fraction used by Hologic is 50%, while that used by the model is 30%. We presume that Hologic set this minimum dose fraction primarily to ensure a good quality LE anatomical image. In addition, the LE kV is increased faster as a function of breast thickness on the clinical system by Hologic than predicted by the model. These differences are minimal and the large level of concordance between the two techniques helps to further validate the results of our algorithm.

The  $SDNR$  at each of the optimal techniques for Ag and I can be compared by examination of the simulation and experimental results (Figure 20 and Figure 24, respectively). The simulation can be used to compare the two contrast agents over the range of breast thicknesses; a singular thickness was used for the experimental validation. Both methods support the same two conclusions:

1. If the established technique parameters that are currently utilized in the clinic are considered, Ag provides a higher value of  $SDNR$  than I. This suggests that Ag is better suited as a DE imaging agent compared to I in the mammographic energy range. A biologically stable Ag imaging agent could be directly translated from development to clinical implementation without the need for modification or redesign of image acquisition systems.
2. If the technique parameters are slightly modified to reflect the lower k-edge of Ag, the difference in  $SDNR$  between the two materials would be further increased. These modifications would consist primarily of lower HE and LE kV values. The lower LE kV value may serve to boost the diagnostic application of the CEDE technique further by providing a good quality anatomical image with excellent soft tissue contrast.

There are, however, several improvements that can be made to the simulation algorithm. For example, the algorithm does not incorporate the effects of scatter. The energy dependence of Compton and coherent scattering may have implications on image quality when using a Ag or I imaging agent. The detrimental effect of scatter should be greater for *I* because of the higher LE and HE kV values used. The greater effect of scatter will result in a reduced *SDNR* for I compared to Ag than currently predicted. The algorithm will need to be modified with a Monte Carlo-type x-ray interaction simulation to adequately test this hypothesis. In addition, the model is unable to exactly predict the signal intensity of a particular imaging technique. This can be remedied by incorporating the gain factors involved in the conversion of x-ray photons attenuated by the detector to a digital value. Once signal intensity is predicted exactly, the algorithm could be used in assisting the system design process by identifying optimal filter materials and thicknesses for imaging either a Ag or *I* contrast agent.

## 5. CONCLUSION

This work explores the use of a Ag imaging agent as an alternative to *I* in CEDE x-ray breast imaging. Iodinated agents are used extensively in x-ray projection imaging and display excellent biocompatibility and stability within the body. However, the lower energies available to clinical DE x-ray breast imaging compared to other organs in the body suggests that an alternative material may be better suited. Previously conducted theoretical analysis demonstrated that materials with atomic numbers from 42 to 52 should be explored as potential candidates. From these materials, Ag was chosen for further investigation. The prominence of silver filters in breast x-ray imaging devices and Ag nanoparticles in consumer products suggested that a Ag-based imaging agent might have practical application in CEDE x-ray breast imaging.

An algorithm was developed in MATLAB to simulate the image acquisition of the Hologic Dimensions CEDE system. The *SDNR* of Ag was compared to that of I for imaging parameters that comprised the optimal conditions for either material. Not only does Ag perform better than I when imaged at their respective optimal conditions, but Ag is able to provide greater *SDNR* than I when imaged with protocols that are optimal for I. This means that a Ag contrast agent could be translated to the clinic without

modification of machine or protocol. Work into developing a biologically-stable Ag nanoparticle agent, although outside of the scope of this manuscript, is warranted and preliminary data shows promise <sup>104</sup>.



## CHAPTER 4

### ABSTRACT

Through prior analytic modeling and experimental validation, we have demonstrated that silver could provide higher values of signal difference-to-noise ratio compared to iodine in dual-energy (DE) x-ray breast imaging. A biologically stable silver imaging agent could be translated to the clinic without the need for modification of protocol or imaging system. For this purpose, a prototype polyethylene glycol-coated silica-silver (PEG-SiAg) nanoparticle was manufactured using a three step-process: (1) synthesis of silver core, (2) silica encapsulation, and (3) PEG stabilization. The final diameter of the particles was measured to be  $102 (\pm 9)$  nm. Subcutaneous injection of the particles into athymic mice demonstrated that the DE technique is able to discriminate between the imaging agent and the underlying bony structures. Intraperitoneal injection of the particles resulted in the clear identification and segmentation of the peritoneal organs after the surrounding space had been filled with the silver contrast material. The particles were eventually removed from the circulation (blood half-life: 13 – 17 minutes) and accumulated in macrophage-rich organs, such as the liver, spleen and lymph nodes. These data are the first to demonstrate the application of a silver imaging agent as a DE contrast agent in a living system, and serves as the foundation for further improvements to the design of a prototype silver contrast material.

## 1. INTRODUCTION

Dual-energy (DE) x-ray imaging increases the conspicuity of radiographic imaging agents by suppressing the soft-tissue signal variation in the background. Once the anatomic structures have been removed, it is possible to segment and quantify the signal from the exogenous imaging agent accurately. Clinically, DE imaging in the breast has been shown to aid visualization of lesions that are otherwise mammographically occult as well as to provide functional blood flow information consistent with magnetic resonance imaging - the current gold standard in functional breast imaging<sup>28, 32-35</sup>. The most widely-used implementation of DE is k-edge imaging – two distinct energy windows [low (LE) - and high-energy (HE)] are placed on either side of the k-edge of the contrast material. Through a weighted subtraction of the two images, a DE image consisting solely of the signal arising from the contrast agent can be produced.

Currently, DE imaging is performed with an iodinated contrast agent. Water-soluble iodinated radiographic agents were first tested in 1928<sup>40, 41</sup>. These agents were initially developed for intravenous urography, and were the first major step in the use of radio-opaque materials to diagnose disease. Over the last century, the initial design of iodinated agents has been modified to improve biocompatibility by carefully altering their ionicity and osmolarity. The agents used today are variants of a tri-iodinated benzene ring with substitutions for improved solubility. These agents are extremely stable in the body, and can resist degradation over long periods of time.

However, current agents are limited with several inadequacies. The relatively high k-edge of iodine (33 keV), while ideal for higher energy radiographic procedures, is less well suited for the lower range of energies (26 to 49 kV) used in DE breast imaging. It is therefore difficult to obtain a HE spectrum that does not contain a substantial number of x-ray photons below the k-edge of iodine which do not contribute to the DE contrast. For example, it was determined that 22% of a HE spectrum is below the k-edge of iodine when the maximum kV setting, that is typically permitted on clinical DE breast imaging systems, was applied. In addition, there are several practical considerations that limit the effectiveness of current iodinated agents. The small size of the current agents results in rapid filtration by the kidneys, and therefore necessitates immediate post-injection imaging<sup>61</sup>. Filtration by the kidneys has been linked to contrast-mediated nephropathy in patients with preexisting renal insufficiency, such as diabetes

mellitus<sup>67,68</sup>. Furthermore, the percentage of the injected dose that reaches the target site is low because these agents lack an appropriate biomolecular surface layer to prevent the non-specific binding of blood serum proteins.

In Chapter 3, we have developed a monoenergetic model that helped identify silver (Ag) as a new candidate material for DE x-ray breast imaging. The model predicted that the maximum DE contrast-to-noise ratio (CNR) for silver would be comparable to that of iodine, while requiring operating conditions that are more clinically-suited to imaging the breast. The model was expanded to include simulations of polyenergetic spectra available on a prototype commercial DE image acquisition system. The simulation was used to compare the signal difference-to-noise ratios of equimolar concentrations of iodine and silver contrast agents. If the established technique parameters that are currently utilized in the clinic are considered, silver provides a higher value of *SDNR* than iodine. If the technique parameters are slightly modified to reflect the lower k-edge of silver, the difference in *SDNR* between the two materials would be increased. This suggests that a biologically stable silver imaging agent could be directly translated to the clinic without the need for modification of protocol or imaging system.

Nano-silver represents the largest (25%) and fastest growing category of nanotechnology-based consumer products<sup>76</sup>. As of 2013, there were 313 unique silver nanoparticle-based consumer products available, compared to 184 and 67 for the next highest materials (titanium and silica, respectively)<sup>76</sup>. The majority of the silver nanoparticle consumer applications make use of the broad spectrum antimicrobial and unique optical scattering effects of silver<sup>77-82</sup>. To our knowledge, there has been no work reported on the development of silver nanoparticles as DE contrast agents. This may, in part, be due to the acute toxicity associated with silver nanoparticles. Navarro *et al.*<sup>105</sup> studied the toxic effects of silver nanoparticles on the photosynthetic function of *Chlamydomonas reinhardtii*. Increasing concentrations of silver nanoparticles reduced the algal photosynthetic yield with an average EC<sub>50</sub> (half maximal effective concentration) of 3300 nM after 1 hour of exposure, compared to 188 nM for a silver nitrate solution. The authors postulated that the toxicity is a result of the interaction of the particles with algae which resulted in the formation of Ag<sup>+</sup> ions. The toxic effects observed are related to damage at the cell membrane, oxidative stress, or interaction

of the  $\text{Ag}^+$  ions with proteins and enzymes.<sup>106, 107</sup> Similar results were demonstrated with fish and rat liver cells<sup>108, 109</sup>.

To address the formation of toxic  $\text{Ag}^+$  ions, we proposed a method to encapsulate a silver nanoparticle core within a larger shell to prevent interaction of the silver surface with biomolecules that may result in the oxidation of the silver atoms. The final design of the prototype silver nanoparticle contrast agent is shown in Figure 25. The agent consists of a solid silver core encapsulated by a silica shell. Silica was chosen as the encapsulation material due to the abundant literature available on the coating of colloidal metal nanoparticles with silica and the relative simplicity of the methodology<sup>110</sup>. The silica-silver nanoparticles are then stabilized and made biocompatible through the addition of a layer of polyethylene glycol (PEG). PEG has been demonstrated to improve the stealth characteristics of nanoparticles *in vivo* by preventing the adsorption of serum proteins and uptake by the mononuclear phagocyte system<sup>111, 112</sup>. The purpose of this chapter is to describe the manufacture, characterization and testing of this prototype silver-based contrast agent in living systems.

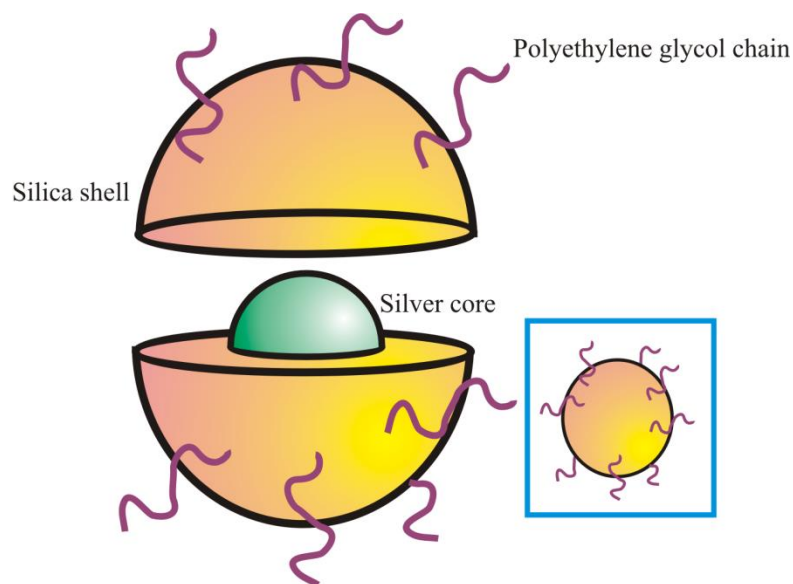


**Figure 25.** Design of prototype silver nanoparticle imaging agent.

## 2. METHODS

Polyvinylpyrrolidone (Average mol wt: 10,000), silver nitrate, ammonium hydroxide, tetraethoxysilane, and 3-aminopropyl-trimethoxysilane were purchased from Sigma-Aldrich (St Louis, MO). Polyethylene glycol-N-hydroxysuccinimide was purchased from Creative PEG Works (Winston Salem, NC). All other chemicals were purchased from Fisher-Scientific (Waltham, MA). Athymic, female mice (6-8 weeks) were purchased from Charles River Laboratory (Wilmington, MA). All animal studies were approved by the Animal Care and Use Committee at the University of Pennsylvania.

### 2.1 *Synthesis of silver core*

The silver core is synthesized as described by Silvert *et al.*<sup>98</sup>. 1.5 g of polyvinylpyrrolidone was dissolved in 75 mL of ethylene glycol in a 250 mL roundbottom flask fitted with a condensation apparatus and left overnight to mix. 50 mg of silver nitrate ( $\text{AgNO}_3$ ) was then added. The mixture was heated to 120 °C at a rate of 1 °C/minute. The reaction was allowed to proceed at this temperature for 1 hour. The mixture was then cooled to room temperature. The PVP-stabilized silver nanoparticles were purified by adding acetone to the reaction vessel and centrifuging at 4000 xg for 15 minutes. The particles were then resuspended in ethyl alcohol for further modification.

### 2.2 *Silica encapsulation of silver core*

The PVP-stabilized silver cores were encapsulated within a silica (Si) shell using the method described by Graf *et al.*<sup>110</sup>. 415  $\mu\text{L}$  of ammonium hydroxide was added to 9.438 mL of PVP-stabilized silver nanoparticles, after which 75  $\mu\text{L}$  of tetraethoxysilane (TES) in 675  $\mu\text{L}$  of ethyl alcohol is added. The reaction is then allowed to proceed in the dark for 12 hours. The silica-silver nanoparticles are purified by centrifugation at 19,000 xg for 15 minutes, and resuspended in ethyl alcohol. The silica-encapsulated nanoparticles are functionalized with terminal amine groups to attach the PEG ligands: the nanoparticles are reacted with 3-aminopropyltrimethoxysilane under gentle stirring for 12 hours at room temperature, after which the temperature of the reaction is brought up to 55 °C for 1 hour. The amine-terminated silica-silver particles are purified using the same centrifugation procedure described previously.

### *2.3 PEG-stabilization of silica-silver nanoparticles*

The amine-terminated silica silver nanoparticles are resuspended in phosphate buffered saline (PBS). The particles are then mixed with a mass excess of PEG-N-hydroxysuccinimide (NHS) (PEG molecular weight: 3,400 Da) and allowed to react for 2 hours under vigorous stirring at room temperature. The PEG-coated silica-silver nanoparticles (PEG-SiAg) were then purified using a combination of centrifugal and 0.2  $\mu\text{m}$  surfactant-free cellulose acetate (SFCA) syringe filters to remove any unwanted byproducts and excess reagents.

### *2.4 Nanoparticle Characterization*

The physical diameter of the nanoparticles was measured using transmission electron microscopy (TEM). 10  $\mu\text{L}$  of the nanoparticle solution was placed on a carbon film-coated copper grid and allowed to dry for 2 hours. The grid was then imaged using a JEOL 1010 (JEOL, Peabody, MA, USA) electron microscope. The accelerating voltage was set to 80 kV with a magnification of 75x. The diameter of 100 particles were measured, and the average diameter of this sample was calculated. The light scattering properties of the nanoparticles was measured using a Malvern Instruments Zetasizer (Malvern Instruments, Malvern, Worcestershire, United Kingdom). 700  $\mu\text{L}$  of the nanoparticle solution was placed in a plastic disposable cuvette and the hydrodynamic size and zeta potential of the particles was determined.

### *2.5 Pharmacokinetic / Biodistribution study*

PEG-SiAg were injected intravenously into three athymic female mice between 8 and 10 weeks old at a dose of 400 mg/kg. 10  $\mu\text{L}$  samples of blood were obtained pre-injection and at various time points post-injection (5 mins, 10 mins, 15 mins, 30 mins, 1 hour, 2 hours, 4 hours, 8 hours, 24 hours). The animals were sacrificed 24 hours after injection of the particles. The organs of the animals were harvested and digested, along with the blood samples, using 1 M nitric acid at room temperature for 1 hour. The silver content was then measured using inductively-coupled plasma optical emission spectroscopy (ICP-OES).

## 2.6 DE imaging of mice using PEG-SiAg

PEG-SiAg were administered at a dose of 8 mg of silver via intravenous, intraperitoneal and subcutaneous injections into three athymic female mice. The mice were maintained under anesthesia for the entirety of the imaging procedure using inhaled isoflurane. The animals were imaged using a GE Senographe DS mammography unit (GE Healthcare, Little Chalfont, United Kingdom). The HE and LE spectra were selected as 49 kV rhodium target with rhodium filtration and a 26 kV molybdenum target with molybdenum filtration, respectively. The LE kV is set just below the k-edge of Ag, while the HE kV is set to the maximum possible on the imaging system to minimize overlap between the two spectra. Regions of interest were chosen in the soft tissue (s) and bone (b) in the LE and HE images. The weighting factor,  $W$ , was calculated using the average signal intensities ( $SI$ ) of the two regions:

$$W = \frac{\ln(SI_b^{HE}) - \ln(SI_s^{HE})}{\ln(SI_b^{LE}) - \ln(SI_s^{LE})}.$$

The DE image is calculated as the weighted logarithmic subtraction between the LE and HE image.

$$DE = \ln(HE) - W \times \ln(LE)$$

Prior to the subtraction, the HE image is registered to the LE image using the intensity-based, iterative, registration algorithm, “imregister” found in the Image Processing Toolbox in MATLAB (MathWorks, Natick, MA). The registration applied a ‘similarity’ transformation, consisting of translation, rotation, and scaling to the HE image. The metric chosen to compare sequential iterations of the registration is the Matte’s mutual information coefficient. An iteration that maximizes this metric will yield the optimal alignment of the LE and HE images. The optimization method used was “one plus one evolutionary” whereby the parameters from the last iteration (parent) are perturbed to yield new parameters (child). If the new parameters yield higher values of the mutual information coefficient, the child becomes the parent, and the process is repeated. Otherwise, the parent remains the parent and a less aggressive perturbation to the parameters is applied. The optimization method in MATLAB has several parameters whose values may be modified (growth factor, epsilon, initial radius, and maximum iterations). The registration between the LE

and HE images was applied using the default values of epsilon, and initial radius while the values of growth factor and maximum iterations were changed to 1.1 and 500 respectively (originally: 1.05, 100). These parameter values were chosen empirically to yield the best results when qualitatively comparing the LE image

### 3. RESULTS

#### 3.1 Characterization of nanoparticles

The physical diameter of the nanoparticles at various stages of the synthesis was measured using transmission electron microscopy (TEM). The PVP-coated silver cores are shown in Figure 26a. The particles consist of solid, spherical silver cores with an average diameter of  $39 \pm 6$  nm (mean  $\pm$  standard deviation). After silica encapsulation, the total diameter of the nanoparticles is  $102 \pm 9$  nm (Figure 26b). The majority of the silica-silver nanoparticles consisted of a single silver core covered by a spherical silica shell. The PEG layer of the final PEG-SiAg is electron-transparent and thus does not appear in the TEM micrograph (Figure 26c). The hydrodynamic diameter and zeta potential of PEG-SiAg was determined to be 115.3 nm (polydispersity index of 10%) and 0.065 mV, respectively. The difference of 13.2 nm between the physical and hydrodynamic diameters help support the assertion that the PEG ligands were successfully attached to the Si surface.

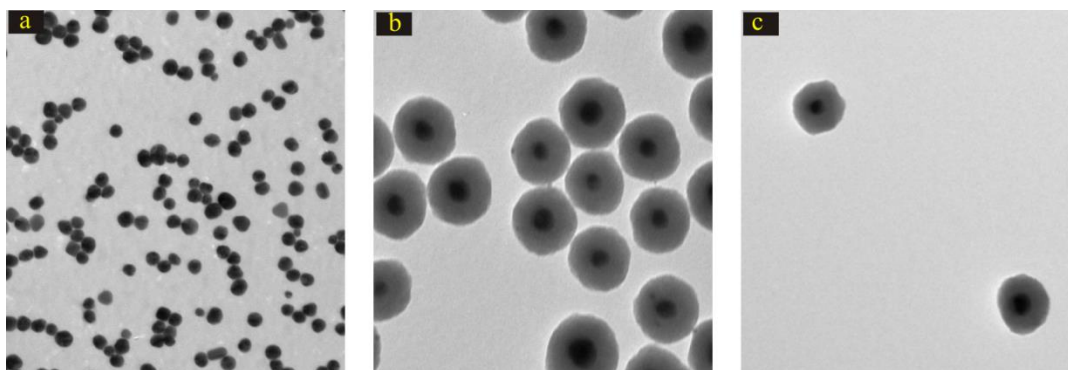


**Figure 26.** TEM micrographs of (a) polyvinylpyrrolidone-coated silver cores, (b) silica-encapsulated silver cores, and (c) polyethylene glycol-silica-silver nanoparticles (PEG-SiAg)



### 3.2 Blood Clearance / Biodistribution

The blood clearance and biodistribution results are shown in Figure 27 and Figure 28, respectively. The particles are rapidly removed from the bloodstream with a half-life of 13 minutes, with only trace amounts of silver nanoparticles circulating 24 hours after injection. The particles are taken up, presumably through macrophage-mediated endocytosis, by the liver, spleen, and lymph nodes. Significant accumulation of silver was also detected in the pancreas, large bowel and muscle.

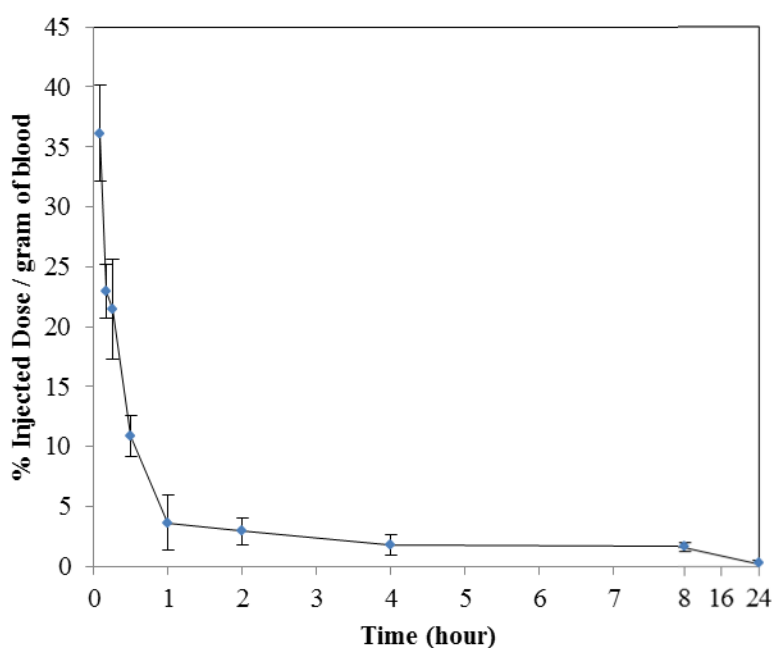


**Figure 27.** Blood clearance of PEG-SiAg nanoparticles after intravenous injection into female mice. The particles are rapidly removed from the bloodstream with an initial half-life of 13-17 minutes. Error bars represent standard deviations.

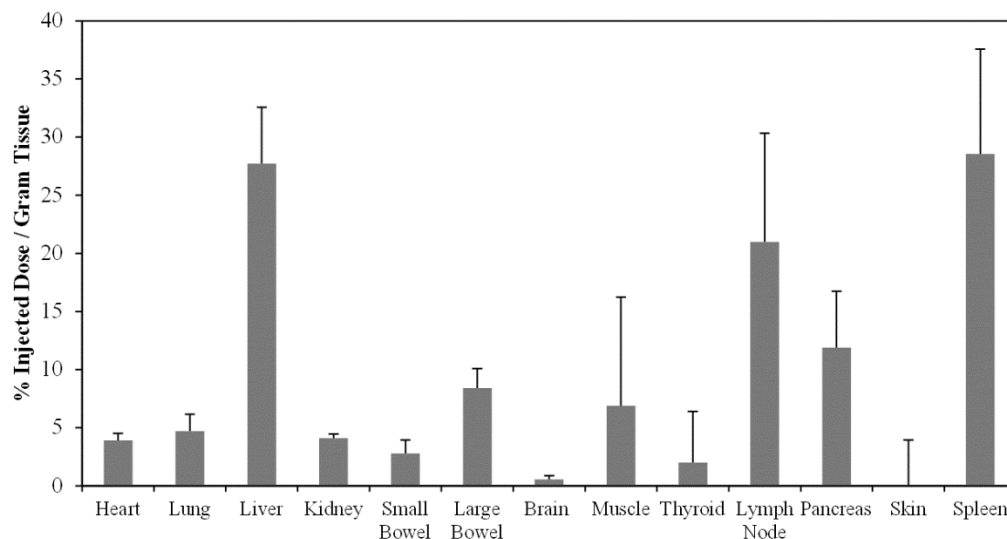


**Figure 28.** Biodistribution of PEG-SiAg nanoparticles, 24 hours after intravenous injection into female mice. The majority of the particles are located in the liver and spleen, in addition to accumulation in the lymph nodes and pancreas. The remaining organs showed very little uptake of the silver particles. Error bars represent standard deviation.

### 3.3 DE imaging of mice – Subcutaneous

Examples of the LE, HE, and DE images of the animal after the subcutaneous injection of the PEG-SiAg are shown in Figure 29, where the site of injection is indicated with the yellow arrow. The single-energy images (LE and HE) show good contrast between the various tissue types, allowing for straightforward discrimination between bone and soft tissue. The anatomical contrast is, by and large, removed in the DE image.

The residual contrast that remains in the DE image can be attributed to three sources: The DE subtraction method is sensitive to the total thickness of tissue in the beam path. As the total thickness of materials in the beam path varies, the weighting factor needed to remove the dependence of the DE signal intensity on these materials varies. This is remedied in clinical DE breast imaging by applying compression to the breast to allow for a homogenous thickness of imaged tissue. This is difficult to replicate in a mouse

model, and therefore regions of the mouse with varying thickness are not optimally subtracted. The subtraction method assumes a singular attenuation coefficient value for each of soft tissue and bone, when there are varying compositions of these tissues within the mouse, each with its own unique attenuation coefficient. Finally, regions of high intensity (white) towards the head of the animal are a result of registration errors between the LE and HE images.

The contrast material can be identified in all three images. However, the DE image is able to discriminate between the injected nanoparticles and the underlying anatomic bone structures. The boundaries of the bolus injection can be easily identified and separated from the surrounding tissue structures. The *SDNR* of the silver contrast material (Ag) compared to the background bone (B) tissue was calculated as:

$$SDNR = \frac{SI^{Ag} - SI^B}{\sigma^B},$$

where *SI* is the average signal intensity and  $\sigma$  is the standard deviation of a region of interest chosen in either the silver contrast material or bone. The *SDNR* was calculated as 1.14, 0.87, and 8.75 in the LE, HE, and DE images respectively, indicating a 7 to 9 factor improvement in the contrast of the silver in the DE image compared to the single-energy images.

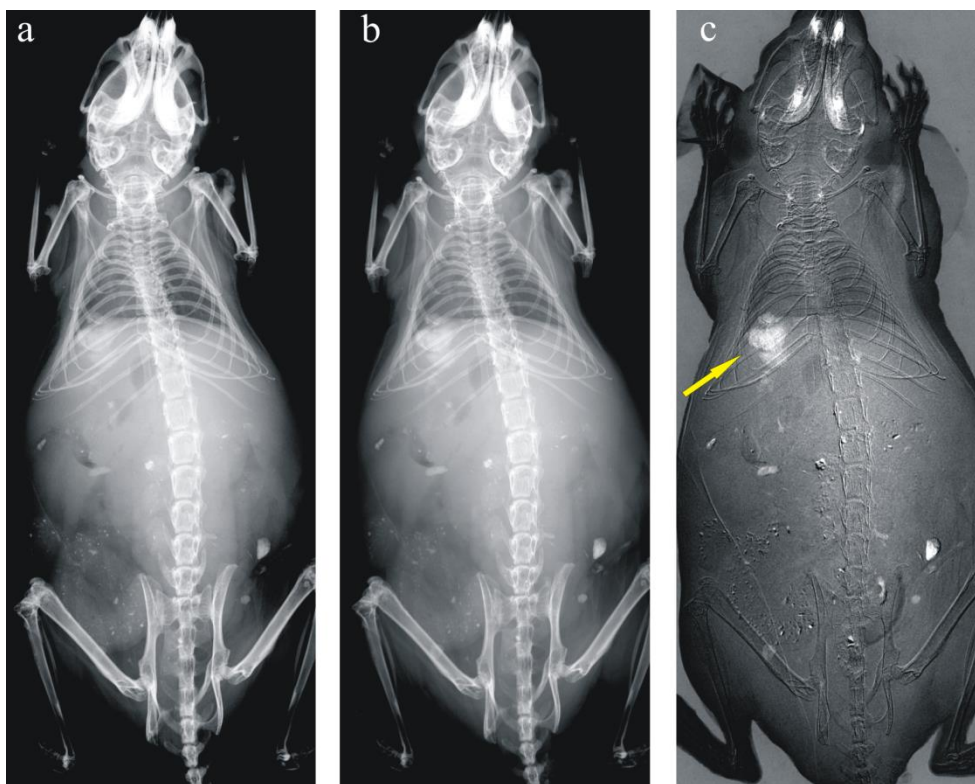


**Figure 29.** *LE (a), HE (b), and DE(c) images of the mouse immediately after administration of PEG-SiAg via subcutaneous injection (yellow arrow).*

### *3.4 DE imaging of mice – Intraperitoneal*

Examples of the LE, HE, and DE images of the animal after the intraperitoneal injection of the PEG-SiAg are shown in Figure 30. The suppression of the anatomical signal variation in the DE image allows for clear identification and segmentation of the peritoneal organs after the surrounding space has been filled with the silver contrast material. The progression of the contrast in the peritoneal cavity over time is illustrated in Figure 31. The outline of the peritoneal organs (example indicated by arrows) decreases steadily over time, as the contrast agent is taken up into the bloodstream. Little contrast is observed in the peritoneum 50 minutes after the injection of the nanoparticles.

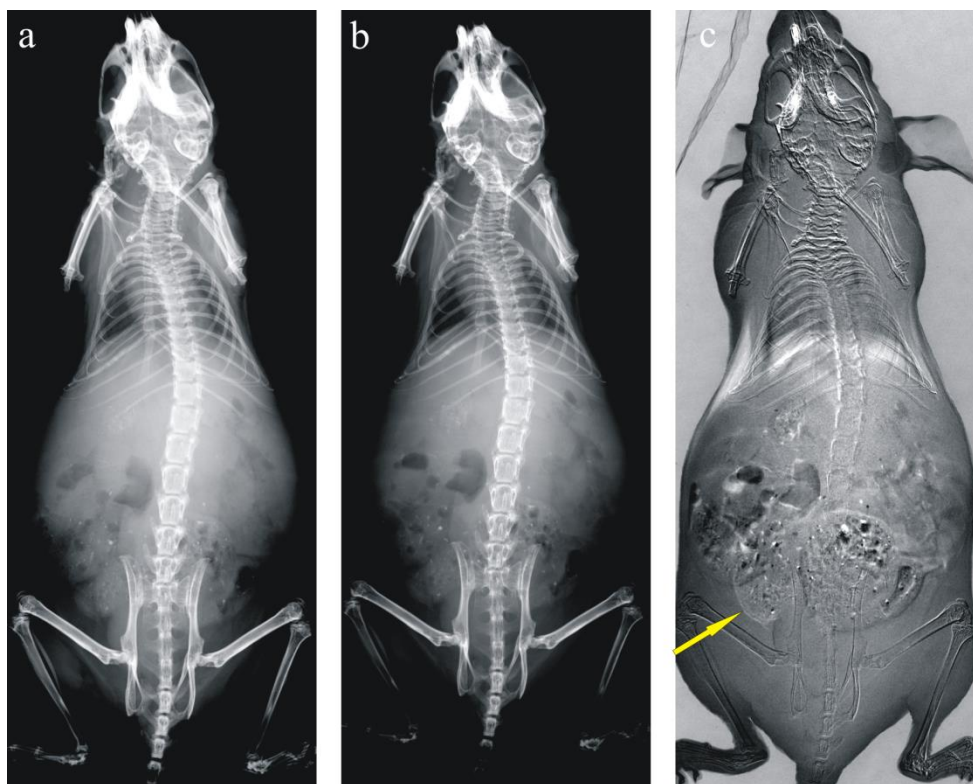


**Figure 30.** *LE (a), HE (b), and DE (c) images of a mouse immediately after administration of PEG-SiAg via intraperitoneal injection. The contrast from the silver in the DE image allows for the identification and segmentation of various peritoneal organs.*

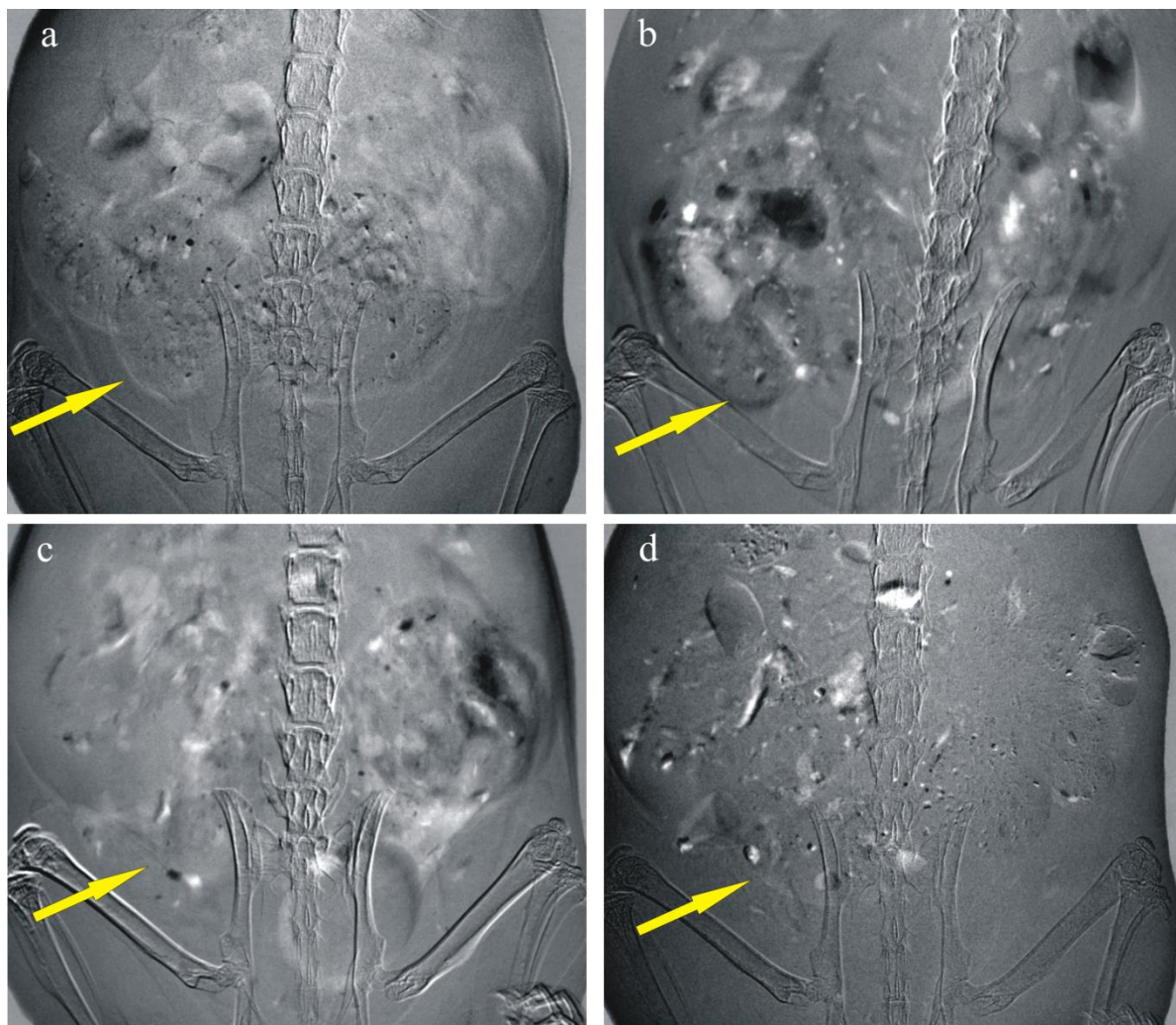


**Figure 31.** *Progression of the contrast as a result of the PEG-SiAg in the DE images. (a) 5 minutes, (b) 20 minutes, (c) 40 minutes, and (d) 50 minutes post-injection. The outline of the peritoneal organs decreases over time, until very little contrast is observed 50 minutes after the injection of the particles.*

In all cases, the animals are still alive at the time of completing this chapter, roughly 2 months after the injection of the particles.

#### 4. DISCUSSION

Through analytic modeling, we have previously concluded that silver represents a novel, potential alternative to iodine as a DE contrast material. The model demonstrated that little or no modifications in imaging system or protocol are needed to obtain a higher contrast with silver, implying that a viable silver

contrast agent could be rapidly translated to the clinic. The proposed design of the silver contrast agent consisted of a (a) silver core – for DE contrast, (b) silica shell – to prevent the formation of toxic  $\text{Ag}^+$  ions, and (c) polyethylene glycol surface layer – to improve hydrophilicity and biocompatibility. The purpose of this study was to synthesize, characterize and test the performance of the prototype polyethylene glycol-silica-silver (PEG-SiAg) nanoparticle in mice. This work is intended to serve as a point of reference for further improvements to the design of the nanoparticle as well as further testing of the existing design.

The PEG-SiAg nanoparticles were synthesized using previously described methods found in the literature<sup>98, 110</sup>. The particles were spherical in shape and consisted of a silver core with an average diameter of  $39 \pm 6$  nm encapsulated in a silica shell with a total diameter of  $102 \pm 9$  nm as shown in Figure 26. The particles are relatively monodisperse with an average polydispersity index of 10%, as measured by dynamic light scattering. The polydispersity index is a measure of the heterogeneity of sizes of nanoparticles in a mixture, with lower values indicating a more monodisperse solution. Uniformity in the size of the nanoparticles suggests that the synthesis methods are stable and reproducible, and can allow for larger scale synthesis of the contrast agent while ensuring similar overall characteristics.

An important point to note regarding the design of the PEG-SiAg nanoparticle is the relatively large size of the silica shell compared to the rest of the nanoparticle. A silica shell with an inner and outer diameter of 39 and 102 nm, respectively means that each nanoparticle consists, by weight, of only 19% silver. The majority of an injected dose of PEG-SiAg nanoparticles therefore consists of silica, which does not contribute to the primary function of the agent which is to provide DE contrast. A detailed toxicity assay with PEG-SiAg nanoparticles of varying silica shell thicknesses will need to be conducted to determine the optimal silica shell thickness which reduces the oxidation of the silver core to acceptable limits while providing a substantial dose of silver per total dose of injected nanoparticles.

The pharmacokinetic and biodistribution profile of the PEG-SiAg nanoparticles in athymic mice is shown in Figure 27 and Figure 28, respectively. The particles are rapidly removed from the bloodstream, with an estimated vascular compartment half-life of 13 minutes. At 24 hours post-injection, the majority of the particles are located in the liver, spleen, and lymph nodes in addition to appreciable amounts in the

large bowel, muscle, and pancreas. The clearance profiles can be explained, to a large extent, by the size of the nanoparticles. Particles with primary dimensions on the order of 100 – 200 nm have been shown to be taken up primarily by mononuclear phagocytic system (MPS) cells present in the liver and spleen<sup>113–115</sup>. In addition, larger particles result in increased surface absorption and opsonization by serum proteins, due to the large surface area available<sup>114, 116</sup>. The binding of the serum proteins results in increased ingestion by phagocytes which then translocate to the lymph nodes. In addition, serum protein-bound nanoparticles are more amenable to hepatobiliary excretion from the liver into the gastrointestinal tract through the biliary duct, thus helping to account for the presence of silver in the large bowel and pancreas<sup>117, 118</sup>.

The accumulation of PEG-SiAg nanoparticles within the reticuloendothelial system (RES) – liver, spleen, kidneys – may have implications on the long term survival of the animals. Studies have shown that mesoporous silica nanoparticles of comparable size and surface charge have remained in the liver for over 90 days<sup>117</sup>. There has been a sustained effort by the research community to improve the biodegradability and clearance of nanoparticle systems. Many of these methodologies are centered on trapping smaller particles in the range of 2 to 5 nm (that can be efficiently cleared) within larger biodegradable carriers (that will prolong the circulation half-life)<sup>73, 119, 120</sup>. One such example is the controlled assembly of 5 nm gold particles in 100 nm-sized biodegradable nanoclusters that are weakly held together by biodegradable triblock copolymers<sup>120</sup>. The polymers degrade slowly under physiological conditions to release the 5 nm particles that can be filtered through the kidneys and eliminated by the urine.

The PEG-SiAg nanoparticles were administered into athymic mice via subcutaneous (Figure 29) and intraperitoneal (Figure 30 and Figure 31) injections and subsequently imaged using the previously developed DE method. In each case, the DE subtraction is able to suppress the anatomic signal variation while preserving the contrast from the silver nanoparticle agent. The subcutaneous injection of the nanoparticles served to mimic a situation where the particles accumulate in a region of interest (for example, a tumor) whose visualization is hampered by overlying anatomic structures. The site of the subcutaneous injection of the PEG-SiAg nanoparticles was chosen so that the resulting bolus injection would overlap with the underlying rib cage of the animal. As seen in Figure 29, the DE image is able to



separate the signals from the bone and silver and thus, accurately portraying the boundary and volume of the bolus injection.

When injected intraperitoneally, the PEG-SiAg can be used to outline the organs in the peritoneum. The best delineation of the organs was observed after the animals had been allowed to recover from the inhaled anesthetic and move around. The motion displaced the injected bolus of the contrast material sufficiently to enable visualization of the various organ outlines. The contrast decreases in the first hour post-injection as the nanoparticles slowly enter the bloodstream and are removed from the peritoneal space.

In conclusion, the PEG-SiAg particles provided sufficient contrast to distinguish objects of interest from surrounding and overlying background structures using DE subtraction techniques. No adverse effects were recorded in any of the animals administered the silver contrast agent at the time of writing this chapter, roughly 2 months after the injections. These data are the first to demonstrate the application of a silver imaging agent as a DE contrast agent in a living system, and serves as the foundation for further improvements to the design of the prototype silver contrast material.

## CHAPTER 5

The research conducted during my Ph.D. has led to several important conclusions that I will highlight in the following chapter. While these points are discussed at length in previous sections, I will emphasize the most significant results in each of the three major subsections of my research: (i) a model to identify new candidate contrast materials, (ii) testing one such contrast material (silver) in a clinical system, and (iii) the design and development of a silver contrast agent for *in vivo* applications. In addition, the limitations of the methodologies in each of the sections will be discussed along with potential strategies to address them.

### 1. THEORETICAL MODELING

#### 1.1. CNR vs. atomic number

Materials with atomic numbers from 42 to 63 provide nearly optimal contrast in DE x-ray breast imaging. Theoretical modeling using monoenergetic x-ray simulations identified a group of materials with atomic numbers ranging from 42 to 63 (hereafter referred to as G1) that possess the nearly optimal contrast-to-noise ratio (CNR) value for DE x-ray breast imaging. When the CNR is plotted against the atomic number, a plateau can be observed for G1 (highlighted in yellow, Figure 32) where the maximum CNR between the materials does not differ by greater than 15%. Outside of this range of atomic numbers, the CNR decreases to values that can be considered insignificant for our purposes.

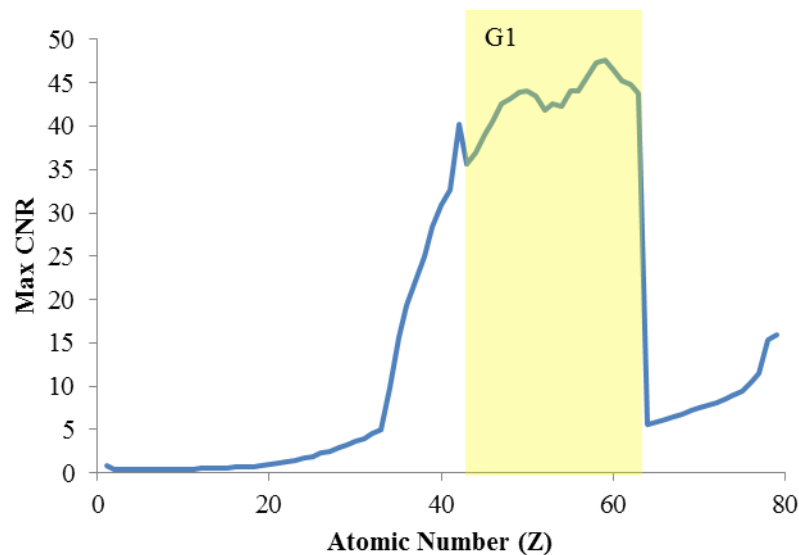


**Figure 32.** *The maximum CNR plotted against the atomic number of contrast material. Theoretical modeling is used to calculate the maximum possible CNR for every material with atomic number ranging from 1 to 80.*

G1 materials can therefore be classified as potential candidates for novel contrast agent materials in DE x-ray breast imaging. When selecting a material for further investigation, it is important to recognize two major points for consideration: (1) location of optimal HE and (2) optimal dose distribution.

Location of optimal HE: The analysis demonstrated that a LE value of 18 keV was optimal for all of the materials within G1, while the optimal HE assumed a value above the k-edge of the contrast material. The optimal HE value increases steadily with atomic number from 23 keV (atomic number: 42, k-edge: 20) to 50 keV (atomic number: 63, k-edge: 48.5). A monoenergetic x-ray source was assumed for the theoretical analysis, so the HE values roughly translate into mean energies of polyenergetic spectra in a clinical setting. Mean energies such as 35 – 49 keV require large amounts of filtration to the HE spectrum which in turn reduces the photon fluence incident upon the detector. The tube current-time product (mAs) would, therefore, need to be substantially increased to accommodate for the reduced fluence. Commercial

acquisition systems have limited tube loading and exposure times which may prevent optimal HE values for high atomic number materials from being achieved. From a practical standpoint, materials in G1 with lower atomic numbers and consequently lower optimal HE values are preferable.

Optimal dose fraction: The optimal dose fraction to the LE image for materials in G1 was shown to decrease from 0.46 (atomic number: 42) to 0.14 (atomic number: 63). Ideally, a dose fraction of 0.5 with equal doses to the LE and HE image would be used. Such a scenario would result in high-quality single-energy images that could be used separately to portray the anatomy (LE) or contrast (HE). Dose fractions that heavily bias the HE image (high atomic numbers) would result in LE images with very poor signal-to-noise ratios as a result of the low photon fluence. This would reduce the effectiveness of the DE technique as a whole, because the LE image is often used to provide anatomical landmarks for contrast uptake findings in the DE image. Noisier LE anatomic images will reduce the quality of this information and may impede the accurate diagnosis and detection of breast lesions. As with the choice of optimal HE, materials in G1 with lower atomic numbers are preferred because of a more balanced distribution of dose between the LE and HE images.

### *1.2 Limitations of monoenergetic modeling*

While a theoretical monoenergetic model was able to provide substantial insight into candidate materials for new contrast agents, it does suffer from several limitations. These limitations are evident in the previous section's discussion on the effect of the optimal HE value on the choice of contrast material. The conclusion that low atomic number materials in G1 are more favorable is based on intuition and lacks quantitative support. While the conclusion is most likely valid, a quantitative polyenergetic model to support these claims would be useful. Generalized LE and HE spectra can be simulated using the polyenergetic simulation code from Chapter 3. The results from this chapter indicate that the choice of filter material at the thicknesses used clinically has little bearing on the contrast from an imaging agent. Therefore, a generic shape for the LE and HE spectra can be assumed. From this shape, the effective attenuation coefficient of a material ( $\mu_{eff}$ ) sampled by a spectrum can be calculated as the normalized weighted sum of the product of attenuation coefficient ( $\mu$ ), spectral photon fluence ( $N$ ) and energy ( $E$ ).

$$\mu_{eff} = \frac{\sum_{E=1}^{kVp} \mu(E) \times N(E) \times E}{\sum_{E=1}^{kVp} N(E) \times E}$$

The effective attenuation coefficients of adipose, glandular, and contrast material can then be used in the calculation of weighting factor, contrast, and contrast-to-noise ratio (CNR), as demonstrated in Chapter 2. The calculation of CNR may help to support the claim that materials with lower atomic numbers in G1 are favorable due to clinically achievable optimal HE values.

## 2. TESTING SILVER IN CLINICAL SYSTEM

### 2.1 SDNR of silver vs. iodine

Silver demonstrates better contrast (higher SDNR) than iodine in a clinical image acquisition system. Silver was chosen for further investigation from the materials in G1. The low atomic number of silver means that the optimal HE value is more likely to be achieved and the optimal dose fraction will provide a good quality LE anatomic image. In addition, the prevalent use of Ag filters in CEDE imaging means that the LE spectrum can be filtered to block energies above the k-edge of Ag. This is important because DE contrast is only observed when the LE and HE values are on opposite sides of the k-edge of the imaging agent. The transition from scientific validation to bench-top testing of a silver imaging agent is facilitated by the large amounts of literature available on the synthesis of silver nanoparticles. Nano-silver represents the largest and fastest growing category of nanotechnology-based consumer products, owing to their excellent antimicrobial properties<sup>76</sup>.

A simulation algorithm was developed in order to identify the optimal imaging conditions for silver and iodine imaging agents on a clinical acquisition system. Once these conditions were identified, the two materials were compared objectively to determine which contrast agent provided higher contrast. The system chosen to be simulated was the prototype Hologic Dimensions CEDE x-ray breast tomosynthesis unit, located in the breast imaging section at the Perlman Center for Advanced Medicine. The algorithm searched through 26,460 combinations of kV values, filter materials, and dose fractions to identify the

optimal, clinically-feasible imaging parameters. Clinical feasibility was assessed by limiting the mean glandular dose to the breast to values that Hologic currently implements for its DE clinical trials. The spectral combinations were therefore required to deliver this dose to the breast as well as a minimum threshold signal intensity at the detector while under the maximum allowable tube current-time product of the x-ray tube. The results of the simulation algorithm were tested by measuring the weighting factor and signal difference-to-noise ratio (*SDNR*) experimentally for a select group of spectral pairs. The two sets of data showed excellent correlation, which led us to believe that the simulation algorithm was successful in predicting the signal response of the imaging system. Any optimal points that were identified through the algorithm can be confidently assumed to be optimal for imaging on the system.

The optimal imaging conditions identified by the simulation algorithm were then tested using a custom-built physical phantom. The phantom measures 3 cm in height and has a 4 mm bore drilled along its longitudinal direction. The bore allows for a plastic tube containing the contrast agent to be imaged against varying glandular percentages. 16 mg/mL of silver or iodine contrast agent was then imaged at the optimal silver or iodine imaging conditions. The measurements were repeated for various LE filters (aluminum – Al, rhodium – Rh, silver – Ag). The results (shown in Figure 24) demonstrate several important points:

- **The *SDNR* does not vary with filter material.** The *SDNR* for either contrast material varies by less than 4% across the various LE filter materials. This can be explained by the fact that the thickness of each material is not large enough to impart a unique shape to the spectra. The filters primarily serve to remove low energy x-ray photons below 10-15 keV that would otherwise be completely attenuated by the breast and serve no use to form the image on the detector. The optimal LE kV was 26 kV regardless of contrast or filter material. While the higher atomic number filter materials such as rhodium and silver are able to substantially attenuate the spectra above the k-edge of these materials (23.2 and 25.5 for rhodium and silver, respectively), these k-edges are too close to the LE peak voltage to substantially alter the shape of the spectrum. Therefore, there is very little, if any, difference between the choices of filter material when the LE kV is set to a value of 26.

- At their respective optimal imaging conditions, silver performs better than iodine.** The *SDNR* for silver is on average 43 % higher than that of iodine. The improved *SDNR* for Ag can be attributed to the lower k-edge. A lower k-edge means that there is sufficient space between the k-edge and the maximum possible voltage (50 kV) for the HE spectrum. Such an arrangement results in a high percentage of the spectrum being placed above the k-edge and thus contributing to the DE *SDNR*. By contrast, the relatively high k-edge of iodine means that a substantial portion of the HE spectrum is below the k-edge of iodine, and therefore does not contribute to the DE *SDNR*. For example, when using a 49 kV HE spectrum with copper filtration, 99% of the spectrum (by number of photons) is above the k-edge of silver while only 78% is above the k-edge of iodine. The tube voltage limitation in clinical systems results in an improved *SDNR* for lower atomic number materials such as silver.
- When imaged at the optimal imaging conditions for iodine, silver still performs better.** This would suggest that minimal machine modifications, if any, are needed to translate a bio-stable silver imaging agent into the clinic. The improvement in *SDNR* observed with silver could still be obtained if the protocols currently in place for an iodinated contrast agent are followed.

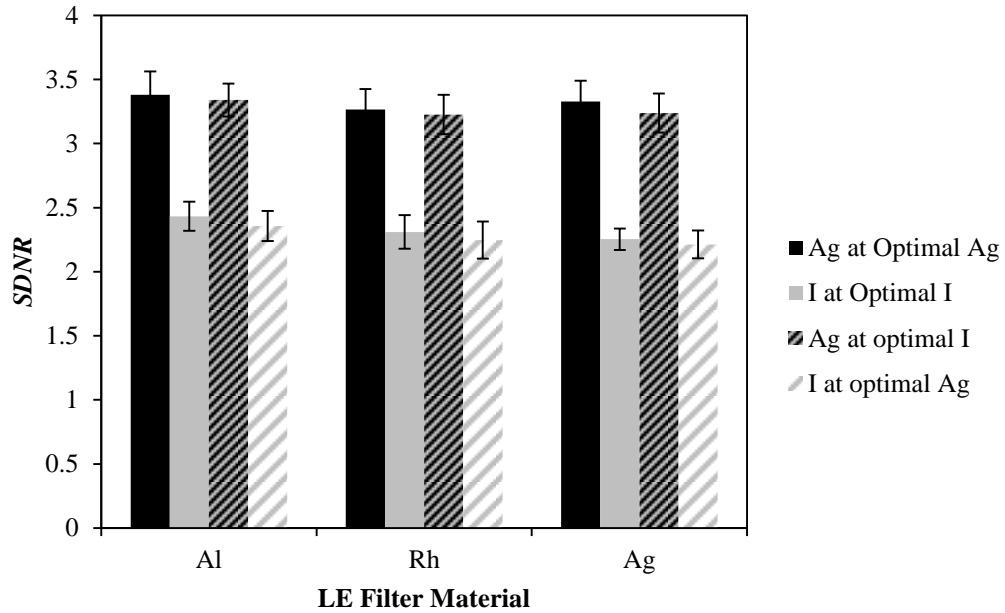


**Figure 33.** Comparison of  $SDNR$  between Ag and I for the optimal imaging parameters at each LE filter material. Ag performs better than Iodine at their respective optimal imaging conditions, regardless of the filter material. In addition, I imaged at the optimal conditions for I performs worse than Ag at those same conditions.

## 2.2 Limitations of the current model

The simulation algorithm, in its current form, is able to correctly predict the trends of the signal intensities. If spectral combination 1 has a higher  $SDNR$  than spectral combination 2, this will be properly reflected in the simulation results. However, the actual  $SDNR$  values are not accurate in the simulation. Currently, the simulated values are four times that of the experimental values. The purpose of the simulation algorithm was to identify the optimal imaging conditions for contrast materials, and not to predict the exact signal intensity of the system. In this application, the factor of four difference between the experimental and simulated values has no consequence on the results. However, for future analysis, a more accurate simulation of the Hologic signal intensity and noise may be useful. The simulation could also be used to help guide the design of imaging systems by identifying filter materials that maximize the  $SDNR$ .



for a particular contrast material. The algorithm could search through potential filter material candidates that are identified based on their availability and ease of manufacturing. The algorithm could then predict the tube output for the particular target-filter material based on empirical data that has been collected for those materials currently present in the Hologic DE acquisition system. The algorithm would then be able to identify an optimal filter thickness that maximizes the *SDNR* for silver.

Accurate representation of the noise in DE x-ray breast imaging can lead to several avenues of potential research. There are numerous ongoing efforts to denoise DE images in DE computed tomography<sup>23, 39, 121</sup>, but very few attempts to reduce the noise in DE x-ray breast imaging. A better understanding of the nature of the noise is required for this task. A simulation algorithm that could accurately predict the noise for various weighting factors and DE subtraction techniques could be used to test the effectiveness of new denoising algorithms. Johns *et al.*<sup>7</sup> used an averaging algorithm to reduce the variance in the HE image by a factor of 4 before the subtraction technique was applied. They found that this increased the detection of microcalcifications in a suppressed background, despite an overall reduction in the *SDNR*. Optimizations in noise reduction, similar to this, can be made once the noise in the Hologic DE imaging system has been accurately quantified. To this end, we can draw upon the works of Marshall *et al.*<sup>103, 122</sup> who characterized the noise in several mammography systems including the Hologic Selenia. In their analysis, the standard deviation ( $\sigma$ ) in the image was broken down into three components: electronic ( $\sigma_e$ ), quantum ( $\sigma_q$ ) and structured ( $\sigma_s$ ) noise.

$$\sigma = \sqrt{\sigma_e^2 + \sigma_q^2 + \sigma_s^2}$$

The electronic noise is independent of x-ray exposure and can be estimated by a constant,  $e$ .

$$\sigma_e = e$$

The quantum noise is assumed to be purely Poisson, and scales by a factor  $q$  with the square root of the air kerma ( $K$ ).

$$\sigma_q = q \times \sqrt{K}$$

The structured noise is amplified by the x-ray signal used, and can be expressed in terms of  $K$ , and a constant  $s$ .

$$\sigma_s = s \times K$$

Using this method, the standard deviation in either low- or high-energy image can be estimated as:

$$\sigma = \sqrt{e + q^2 \times K + s^2 \times K^2}$$

The constants  $e$ ,  $q$ , and  $s$  must be determined empirically for the Hologic DE acquisition system by measuring the standard deviation in regions of interest in several low and high-energy images. For a first approximation, the constants can be assumed to be independent of the incoming energy of the x-ray spectrum. However, the energy-dependence of the detector response may play a significant role, and should be tested. The standard deviation in the DE image can then be formulated using a combination of the low- and high-energy standard deviations and weighting factors. In addition, terms relating to the covariance between pixel elements from the low- and high-energy images can contribute to the standard deviation of the DE image. Once the DE standard deviation is accurately formulated and validated for the Hologic DE acquisition system, the effect of various de-noising algorithms and techniques can be tested for efficacy.

### 3. PROTOTYPE SILVER CONTRAST AGENT

#### 3.1 Testing of silica-silver nanoparticles in mice

The synthesized silica-silver nanoparticles (PEG-SiAg) consisted of a solid, spherical silver core with an average diameter of  $39 \pm 6$  nm and a silica shell thickness of  $63 \pm 7$  nm. The total diameter of the nanoparticles is  $102 \pm 9$  nm. The hydrodynamic diameter of the particles was measured through dynamic light scattering measurements to be 115 nm. The discrepancy between the diameter measured by DLS and TEM is a result of the PEG surface layer. The PEG ligand is electron-transparent and therefore does not appear in the transmission electron micrographs that are used to determine the physical diameter. However, the surface ligand does influence the interaction of the particle with the surrounding media and will therefore have an effect on the hydrodynamic diameter. The nanoparticles have a vascular half-life of 13

minutes, and were taken up by macrophage-rich organs, such as the liver, spleen and lymph nodes. In addition, noticeable amounts of silver were detected in the pancreas and large intestine, indicating that some of the particles may have been excreted by the liver into the gastrointestinal tract.

An example of the effectiveness of the synthesized PEG-SiAg particles as a DE contrast agent is illustrated in Figure 34. An injection of the nanoparticles was implanted subcutaneously above the rib cage of athymic, female mice. The animals were then imaged using a 49 kV rhodium spectrum with rhodium filtration and a 26 kV molybdenum spectrum with molybdenum filtration. The low- and high-energy images were logarithmically subtracted with a weighting factor to eliminate the influence of soft tissue and bone. As observed in the DE image (Figure 34c), the anatomical contrast has almost entirely been removed. The signal arising from the subcutaneous silver agent is, however, preserved. When considering the overlying bones of the rib cage of the animal as the background, the *SDNR* of the bolus silver injection increased from 1.14 and 0.87, in the high and low-energy image respectively, to 8.75 in the DE image. This corresponds to an increase in *SDNR* of 660 and 910%, respectively. The DE image is able to separate the signals from the bone and silver and thus, accurately portray the boundary and volume of the injection.

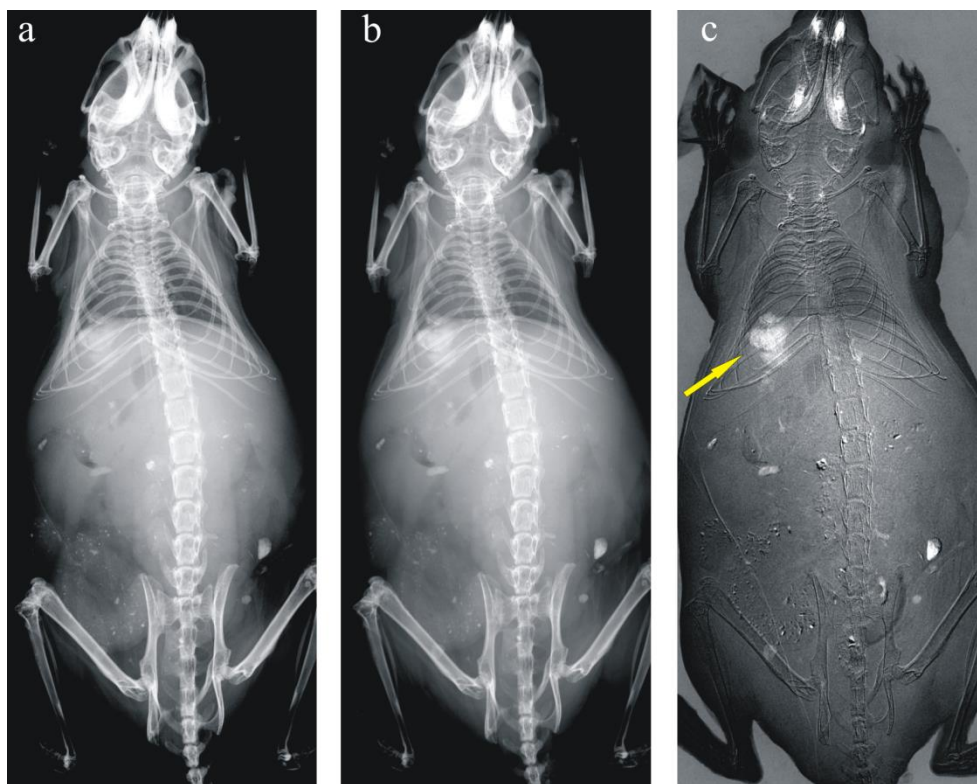


**Figure 34.** *LE (a), HE (b), and DE(c) images of the mouse after administration of PEG-SiAg via subcutaneous injection (yellow arrow).*

### 3.2 Proposed redesigns of prototype silver agent

One of the major obstacles in developing a biocompatible silver CEDE imaging agent is the toxicity of silver nanoparticles in biological systems<sup>76, 105, 109, 123, 124</sup>. While the cause for this toxicity is not fully understood, it is hypothesized that the generation of free  $\text{Ag}^+$  ions from the nanoparticle plays a major role. The oxidation of silver on the nanoparticle surface results in free ions that disrupt biochemical pathways and generate free radicals that contribute to oxidative stress. We, thus, devised a nanostructure composed of a silver core encapsulated within a silica shell to reduce the interaction of the silver nanoparticle surface with the surrounding media. The results demonstrated that the inclusion of the silica substantially reduced the toxicity of silver nanoparticles. Previous generations of the nanoparticles administered at the doses used in the imaging studies in Chapter 4 resulted in severe distress of the animals,

6 hours after the administration of the particles. The animals injected with the current formulation are still alive at the time of writing this document, roughly 2 months after the injection of the nanoparticles. However, the porous nature of silica may not completely prevent the interaction of the silver core with the environment. Long term survival studies will need to be performed to determine definitively if the silica shell is adequate in preventing the toxic effects of the silver cations.

Based on these initial results, an alternative strategy has been devised for future investigation, whereby the silver core is encapsulated within a gold (instead of silica) shell. Gold atoms are more tightly packed compared to silica, as evidenced by the smaller lattice constant (4.08 and 5.43, for gold and silica respectively)<sup>43</sup>. The close arrangement of the gold atoms will help prevent the interaction of the encapsulated silver core with the surrounding media, and therefore reduce toxicity. Li *et al.*<sup>125</sup> demonstrated that bimetallic nanoparticles consisting of mixtures of silver and gold had significantly lower toxicity compare to silver nanoparticles. The bimetallic nanoparticles were only slightly more toxic than gold nanoparticles – generally considered to be biologically inert. It is important to remember that these results were obtained with a bimetallic structure, meaning that a certain proportion of the silver atoms were located at the surface and free to interact with the surrounding media. We therefore hypothesize that by completely encapsulating the silver core within a gold shell, the toxicity of the entire nanostructure will be comparable to that of gold nanoparticles. Surface stabilized gold nanoparticles have been employed extensively in mouse models and have been shown to be biologically inert at the concentrations required for imaging<sup>61, 71, 73, 126–128</sup>. The near-zero lattice mismatch between gold and silver (Lattice constants of 4.08 for gold vs. 4.09 for silver<sup>43</sup>) suggests that reduced gold will have a high affinity for a silver surface and that a silver-gold core-shell nanostructure is experimentally feasible.

The silver cores could be encapsulated with a gold shell using a slightly modified method from that described by Cao *et al.*<sup>129</sup>. In their manuscript, Cao deposited a single layer of gold atoms (roughly 0.4 nm thick) onto the surface of 12 nm silver nanoparticles. Our application requires a thicker gold shell in order to minimize any possible interaction between the encapsulated silver surface and the surrounding biological media. The protocol consists of the simultaneous addition of gold (III) chloride and sodium borohydride into a solution of silver nanoparticles and sodium citrate at 0°C. The concentration of the gold-forming

reagents must be maintained at roughly 2 mM to enhance the reduction of gold on the silver surface and prevent the formation of separate gold cluster nucleation sites. The thickness of the gold shell will need to be optimized so as to minimize the toxicity of the entire nanostructure. As an example, in order to deposit a 5 nm thick gold shell onto the surface of a 39 nm silver nanoparticle, the following protocol should be used. 1 nmole of silver nanoparticles is suspended in 400 mL of 0.3 mM sodium citrate aqueous solution. To this solution, a total of 317 mg of  $\text{HAuCl}_4(\text{H}_2\text{O})_3$  and 1.47 g of  $\text{NaBH}_3$  is added drop-wise. The reaction vessel is maintained at 0°C by immersing in ice.

Finally, the silver-gold core-shell nanoparticles can be surface stabilized using a heterobifunctional polyethylene glycol ligand. The ligand would require a proximal thiol group for direct attachment to the gold surface and a distal non-reactive methyl group. The methyl group can be replaced with other moieties to allow for the attachment of targeting ligands. An illustration of the final design of the nanoparticle is shown in Figure 35.

The effectiveness of the gold shell can be tested experimentally by measuring the leeching of silver cations using inductively-couple plasma optical emission spectroscopy (ICP-OES). A 20 mL sample of the silver-gold nanoparticles should be dissolved in de-ionized water and placed inside of a 10k MWCO dialysis bag. The bag is placed inside of a beaker filled with 500 mL deionized water. 1 mL samples of the water should be obtained at regular intervals ( 0.5, 1, 2, 4, 8 and 24 hours) after the introduction of the dialysis bag. The sample can then directly used to measure the content of silver ions using ICP-OES. Various testing solutions can also be placed in the dialysis bag: deionized water (negative control), silver nitrate solution (positive control), PVP-coated silver nanoparticles, and Si-encapsulated silver nanoparticles. The de-ionized water will serve as the negative control to correct for any silver present in the water, if any. The silver nitrate solution with the same total amount of silver as the silver-gold nanoparticle solution will set an upper limit for the diffusion of silver anions across the dialysis membrane. The PVP- and Si-coated nanoparticles will help to compare the effectiveness of the gold shell to that of other formulations.

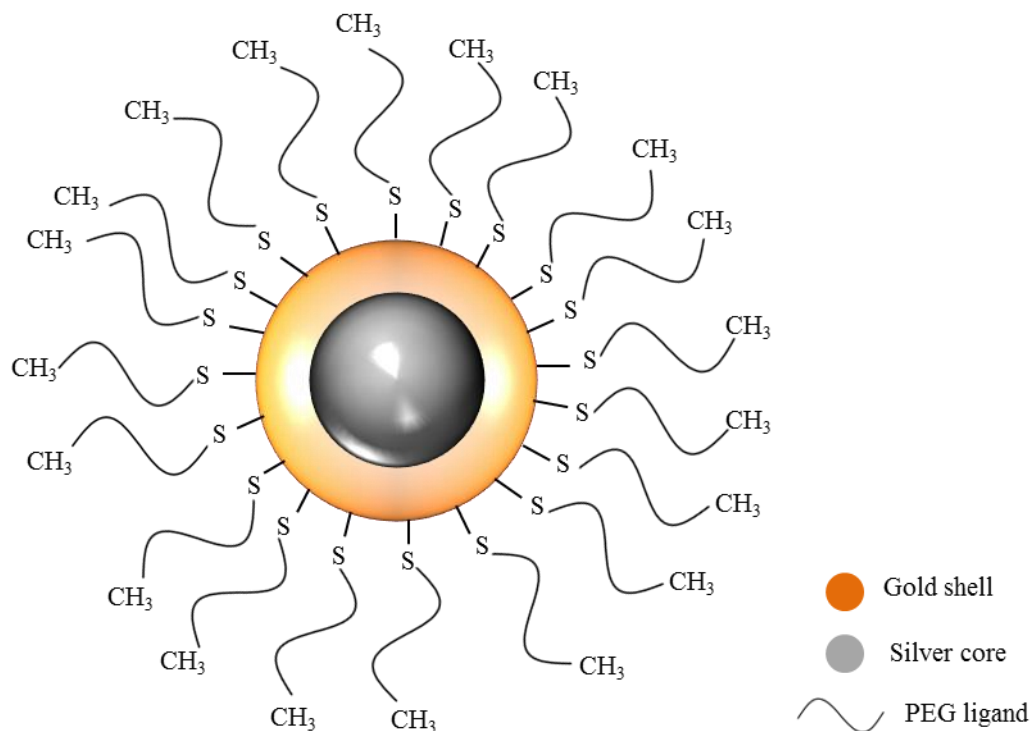


**Figure 35.** Design of the silver-gold core shell nanoparticle. The nanoparticle is surface stabilized using a heterobifunctional polyethylene glycol (PEG) ligand. The proximal thiol group attaches directly to the gold surface, while the distal unreactive methyl group is to prevent the non-specific attachment of biological compounds.

## APPENDIX

Prior to the development of the silver nanoparticle design outlined in Chapter 4, several iterations of nanoparticles were synthesized and tested. This chapter aims to outline the various generations of nanoparticle contrast agents; the major discoveries and lessons learned throughout the development process.

### Gold Nanoparticles

Initially, gold (instead of silver) nanoparticles were designed as contrast agents for x-ray breast imaging. These nanoparticles were intended for use in contrast-enhanced breast imaging procedures using temporal subtraction. In this case, a single-energy image is obtained before and after the administration of the contrast agent. The images are then subtracted to yield either a contrast- or soft-tissue-only image. Gold was chosen for this purpose due to its high atomic number and its abundant presence in the scientific literature. Gold has roughly three times greater contrast per unit weight compared to iodine at typical mammographic energies (15 – 40 keV). Gold nanoparticles (AuNP) have also been the target for considerable scientific attention due to their non-toxic, biological compatibility and optical properties<sup>130–140</sup>. As an example, Tkachenko has used a AuNP platform for a nuclear targeting mechanism<sup>134</sup>. The 20 nm AuNPs were conjugated to various peptides that serve to induce receptor-mediated endocytosis (RME), interact with the nuclear pore complex and enter the nucleus. The peptide-nanoparticle complexes were then incubated with HepG2 cells and imaged using video-enhanced difference interference contrast (DIC) microscopy.

### Gold Nanoparticles – Synthesis

The AuNP were synthesized using a modified Turkevich method described by Grabar *et al.*<sup>141</sup>. The method involves the reduction of a boiling solution of gold chlorate by citrate anions, which serve as both the reducing agent and surfactant. The citrate anions form a protective barrier around the AuNPs and prevent separate particles from fusing together. The final size and distribution of the particles obtained is dependent on a multitude of factors including the pH and temperature distribution of the boiling gold solution, but most importantly on the molar ratio between the gold chlorate and citrate solution. Described



here are the steps used in the synthesis of AuNP with an expected diameter in the range of 13 nm using a 4:1 ratio between the gold and citrate.

All glassware used in the synthesis was first treated with aqua regia (3 parts nitric acid, 1 part hydrochloric acid), rinsed with deionized (DI) water ( $\text{H}_2\text{O}$ ), and then oven-dried. Briefly, 321.6 mg of gold (III) chloride trihydrate ( $\text{HAuCl}_4 \cdot 3\text{H}_2\text{O}$ ) was dissolved with 450 mL of DI- $\text{H}_2\text{O}$  and placed in a 1L round-bottom flask with a Teflon-coated magnetic stirring rod. The flask was fitted with a condenser, placed atop a heating mantle and magnetic stirrer, and the gold solution was brought to a boil. Next, 0.93 g of sodium citrate dihydrate ( $\text{C}_6\text{H}_5\text{Na}_3\text{O}_7 \cdot 2\text{H}_2\text{O}$ ) was dissolved in 45 mL of DI- $\text{H}_2\text{O}$  and added to the boiling gold solution. Upon addition of the sodium citrate, the solution rapidly changed color from a pale yellow to a deep burgundy. Heating was continued for an additional 10 minutes after which the heating mantle was removed, and the solution was stirred for a further 15 minutes. The resulting colloidal AuNP solution was allowed to cool overnight and then filtered through a 0.2  $\mu\text{m}$  membrane filter.

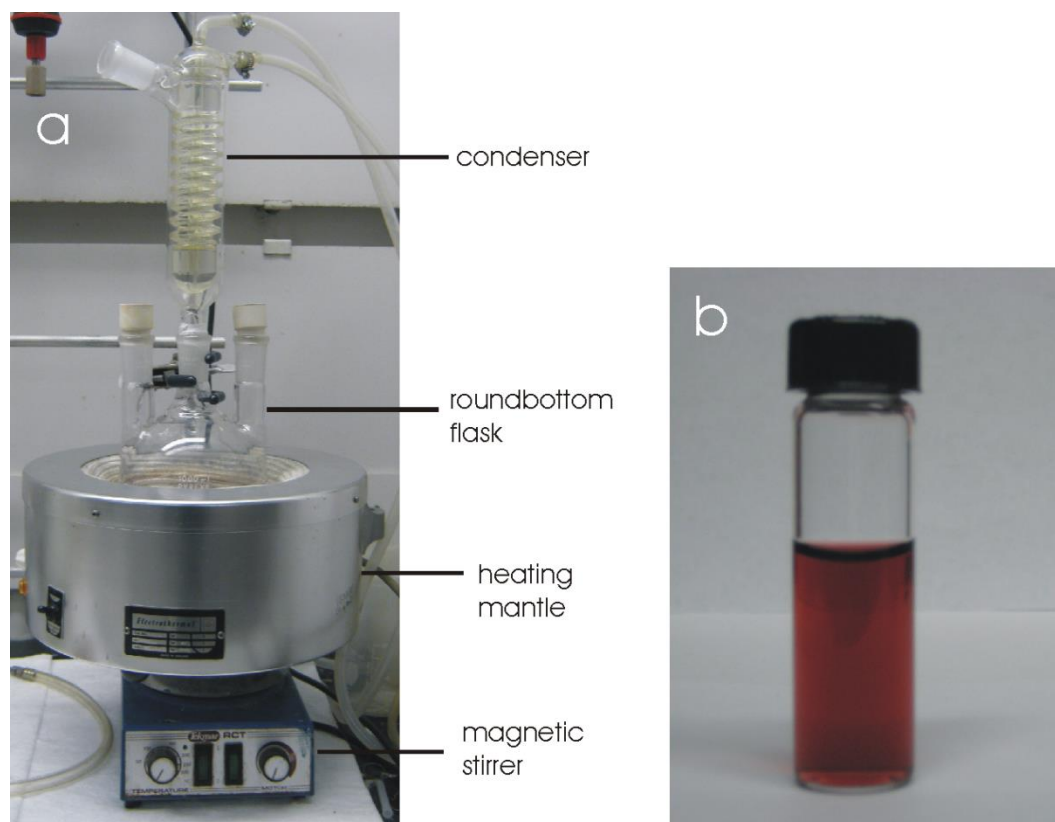


**Figure A1**(a) *Synthesis setup: 1L roundbottom flask fitted with a condenser is placed atop a heating mantle and magnetic stirrer. (b) The citrate-stabilized gold nanoparticles, displaying a characteristic deep-burgundy color.*

The citrate-stabilized gold nanoparticles (cAuNP) were then further stabilized using polyethylene glycol (PEG) chains, as cAuNP are unsuitable for use *in vivo*. The cAuNP are also stabilized through mutual electrostatic repulsion between neighboring negatively-charged nanoparticles. This repulsion can be shielded by ions present in a salt-like, or ionic, solution (e.g. blood plasma), which would result in the aggregation of the cAuNP.

The cAuNP were thus conjugated with polyethylene glycol (PEG) chains in order to obtain surface-stabilized AuNP (ssAuNP) that were stable in blood serum, and exhibited enhanced stealth properties *in vivo* [5-7]. The PEG chain chosen for the conjugation has an average molecular weight of 5000 Da and possesses an unreactive methyl group on one end, and a thiol (-SH) group for direct

attachment to the gold surface on the other (Figure 2). The conjugation scheme was based on a similar procedure by Bergen et al. [8], which assumed a 4 PEG/nm<sup>2</sup> surface coverage.

Described here is an example of a typical functionalization procedure. 30 mL of cAuNP was mixed with 6.7 mL of a 272  $\mu$ M PEG solution in an Erlenmeyer flask, and stirred at room temperature for 1 hour. The solution was then centrifuged twice at 11,400 xg for 45 minutes, after which the ssAuNP pellet was resuspended in 2 mL of DI-H<sub>2</sub>O. The ssAuNP were concentrated further by resuspending the centrifugation pellet in successively smaller volumes.

#### Gold Nanoparticles – Characterization – Stability in Ionic Solutions

In order to demonstrate the improved stability that is a result of the surface stabilization of the AuNP with PEG, 800  $\mu$ L each of cAuNP and ssAuNP were mixed with 400  $\mu$ L of phosphate-buffered saline (PBS) – a common buffer solution whose osmolarity and ion concentration match those of the human body. As shown in Figure A2, addition of PBS to the cAuNP resulted in an aggregation of the particles and a change in color from red to purple-blue. The ssAuNP, by contrast, showed no observable change in color or stability after the PBS had been added.

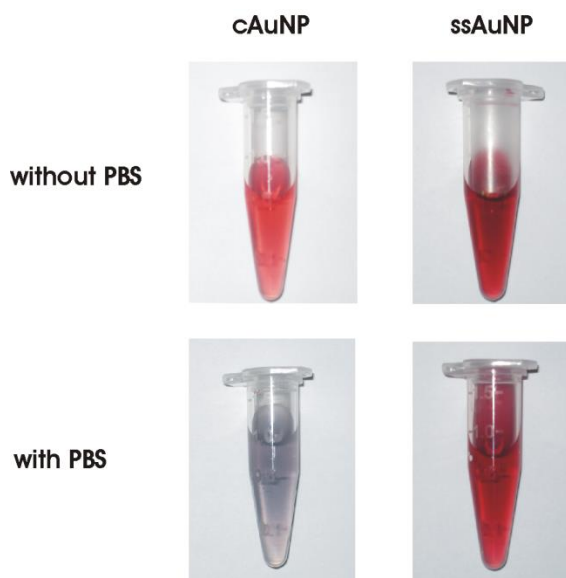


**Figure A2.** *Effect of PBS on cAuNP and ssAuNP.*

### Gold Nanoparticles – Characterization – Optical Absorbance

The characteristic deep-burgundy color of the gold nanoparticle is due to its optical absorbance properties in the visible light range. The particles exhibit a characteristic absorbance peak that is typical of most colloidal metal nanoparticle solutions. This peak is a result of the coherent oscillation of free conduction electrons in nano-sized metal structures in the presence of an electromagnetic field; a phenomenon commonly referred to as surface plasmon resonance (SPR). The peak wavelength of the SPR is determined by the size of the nanoparticles, the presence of a surface agent, as well as the pH of the surrounding solution.

Figure A3 shows the SPR of the cAuNP, with a peak wavelength of 522 nm. The concentration of the nanoparticles was determined using extinction coefficients present in the literature, and was found to be 20.7 nM. Figure A4 shows that the normalized SPR of the ssAuNP is shifted to the red by 2 nm compared to that of the cAuNP. This shift in the SPR helps confirm the presence of the PEG layer on the surface of the ssAuNP.

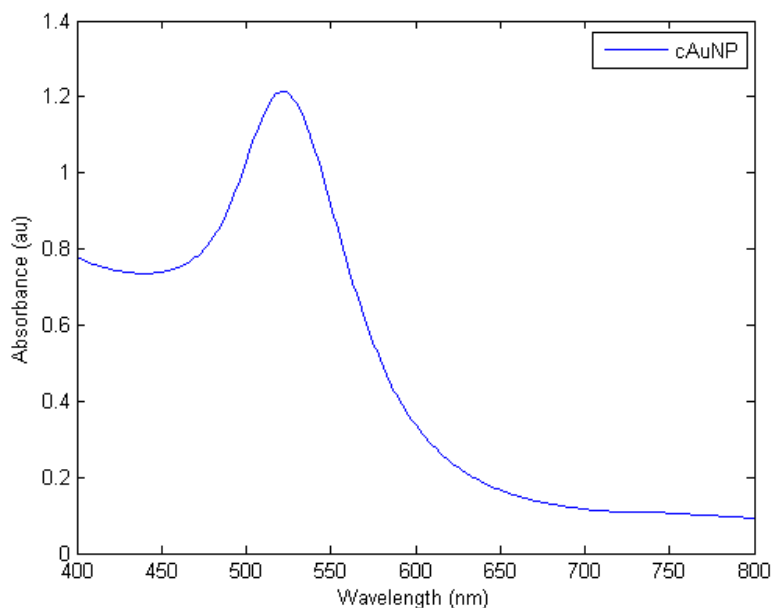


**Figure A3.** SPR of cAuNP in the UV/Vis range.

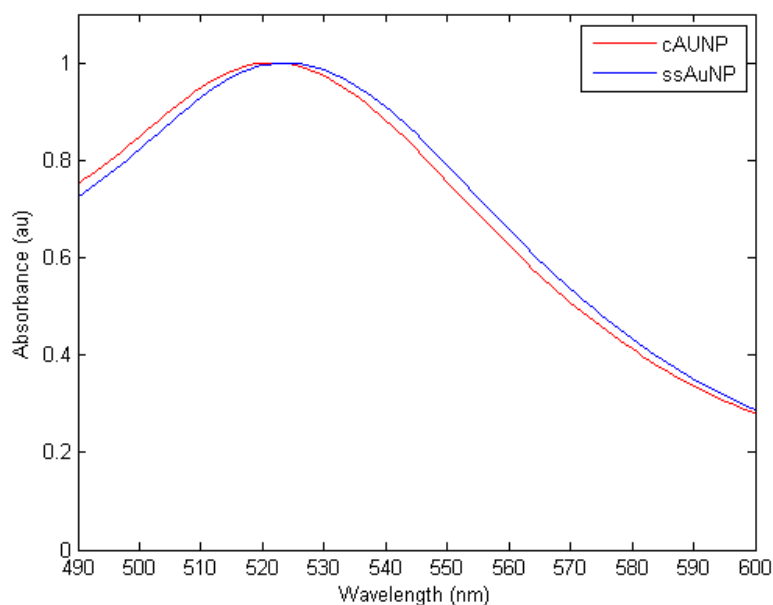


**Figure A4.** Red-Shift in the normalized SPR of the ssAuNP compared to cAuNP. This finding helps confirm the presence of the PEG layer on the surface of the ssAuNP.

#### Gold Nanoparticles – Characterization – Physical Diameter

The diameter of the AuNP was determined through TEM. A drop of the AuNP (cAuNP and ssAuNP) solution was placed on a carbon-coated copper grid and allowed to dry for 6 hours prior to imaging. The grid was then imaged using a high-resolution transmission electron microscope, and the images obtained are shown in Figure A5. The size of the AuNP was determined by individually measuring the diameter of 50 imaged nanoparticles, and averaging the result. The average diameter of the AuNP was found to be  $21 \pm 4.2$  nm.

The ssAuNP (Figure) appear to be further spaced apart than the cAuNP (Figure) due to the presence of the PEG layer on the surface of the nanoparticles. The PEG chains provide a physical barrier between the nanoparticles, and thus prevent them from coalescing or clumping together.

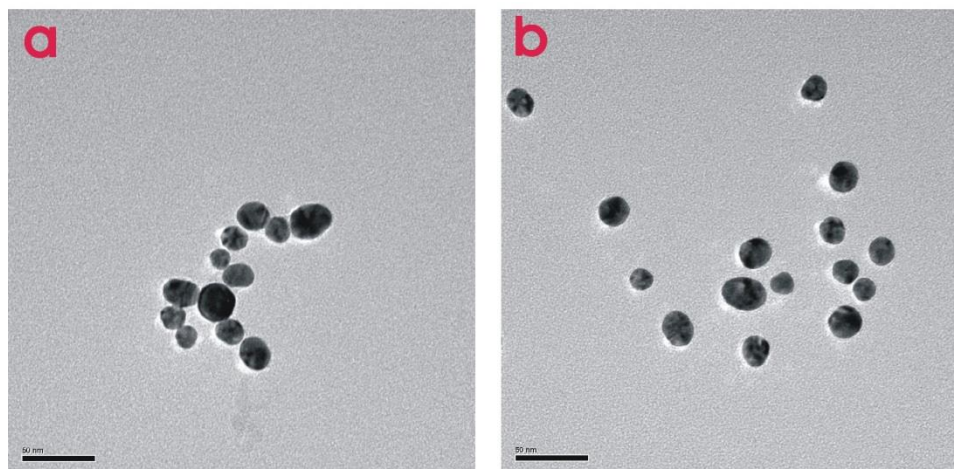


**Figure A5.** TEM images of (a) cAuNP and (b) ssAuNP. The scale bar in the images corresponds to 50 nm.

Gold crystals are structured as a face-centered lattice, and the atoms are arranged in regular arrays that are spaced an equal distance apart<sup>43</sup>. This is illustrated in Figure A6 that shows a magnified view of a AuNP. A line-plot of the pixel intensities through the crystalline pattern shows that the peaks are spaced roughly 2 Angstroms (0.2 nm) from each other. These findings agreed with findings presented in the literature regarding the growth and structure of gold crystals<sup>43</sup>.

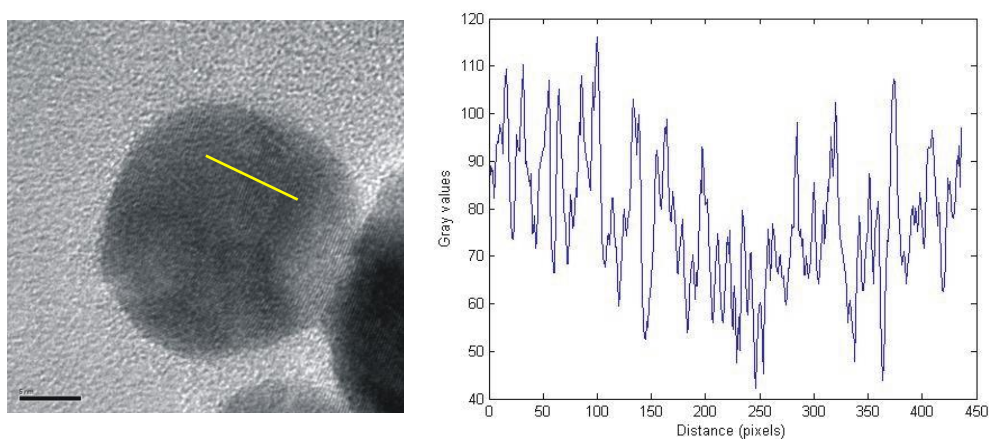


**Figure A6.** The crystal structure of the AuNP (left). A line plot of the pixels marked in yellow was obtained (right). The distance between the peaks on the graph averaged to 8 pixels which corresponded to a distance of 0.25 nm.

### Gold Nanoparticles – Characterization – X-ray spectroscopy

The chemical composition of the nanoparticles was determined using energy-dispersive x-ray spectroscopy, and the energy of the photons emitted from the sample was collected and measured. The spectrum of energies obtained from the citrate-capped AuNP sample is shown in Figure A7. The peaks show the presence of carbon, copper and gold in the sample. The carbon and copper are attributed to the grid on which the particle solution was dried, and the gold is from the nanoparticles. The results from the TEM clearly showed that our solution was indeed colloidal gold nanoparticles with an average diameter of 21 nm.

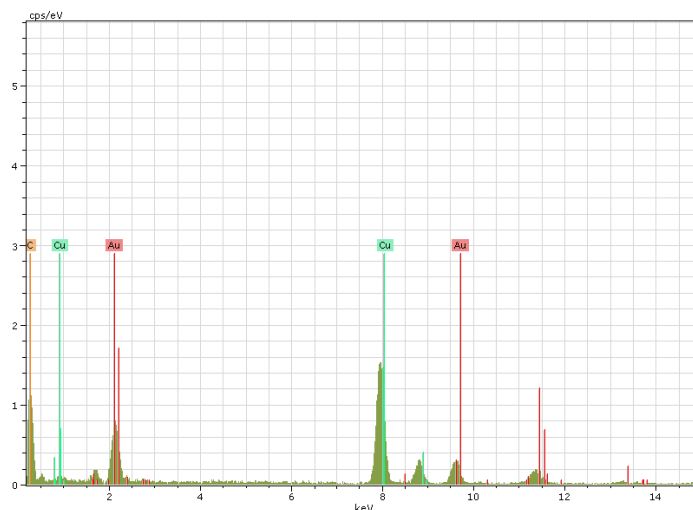


**Figure A7.** *The energies of photons emitted from the AuNP sample\*

### Silver Nanoparticles

With the emergence of contrast-enhanced dual-energy x-ray imaging in the mammographic research community, the focus of my research shifted towards the development of contrast materials for this modality. The installation of a prototype Hologic dual-energy 2D and 3D acquisition system at the Perlman Center for Advanced Medicine provided me the opportunity to test the new contrast materials on a clinical system. Contrast-enhanced dual-energy (DE) x-ray imaging provides a technique to increase the contrast of radiographic imaging agents by suppressing the variation in signal between various tissue types.

In the breast, this involves the suppression of the signal variation between admixtures of glandular and adipose tissue. By reducing the effect of this “anatomical noise”, it is then possible to more accurately segment and quantify the signal from the contrast agent. Dual-energy imaging utilizes two distinct energy windows (low- and high-) to quantify the variation in attenuation with energy. To achieve a suitable contrast between imaging agent and tissue, it is therefore necessary that their respective attenuation profiles do not follow the same general trend from low- to high- energy. This can be done by using a contrast material whose k-edge lies between the two energy windows. The discrete jump in attenuation due to the photoelectric effect of the extra k-shell electrons means that the contrast material exhibits a markedly different attenuation profile to the surrounding tissue.

Currently, the majority of research that is performed in dual-energy x-ray imaging involves iodinated contrast agents. Silver (Ag) represents an attractive alternative due to the location of its k-edge (25.5 keV) within the range of clinically-used mammographic energies. Silver filtration is also common in the clinical setting, which could provide additional benefit with a silver imaging agent. This benefit arises because the low-spectrum can be filtered to remove the portion of the spectrum that resides above the k-edge of the contrast material. This results in a spectral pair that almost perfectly brackets the k-edge of silver.

#### Silver Nanoparticles – 1<sup>st</sup> Generation

The first generation of silver nanoparticles (AgNP) were synthesized using the Brust method<sup>142</sup> in water. This is preferred over the Turkevich method as it provided a more reliable size distribution of particles from batch to batch. Figure A8 shows a transmission electron micrograph (TEM) of the synthesized particles. Analysis of the size distribution yielded a mean diameter of  $4 \pm 2$  nm. Initial analysis showed two populations of nanoparticles present which accounts for the high standard deviation in mean diameter. The AgNP were surface stabilized using polyethylene glycol thiol (PEG,  $M_w = 5000$ ) to improve solubility in cell media and phosphate buffered solutions. A molar ratio of 1.5:1 was used between the PEG stabilizing ligand and silver.



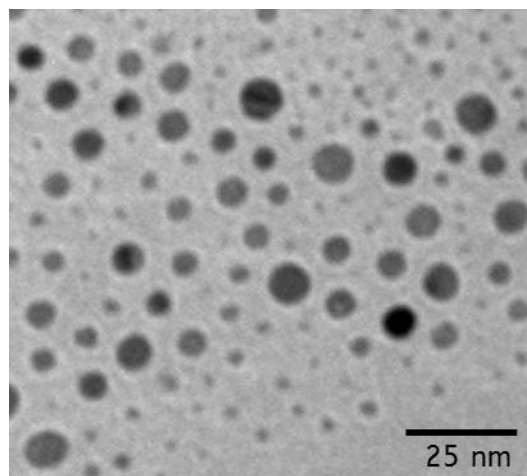


**Figure A8.** TEM of the colloidal silver nanoparticles synthesized using the Brust method in water. The particles have been stabilized using a polyethylene glycol surface chain.

The hydrodynamic diameter of the particles was measured using a Zetasizer dynamic light scattering instrument and was found to be  $20 \pm 5$  nm (see Figure A9). The difference between physical and hydrodynamic diameter corresponds to the length of the PEG ligand on the surface of the particles.

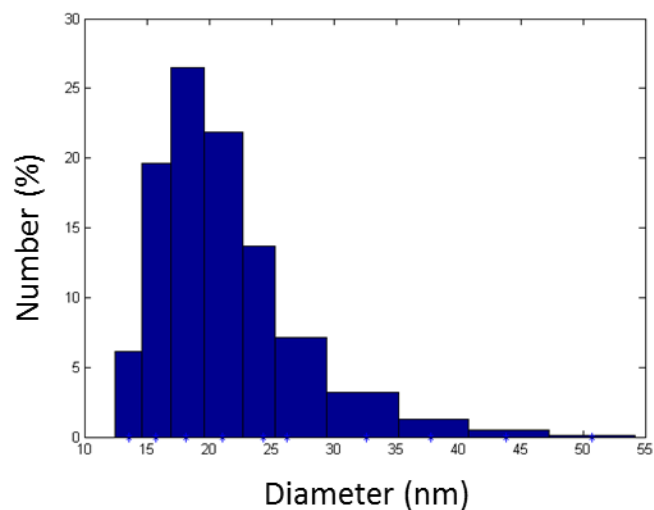


**Figure A9.** Dynamic light scattering measurements showing the hydrodynamic diameter of the synthesized particles

The cellular toxicity of the stabilized AgNP was measured in T6-17 fibroblast cells using the MTT assay. Figure A10 shows the relationship between concentration of Ag in AgNP and percent cell viability after 24 hour incubation. Compared to a sham treated control, total cell viability of 50% was maintained at an Ag concentration of 10 mM (roughly 1 mg Ag/mL). These results show marked improvement over cell viability studies using AgNP in the literature<sup>105, 109</sup> and have encouraged us to begin analysis of the particles in living systems.

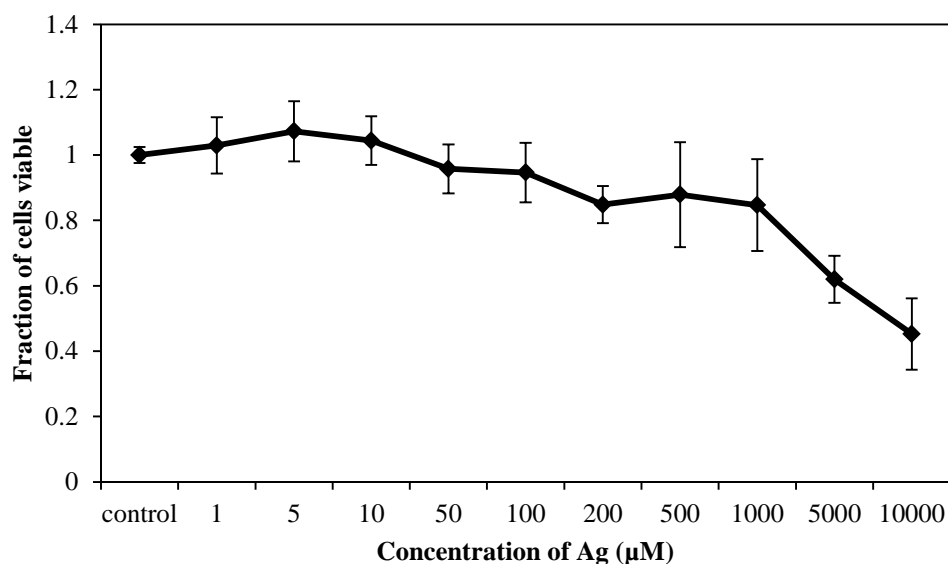


**Figure A10.** Cellular toxicity of AgNP in T6-17 cells after 24-hour incubation.

AgNP were then injected into immunocompromised mice at an initial dose of 0.24 mg Ag. Blood Ag content was measured using blood draws for time points up to 24 hours post-injection (see Figure A11). The data suggests that the plasma half-life of the particles is roughly 45 minutes.

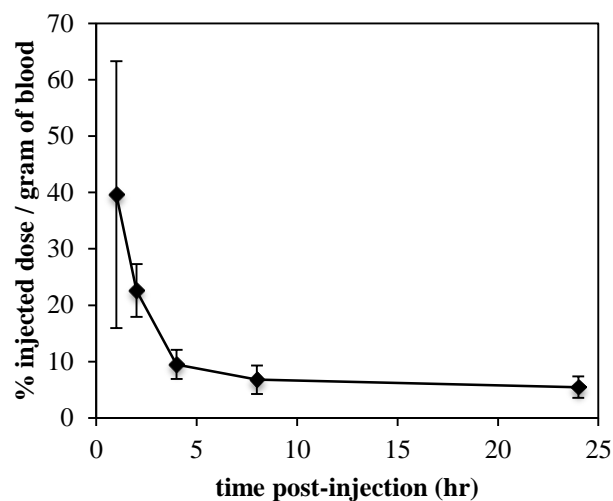


**Figure A11.** Blood Ag levels in immunocompromised mice up to 24 hours post-injection

The animals were then sacrificed at 24 hours post-injection, and their organs harvested and digested using nitric acid. Figure A12 shows the Ag content of the organs collected. The majority of the particles were found to be trapped in the spleen.

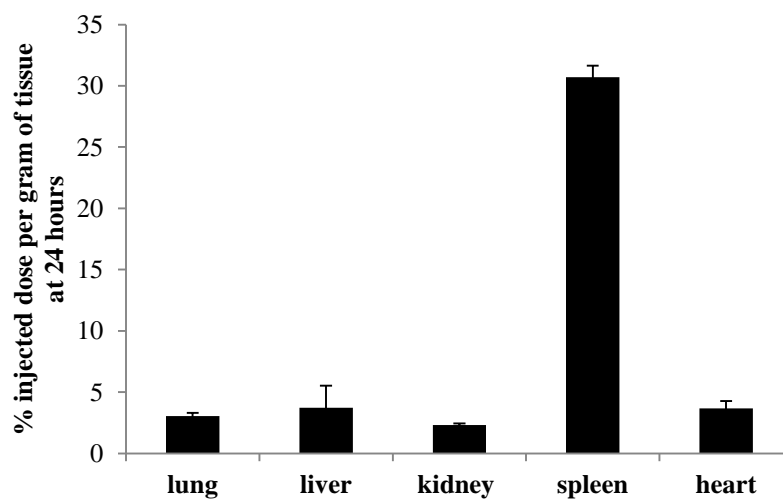


**Figure A12.** Ag content of organs of animals injected with AgNP at 24 hours post-injection.

AgNP was then administered into mice, via retro-orbital injection at a dose of 200 mg Ag/kg of body weight. The mice were then imaged using a small-animal CT scanner immediately post-injection. Figure A13 shows the resulting CT images which reveal enhancement in the bladder (white arrow). This design of the silver nanoparticle was abandoned due to the fact that administrations of the nanoparticle at doses higher than 400 mg/kg resulted in severe animal distress, leading to euthanasia. Following this, the methodology outlined in Chapter 4 to encapsulate the silver core within a silica shell is implemented.



**Figure A13.** *CT images of mice injected with 200 mg Ag/kg of body weight. Significant enhancement is observed in the bladder (white arrow).*

## SYNTHESIS OF PVP-COATED SILVER NANOPARTICLES

August 19, 2013

Roshan Karunamuni

### SCOPE AND APPLICABILITY

This method is applicable to develop polyvinylpyrrolidone (PVP)-stabilized silver nanoparticles for further modification to be used as imaging agents or other applications. The nanoparticles are spherical with a physical diameter of  $39 \pm 6$  nm.

### SUMMARY OF METHOD

The method is based on the synthesis procedure described by Silvert *et al*<sup>98</sup>, in “Preparation of colloidal silver dispersions by the polyol process”. Silver nitrate is dissolved in a mixture of ethylene glycol and PVP. The mixture is then heated to form silver nucleation sites and then maintained at constant temperature to allow for the growth of the nanoparticle to the final size. The final particles are purified by centrifugation and resuspended in ethyl alcohol.

### REFERENCES

### SAFETY

Care must be taken when cleaning glassware with nitric acid.

### MATERIALS AND SUPPLIES

#### Reagents

Deionized Water (DI) – Research grade

Nitric acid, 70% - CAS: 7697-37-2, Fisher Scientific (Stockroom): A200S212

Polyvinylpyrrolidone (PVP), Molecular Weight: 10,000 Da. – CAS: 9003-39-8, Sigma Aldrich: PVP10-100G

Silver Nitrate – CAS: 7761-88-8, Sigma Aldrich: 209139-25G

Ethylene Glycol, Certified – CAS: 107-21-1, Fisher Scientific (Stockroom): E1784

Acetone, HPLC Grade – CAS: 67-64-1, Fisher Scientific (Stockroom): A949-4

Ethanol, 200 proof, Fisher Scientific (Stockroom), ETHANOL500ML

#### Apparatus

250 mL roundbottom flask

Egg-shaped magnetic stir bar

Silica oil bath

Heating and magnetic stirring apparatus with temperature control

Stir plate -

Heating oven

Fisherbrand 50 mL centrifuge tube

Centrifuge

Sonicator

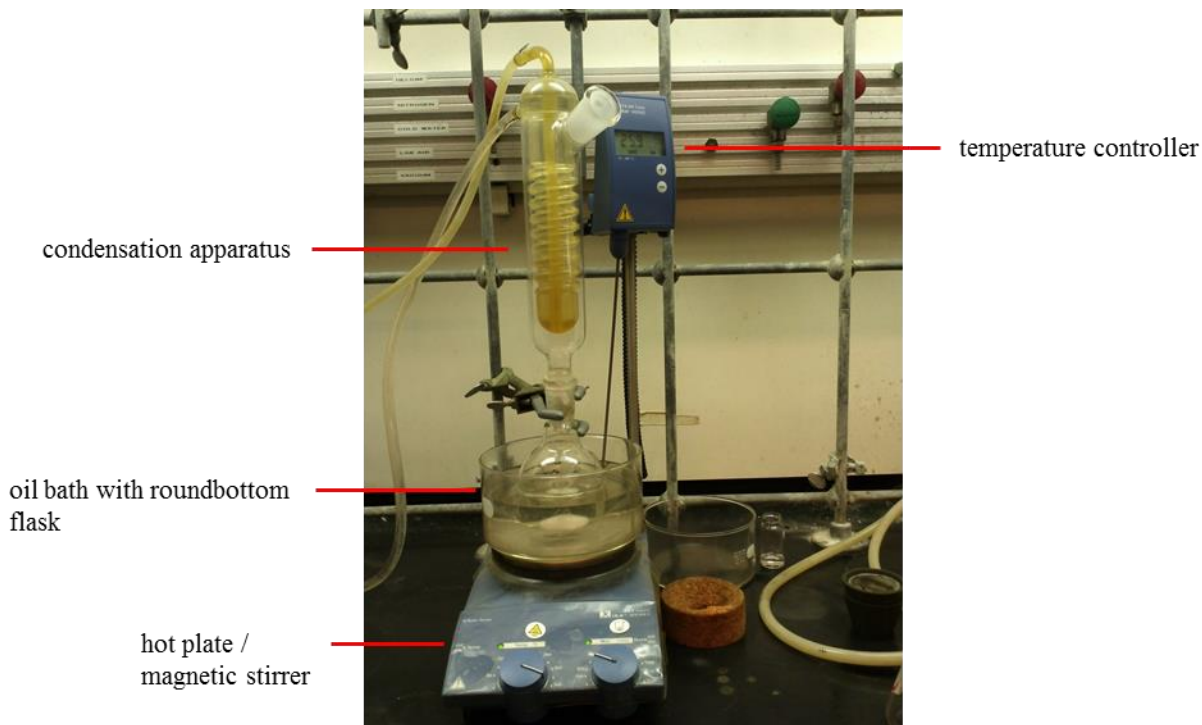
Vortex

## METHOD

Clean all glassware and magnetic stirrers with 70% nitric acid and let sit for 15 – 30 minutes. Wash with DI water, followed by acetone. Place clean apparatus in oven for 10 minutes to dry. Place in fume hood, and allow to cool to room temperature. Cap glassware openings with septa in order to prevent contamination.

Measure  $120 \pm 0.5$  mL of ethylene glycol using graduated cylinder and decant into roundbottom flask. Weigh  $2.4 \pm 0.05$  g of PVP and add directly to the ethylene glycol in the roundbottom flask. Take care when adding PVP, as the powder tends to stick to the side of the glassware. Cover the roundbottom flask with aluminum foil and stir for  $18 \pm 1$  hours on stir plate. Keep septa on roundbottom flask while stirring overnight.

Add  $80 \pm 0.05$  mg of silver nitrate to the mixture and allow to stir for 30 minutes. The aluminum foil should still be placed around the flask for this step. Make sure all the silver nitrate crystals have dissolved and transfer the roundbottom flask to the stirring/hot plate. Fit the flask with a condensation apparatus, as shown below. Increase the temperature of the bath at a rate of  $1^{\circ}\text{C}/\text{min}$  to a final temperature of  $120^{\circ}\text{C}$  under constant stirring. The temperature setting on the hot plate should be set to the maximum ( $340^{\circ}\text{C}$ ) while manually increasing the temperature using the temperature controller in  $10^{\circ}\text{C}$  steps until the desired value is reached. The stirring motor should be set at 250 rotations per minute.



The temperature is maintained at  $120^{\circ}\text{C}$  for 1 hour. Immediately afterwards, the roundbottom flask is immersed in cold water to terminate the reaction. Once the reaction vessel has reached room temperature, the silver nanoparticle is split into 12x 50mL centrifuge tubes (10 mL each). 40 mL of acetone is then added to each tube. The tubes are then centrifuged at  $4000 \times g$  for 15 minutes. The particles are resuspended in 25 mL of 100% ethyl alcohol. The particles are then purified with 2x centrifuge/ suspension cycles of  $18,000 \times g$  for 15 minutes and resuspended in a final total volume of 8 mL. In all the centrifuge

cycles described above, the supernatant is discarded and the nanoparticle pellet is resuspended in ethyl alcohol. The particles can be resuspended with the help of sonication or/and vortexing.

## **TEM OF SILVER NANOPARTICLES**

August 22, 2013

Roshan Karunamuni

### **SCOPE AND APPLICABILITY**

This method is used to image nanoparticles using transmission electron microscopy (TEM). The physical diameter of the nanoparticles can be determined from the images collected. This method is only applicable for nanoparticle solutions consisting of high atomic number materials such as silver or gold.

### **SUMMARY OF METHOD**

The nanoparticle solution is placed on a TEM grid, and the solvent is allowed to evaporate. The grid is then imaged using the JOEL-1010 Transmission electron microscope in the Electron Microscopy Resource Laboratory. Further information regarding the core facilities can be found here:

<https://somapps.med.upenn.edu/pbr/portal/morph/tech.php>

### **REFERENCES**

N/A

### **SAFETY**

N/A

### **MATERIALS AND SUPPLIES**

#### **Reagents**

Silver Nanoparticle Solution

#### **Apparatus**

JOEL-1010 Transmission electron microscope

Carbon-coated copper TEM grids 200 mesh, Polysciences (www.polysciences.com), Product No: 24918-25

### **METHOD**

The nanoparticle solution must be diluted with de-ionized water. If the nanoparticles are immersed in a solvent that is not miscible with water, excess solvent may be used instead. 20  $\mu$ L of the diluted nanoparticle solution is placed on the TEM grid. The grid is allowed to dry on a paper towel for 1 hour.

The Electron Microscopy Resource Laboratory is located on the first floor of the Richards building in B110. All users of the core facility services must first complete the necessary training. Request for training can be completed on the website or in person. Please contact Dewight Williams (dewight@mail.med.upenn.edu) for further instruction. Scheduling to reserve time on the JOEL TEM must be completed online by using the "Scheduling" menu option. Funding source from the available options must be selected to continue. Select the appropriate microscope, and reserve the required time.



Ensure the beam is off, and pull the grid holder straight out until you cannot go further. Rotate counter-clockwise and then pull out of microscope. Place the grid onto the grid holder using tweezers, and insert the holder back into the microscope. Push holder into inlet, wait until the green light goes off, and then rotate clockwise and slowly allow the holder back into microscope. The vacuum will pull the holder back and in, and so the user must resist to ensure that the holder moves in smoothly and slowly. Turn on the beam. Modify the magnification, intensity, and focus as required in order to visualize the particles. Capture imaging using software on secondary screen, and save as 'tiff' file format. Once image collection has been completed, turn off the beam, remove the grid holder and grid. Record the location of the grid in the laboratory grid array in the log.

## **UV/VIS SPECTRA OF SILVER NANOPARTICLES**

August 22, 2013

Roshan Karunamuni

### **SCOPE AND APPLICABILITY**

This method is used to measure the optical absorbance of silver nanoparticles in the Ultraviolet / Visible (UV/Vis) range. The technique can be applied to metallic nanoparticles that exhibit a surface plasmon resonance (SPR) in this energy range. The polystyrene cuvettes in this protocol can be used to scan wavelengths longer than 350 nm. For shorter wavelengths, quartz or methacrylate cuvettes must be employed.

### **SUMMARY OF METHOD**

The absorbance of the nanoparticles is measured using a spectrometer at the wavelengths to be studied. A polystyrene semi-micro cuvette is used to hold the sample while the absorbance is measured.

### **REFERENCES**

N/A

### **SAFETY**

N/A

### **MATERIALS AND SUPPLIES**

#### **Reagents**

Silver Nanoparticle Solution

Deionized Water (DI) – Research grade

#### **Apparatus**

Polystyrene semi-micro cuvette, small volume (1.5 mL), Fisher Scientific, Cat No: S759075D

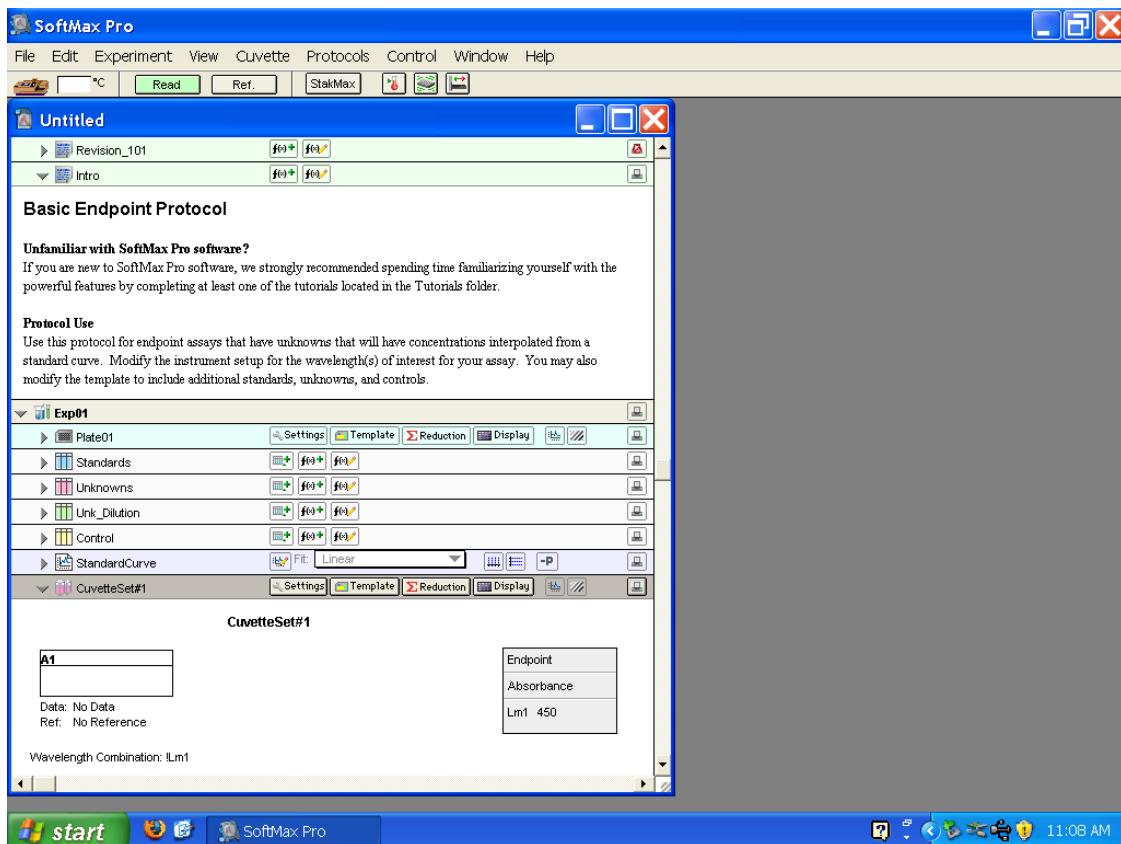
Molecular Devices SpectraMax M5 microplate reader

### **METHOD**

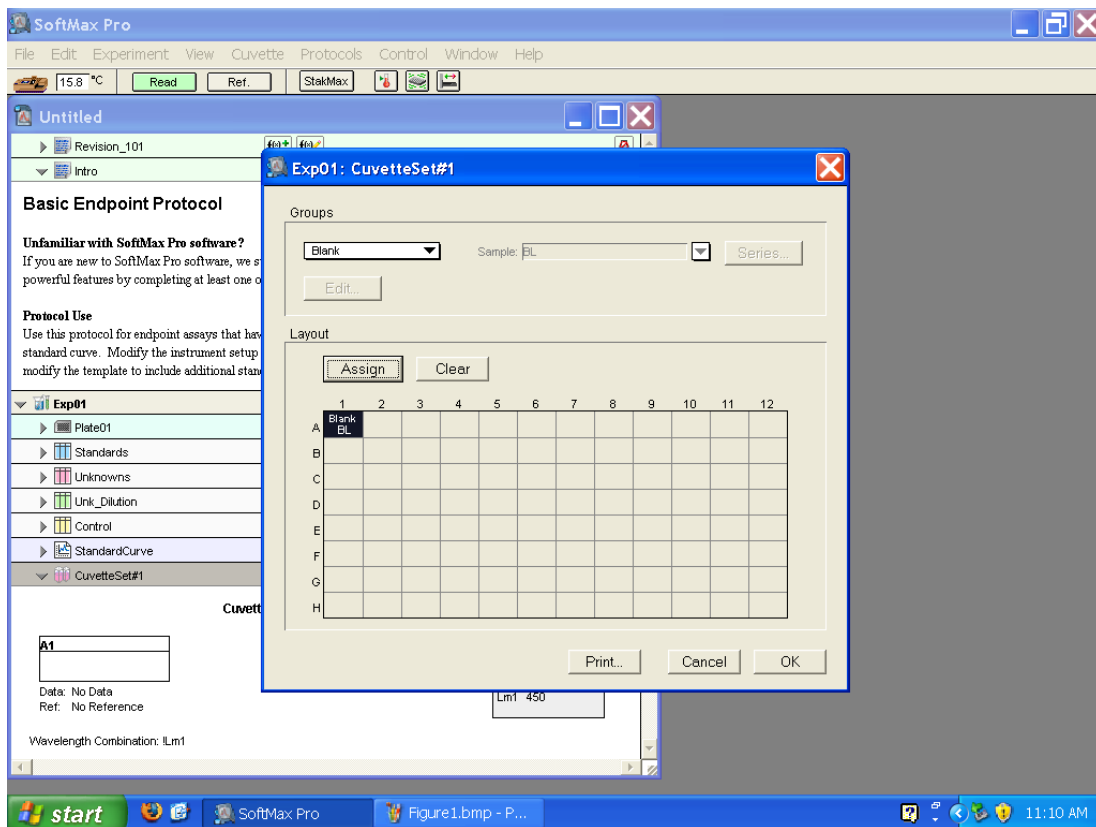
Dilute the silver nanoparticle solution with deionized water. Add 700  $\mu$ L of the diluted silver nanoparticle solution and into a polystyrene cuvette. Add 700  $\mu$ L of DI water to an additional cuvette – this will serve as the “blank” control to normalize the absorbance of the silver nanoparticle solution.

Start the Softmax Pro software.

Under Experiment → New Cuvette Set. The following box titled “Cuvette Set 1” should appear.

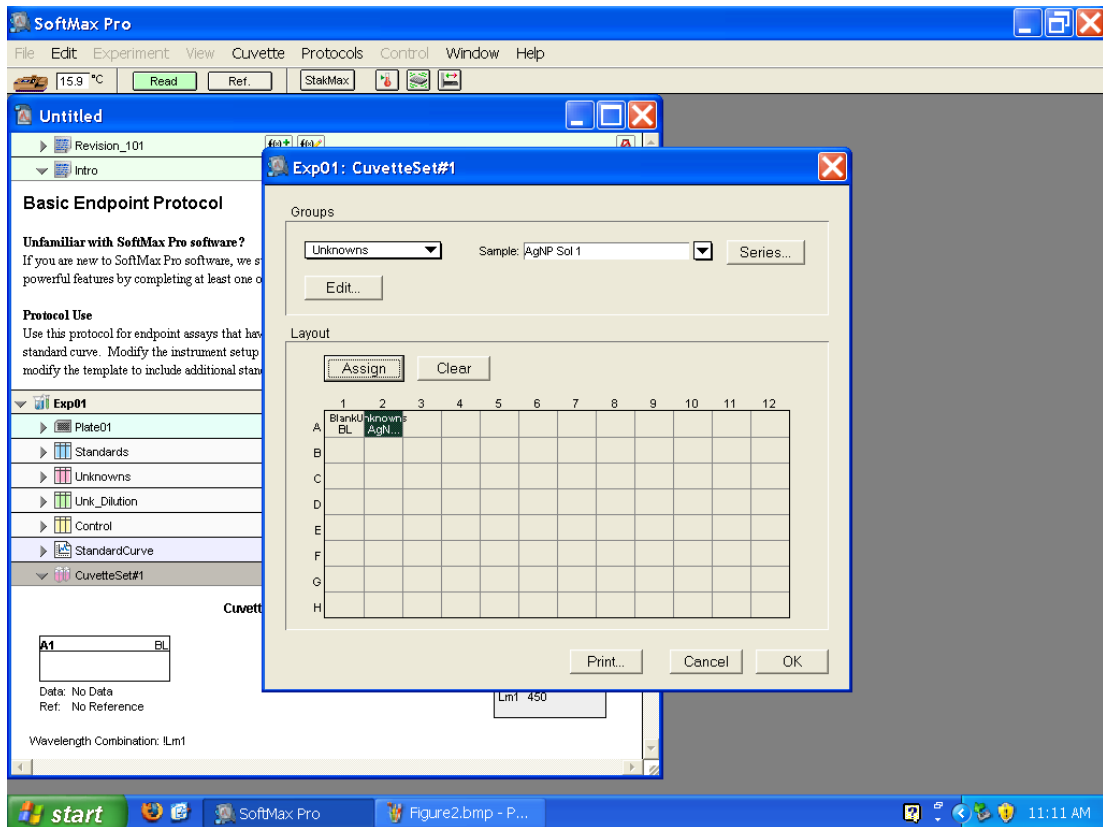


Click the “Template” tab. Assign the cell “A1” to “Blank”.



Assign cell “A2” to “Unknowns”. Additional nanoparticle solutions can be assigned separate cells (A3, A4...)

Once all the necessary cells have been assigned, click “OK”

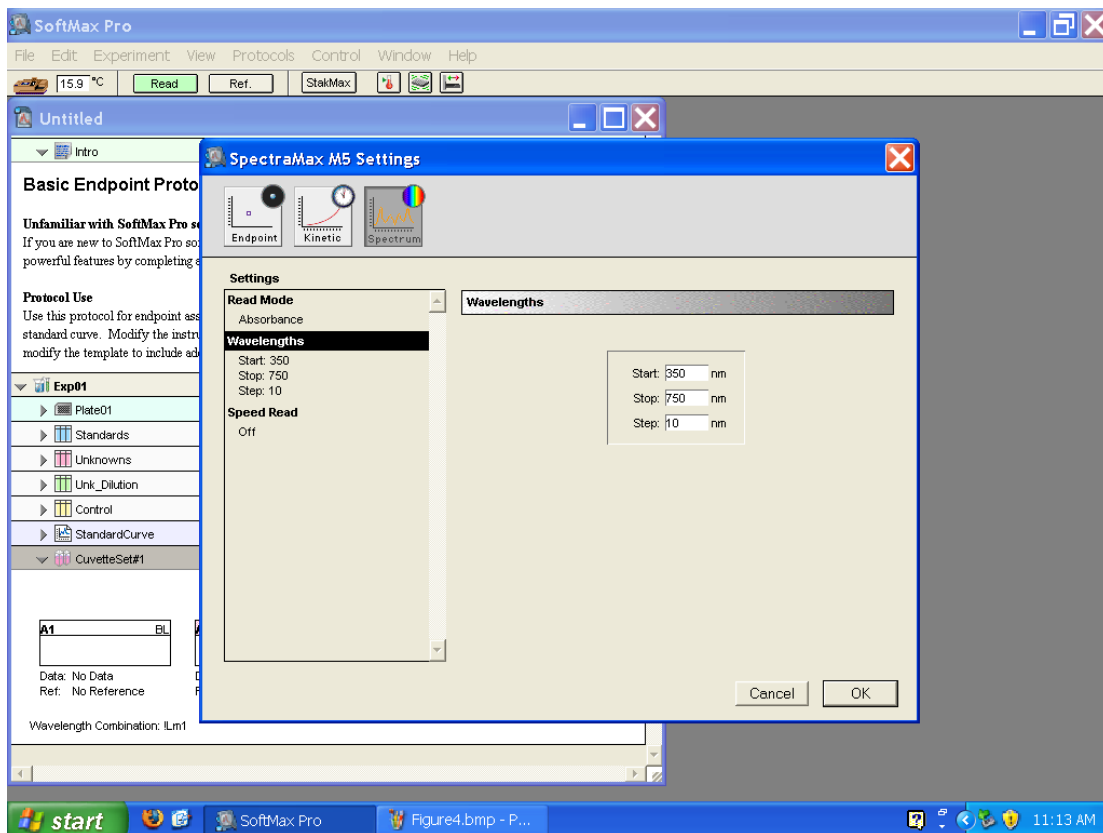


Click the “Settings” tab. Select “Spectrum” to obtain the absorbance of the nanoparticle solution at multiple wavelengths.

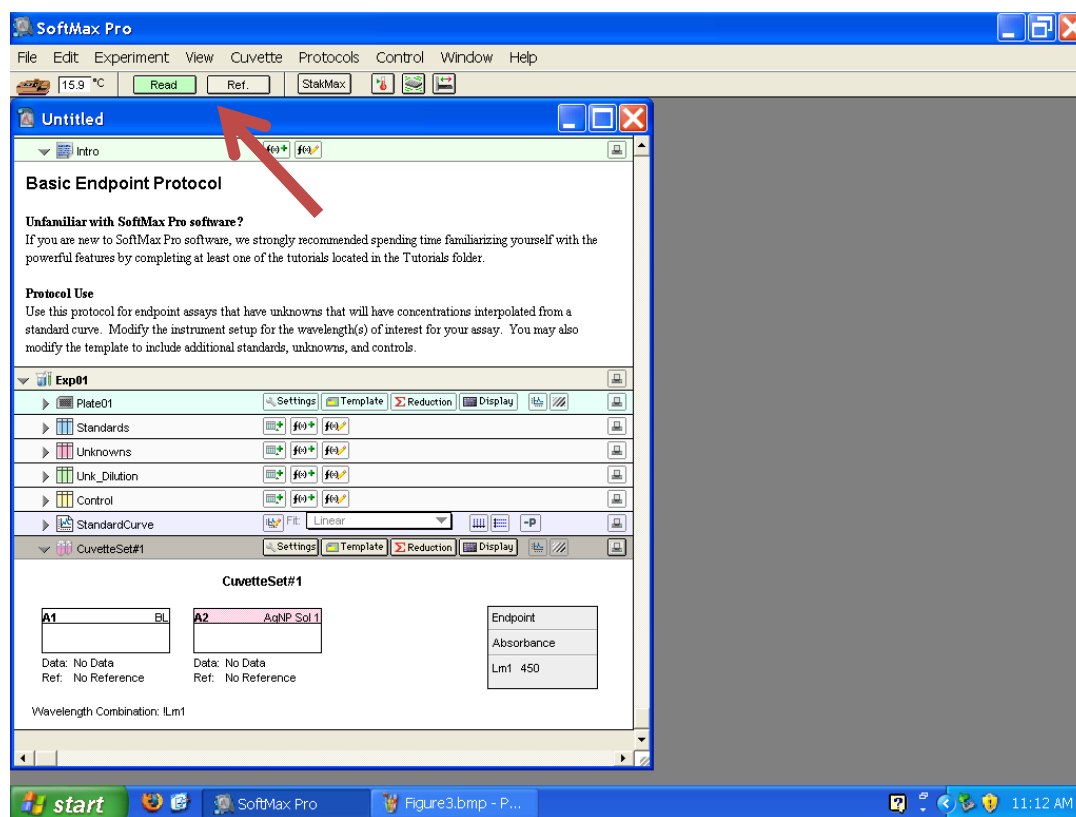
Ensure the “Read Mode” is set to “Absorbance”.

By selecting “Wavelengths”, the range of wavelengths to be scanned can be selected.

Once completed, click “OK”.



Insert the blank cuvette into the reader. Select the blank cell “A1”, and click “Read” on the front panel.



Once the scan has been completed, the remaining cells can be completed in the same manner. The absorbance values of the “Unknowns” will automatically be normalized against the “blank” cell values.

The data can be saved in a text file format using File → Import/Export → Export.

## **DYNAMIC LIGHT SCATTERING OF SILVER NANOPARTICLES**

August 23 2013

Roshan Karunamuni

### **SCOPE AND APPLICABILITY**

This method is used to measure the hydrodynamic diameter of the silver nanoparticles in solution. The hydrodynamic diameter of a colloidal solution includes ligands that are present on the surface of the nanoparticle, and cannot be visualized directly using transmission electron microscopy (TEM). For example, the PVP-stabilized silver nanoparticle core is easily visualized using TEM. However, the PVP ligands stabilizing the silver core are not visible as they are not electron-dense. The difference between the physical diameter measured by TEM and hydrodynamic diameter measured by DLS is a result of the PVP ligand.

### **SUMMARY OF METHOD**

The nanoparticles are placed in a low-volume disposable cuvette. The hydrodynamic diameter of the nanoparticles are measured using the Zetasizer. There are three distributions reported by the instrument: Intensity, Number, and Volume. The basic distribution obtained from the instrument is intensity. The intensity and volume distributions are generated from the intensity data. The PDI (polydispersity index) reported by the instrument can be used to assess the polydispersity of a nanoparticle solution. Solutions with PDI less than 0.2 can be assumed to be of good quality with a low polydispersity.

### **REFERENCES**

N/A

### **SAFETY**

N/A

### **MATERIALS AND SUPPLIES**

#### **Reagents**

Silver Nanoparticle solution

#### **Apparatus**

Zetasizer

Polystyrene semi-micro cuvette, small volume (1.5 mL), Fisher Scientific, Cat No: S759075D

### **METHOD**

Start the Zetasizer software.

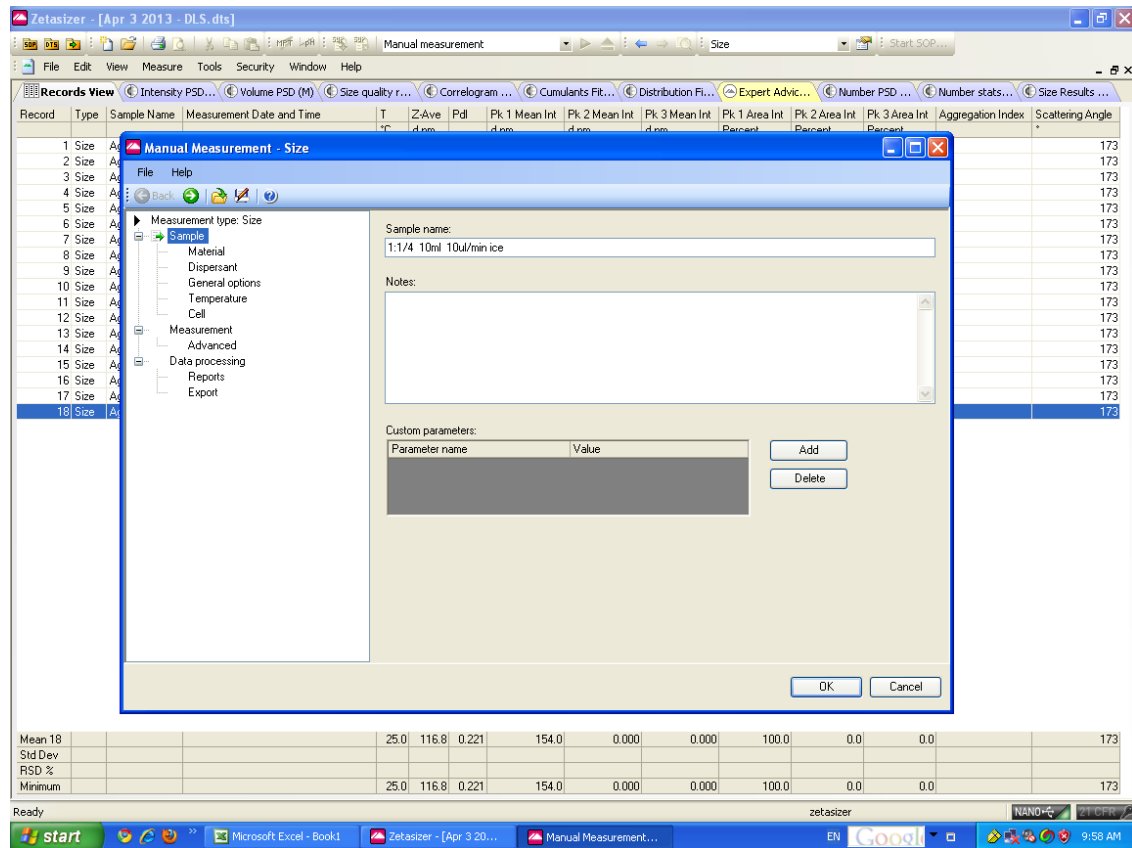
File → Open → Measurement File



Select a previously created measurement file. Alternatively, create a new measurement file using: (File → New → Measurement File)

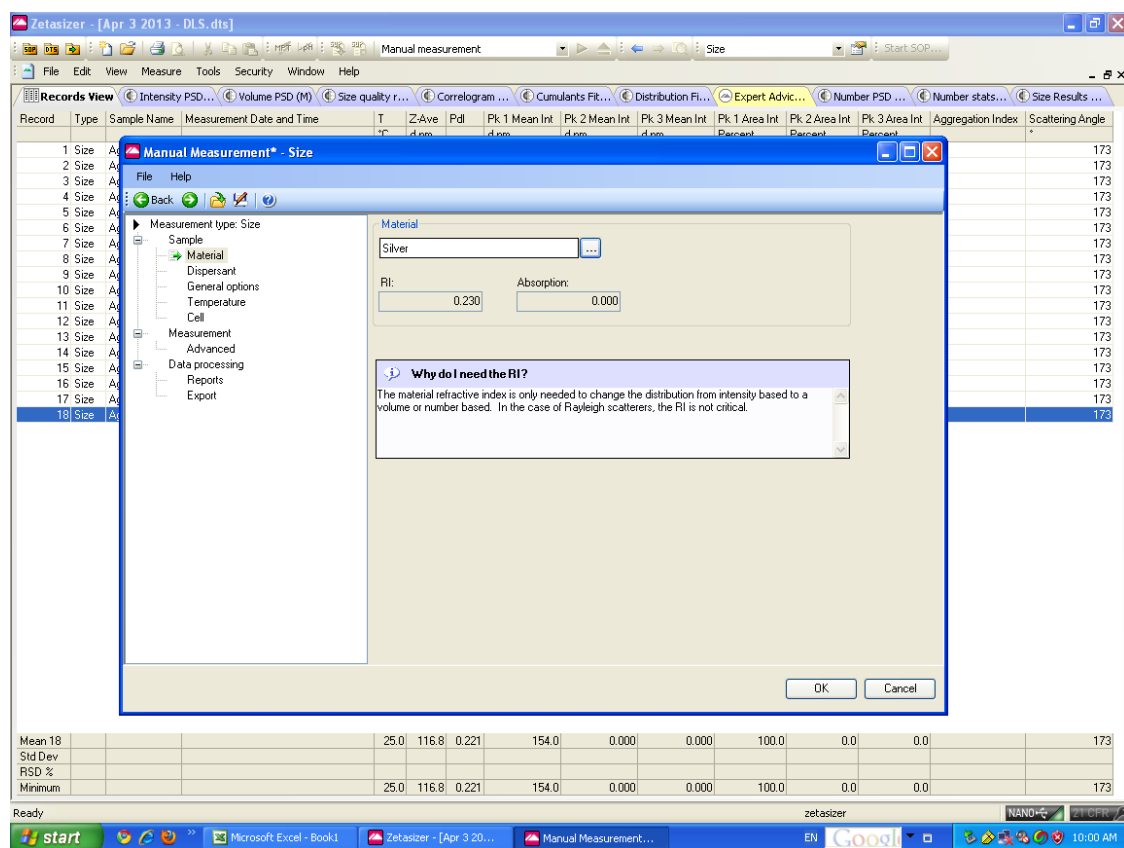
Measure → Manual

The following Manual Measurement dialog box will appear:



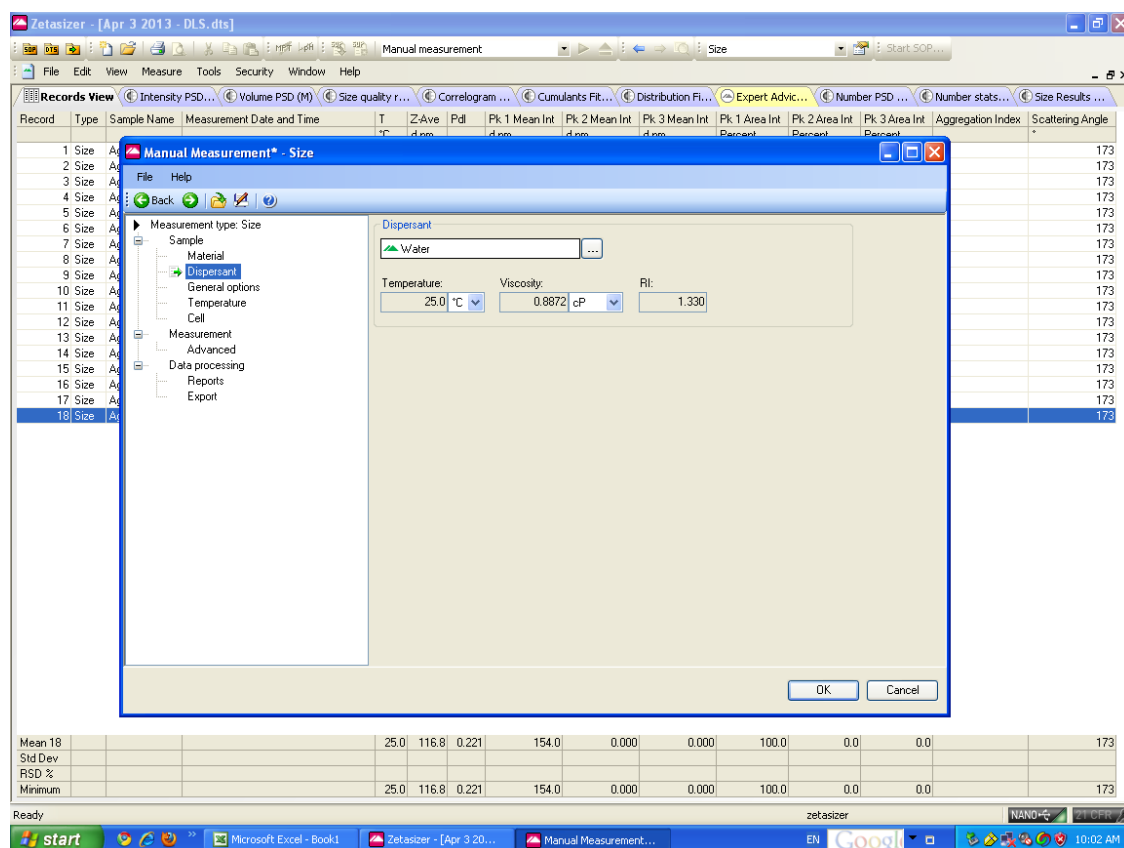
Ensure that the measurement type is set to “Size”. Under the “Sample” menu option, enter an appropriate sample name.

Under “Material” select Silver.



The values of refractive index (RI) and Absorption can be modified if needed.

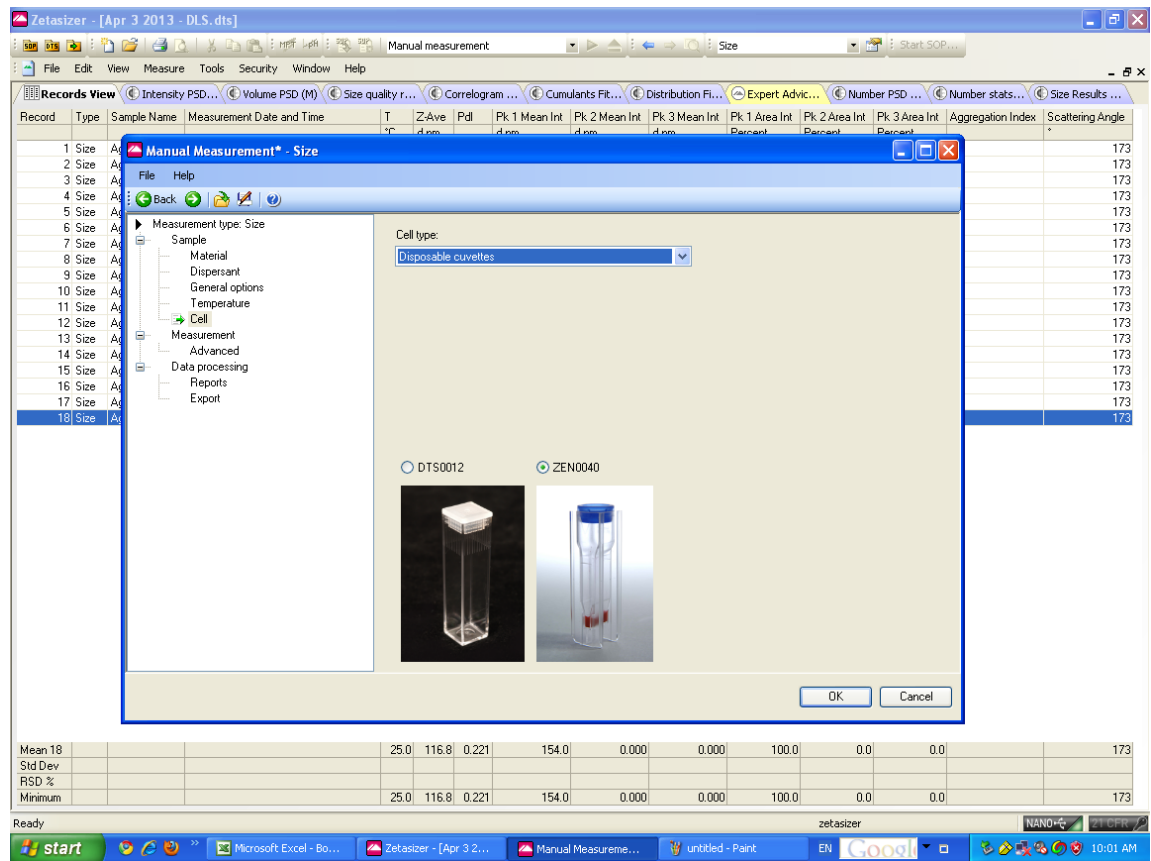
Under “Dispersant”, select the solvent used for the nanoparticle solution:



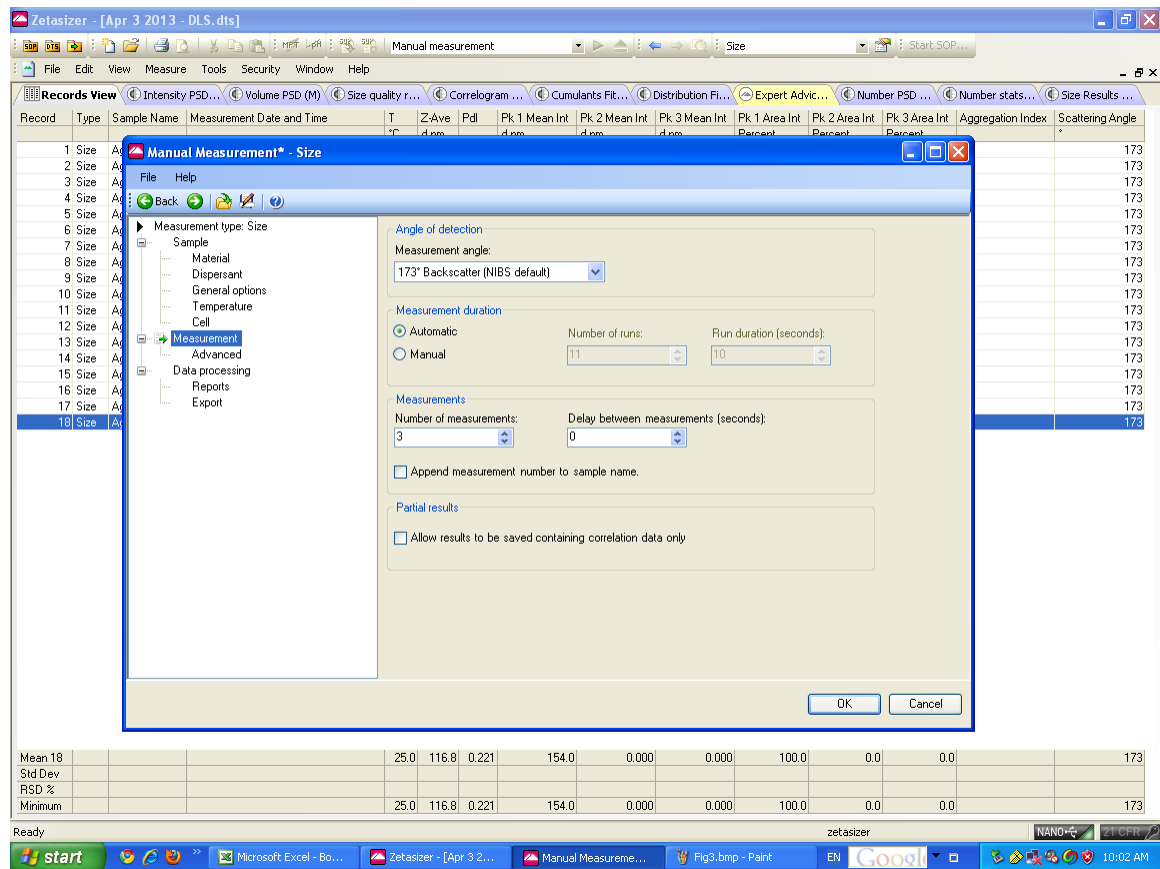
The viscosity and RI values will autopopulate once a solvent is chosen.

Typically, the silver nanoparticle solution should be diluted with deionized water, before being used for the DLS measurement.

Under “Cell”, select “Disposable cuvettes:” for the “Cell type”. Select the “ZEN0040” radio button to select the low-volume option.



Under “Measurement”, ensure that the “Measurement angle” is set to its default value of “173° Backscatter (NIBS default)”. The number of measurements should be set to 3.



Once all the options have been selected, clicking “OK” will bring up the measurement dialog box. At this point, place the cuvette inside the instrument and start collecting data. Once data collection completion, the three measurements (each with Volume, Intensity, and Number distributions) will be visible in the measurement file.

Record	Type	Sample Name	Measurement Date and Time	T °C	Z-Ave d.nm	Pd	Pk 1 Mean Int d.nm	Pk 2 Mean Int d.nm	Pk 3 Mean Int d.nm	Pk 1 Area Int Percent	Pk 2 Area Int Percent	Pk 3 Area Int Percent	Aggregation Index	Scattering Angle °
1	Size	AgNP-PVP 1	Wednesday, April 03, 2013 5:02:45 PM	25.0	125.0	0.264	178.0	26.86	0.000	95.5	4.5	0.0		173
2	Size	AgNP-PVP 2	Wednesday, April 03, 2013 5:04:50 PM	25.0	126.8	0.275	181.4	0.000	0.000	100.0	0.0	0.0		173
3	Size	AgNP-Oct 1	Wednesday, April 03, 2013 5:11:19 PM	25.0	964.7	0.257	1033	5008	0.000	95.0	5.0	0.0		173
4	Size	AgNP-Oct 2	Wednesday, April 03, 2013 5:13:35 PM	25.0	995.6	0.263	1397	0.000	0.000	100.0	0.0	0.0		173
5	Size	AgNP-PEG 1	Wednesday, April 03, 2013 5:24:11 PM	25.0	145.4	0.252	185.8	4425	0.000	97.5	2.5	0.0		173
6	Size	AgNP-PEG 2	Wednesday, April 03, 2013 5:26:37 PM	25.0	146.0	0.256	169.3	1427	0.000	88.6	11.4	0.0		173
7	Size	AgNP-PEG 3	Wednesday, April 03, 2013 5:29:03 PM	25.0	146.7	0.274	220.2	0.000	0.000	100.0	0.0	0.0		173
8	Size	AgNP1 1	Tuesday, July 02, 2013 4:39:48 PM	25.0	141.1	0.267	198.8	0.000	0.000	100.0	0.0	0.0		173
9	Size	AgNP1 2	Tuesday, July 02, 2013 4:42:01 PM	25.0	144.8	0.277	208.2	0.000	0.000	100.0	0.0	0.0		173
10	Size	AgNP1 3	Tuesday, July 02, 2013 4:44:15 PM	25.0	147.7	0.282	220.6	0.000	0.000	100.0	0.0	0.0		173
11	Size	AgNP1 1	Tuesday, July 02, 2013 4:54:45 PM	25.0	110.1	0.206	141.0	0.000	0.000	100.0	0.0	0.0		173
12	Size	AgNP1 2	Tuesday, July 02, 2013 4:57:10 PM	25.0	112.5	0.212	146.0	0.000	0.000	100.0	0.0	0.0		173
13	Size	AgNP1 3	Tuesday, July 02, 2013 4:59:34 PM	25.0	113.3	0.213	147.1	0.000	0.000	100.0	0.0	0.0		173
14	Size	AgNP1 1	Tuesday, July 02, 2013 5:26:09 PM	25.0	103.5	0.219	134.7	0.000	0.000	100.0	0.0	0.0		173
15	Size	AgNP1 2	Tuesday, July 02, 2013 5:26:40 PM	25.0	106.7	0.220	138.8	0.000	0.000	100.0	0.0	0.0		173
16	Size	AgNP1 1	Tuesday, July 02, 2013 5:32:26 PM	25.0	117.7	0.210	152.2	0.000	0.000	100.0	0.0	0.0		173
17	Size	AgNP1 2	Tuesday, July 02, 2013 5:34:40 PM	25.0	117.6	0.206	150.5	0.000	0.000	100.0	0.0	0.0		173
18	Size	AgNP1 3	Tuesday, July 02, 2013 5:36:55 PM	25.0	116.8	0.221	154.0	0.000	0.000	100.0	0.0	0.0		173
19	Size	AgNP-1	Friday, August 23, 2013 10:06:10 AM	25.0	121.8	0.250	159.3	0.000	0.000	100.0	0.0	0.0		173
20	Size	AgNP-1	Friday, August 23, 2013 10:08:24 AM	25.0	122.2	0.234	159.9	0.000	0.000	100.0	0.0	0.0		173
21	Size	AgNP-1	Friday, August 23, 2013 10:10:38 AM	25.0	119.1	0.263	165.2	18.99	0.000	97.2	2.8	0.0		173

Individual distributions can be printed as image files to be used for further analysis.

## SILICA ENCAPSULATION OF PVP-STABILIZED SILVER NANOPARTICLES

August 28, 2013

Roshan Karunamuni

### SCOPE AND APPLICABILITY

This method is used to encapsulate polyvinylpyrrolidone (PVP) stabilized silver nanoparticles (AgNP) with a silica (Si) shell. The thickness of the shell can be optimized by changing the amount of Si added to the reaction. The method can be used to encapsulate any PVP-stabilized nanoparticle. The method presented adds a  $63 \pm 7$  nm shell of Si onto a  $39 \pm 6$  nm Ag core.

### SUMMARY OF METHOD

The method is based on the procedure described by Graf *et al.*<sup>110</sup>, “A General Method to Coat Colloidal Particles with Silica”. PVP-stabilized AgNP are dispersed in ethyl alcohol. A mixture of ammonium hydroxide (which serves as the catalyst) and tetraethoxysilane (TES, which serves as the source of Si atoms) is then added to the nanoparticle solution. The reaction is left stirring overnight, after which the particles are purified from unwanted reactions through centrifugation. The final Si-coated AgNP are then resuspended in ethyl alcohol for further modification and analysis.

### REFERENCES

C. Graf, D.L.J. Vossen, A. Imhof, and A. van Blaaderen, “A General Method To Coat Colloidal Particles with Silica,” *Langmuir* **19**(17), 6693–6700 (2003).

### SAFETY

Care must be taken when cleaning glassware with nitric acid.

### MATERIALS AND SUPPLIES

#### Reagents

Nitric acid, 70% - CAS: 7697-37-2, Fisher Scientific (Stockroom): A200S212

Ethanol, 200 proof, Fisher Scientific (Stockroom), ETHANOL500ML

Tetraethyl orthosilicate, CAS: 78-10-4, Sigma Aldrich: 131903-25ML

Ammonium Hydroxide, CAS: 7664-41-7, Fisher Scientific: A669

PVP-stabilized AgNP

#### Apparatus

50 mL roundbottom flask

magnetic stir bar

Stir plate -

Heating oven

Centrifuge

1.5 mL microcentrifuge tubes

Sonicator

Vortex

## METHOD

Clean all glassware and magnetic stirrers with 70% nitric acid and let sit for 15 – 30 minutes. Wash with DI water, followed by acetone. Place clean apparatus in oven for 10 minutes to dry. Place in fume hood, and allow to cool to room temperature. Cap glassware openings with septa in order to prevent contamination.

Every synthesis batch whose manufacture is described in SOP1: Synthesize PVP-coated silver nanoparticles is referred to as 1 unit of AgNP. Resuspend 2 units of AgNP in ethyl alcohol using sonication and vortexing. Add ethyl alcohol to a total volume of  $30.3 \pm 0.1$  mL. Place the AgNP solution in a 50 mL roundbottom flask with a magnetic stirrer and leave to stir on the stir plate for  $5 \pm 1$  hours. The flask should be covered in aluminum foil while the AgNP solution is stirring. The stir plate should be set at level 4.

Prepare a 10% solution of TES in ethyl alcohol ( $240 \pm 1$   $\mu$ L TES added to  $2160 \pm 1$   $\mu$ L of ethyl alcohol). Add  $1330 \pm 1$   $\mu$ L of ammonium hydroxide and the total 2400  $\mu$ L of 10% TES solution into the AgNP solution. The TES solution should be added immediately after the ammonium hydroxide solution. Leave the mixture to stir for  $12 \pm 1$  hour. Keep septa on the roundbottom flask while the AgNP solution is stirring.

Once the reaction has been completed, the Si-encapsulated AgNP can be purified by centrifuging the nanoparticles placed in 1.5 mL microcentrifuge tubes at 14,000 xg for 15 minutes. The centrifugation and suspension procedure should be repeated three times to ensure that the majority of the unwanted reactants have been removed. The final Si-encapsulated AgNP are resuspended in 5 mL of ethyl alcohol with the help of sonication and vortexing. The solution can then be used for further reaction procedures or analysis.



## AMINATION OF SILICA NANOPARTICLES

November 20, 2013

Roshan Karunamuni

### SCOPE AND APPLICABILITY

This method is used to add amine (-NH<sub>2</sub>) groups to the surface of silica nanoparticles. Once the silica nanoparticles have been functionalized with terminal amine groups, they can be further modified using N-Hydroxysuccinimide (NHS)-containing ligands.

### SUMMARY OF METHOD

The method is based on the procedure described by Westcott *et al.*<sup>143</sup>, “Formation and adsorption of clusters of gold nanoparticles onto functionalized silica nanoparticle surfaces.” The particles are mixed with 3-aminopropyltrimethoxysilane (APTMS) – which serves as the source of the amine groups – overnight and then brought to a low boil. The reaction is terminated and the excess materials are removed using centrifugation. The function group (amine) can be substituted for other functional groups by selection of an appropriate trialkoxyorganosilane. For example, mercaptopropyltrimethoxysilane (MPTMS) can be used to introduce terminal thiol (-SH) groups to the surface of the nanoparticles.

### REFERENCES

S.L. Westcott, S.J. Oldenburg, T.R. Lee, and N.J. Halas, “Formation and Adsorption of Clusters of Gold Nanoparticles onto Functionalized Silica Nanoparticle Surfaces,” *Langmuir* **7463**(12), 5396–5401 (1998)

### SAFETY

Care must be taken when cleaning glassware with nitric acid.

### MATERIALS AND SUPPLIES

#### Reagents

Nitric acid, 70% - CAS: 7697-37-2, Fisher Scientific (Stockroom): A200S212

Ethanol, 200 proof, Fisher Scientific (Stockroom), ETHANOL500ML

3-aminopropyltrimethoxysilane (APTMS), CAS: 13822-56-5, Sigma-Aldrich: 281778-100ML

Silica nanoparticles

#### Apparatus

50 mL roundbottom flask

magnetic stir bar

Stir plate -

Heating oven

Centrifuge

1.5 mL microcentrifuge tubes

Hot plate with oil bath  
Condenser

## METHOD

Clean all glassware and magnetic stirrers with 70% nitric acid and let sit for 15 – 30 minutes. Wash with DI water, followed by acetone. Place clean apparatus in oven for 10 minutes to dry. Place in fume hood, and allow to cool to room temperature. Cap glassware openings with septa in order to prevent contamination.

Determine the mass of the silica-silver nanoparticles to be aminated. This can be estimated by measuring the mass of the pellet that is formed after centrifugation. Use the following table to determine the amount of APTMS needed and the volume of the final solution in ethanol:

Number of silica nanoparticles:	7.00E+14
Volume of APTMS (μL)	50
Volume of final solution (mL of ethanol)	100

Add ethanol to the solution of silica nanoparticles to reach the desired final volume. Place the solution in the 50 mL roundbottom flask (larger or smaller sizes can be used depending on the volumes) with a magnetic stir bar. Add the required volume of APTMS and cover the flask with aluminum foil. Place the flask on top of the magnetic stirrer (setting at 4) and leave mixing for 12 hours.

Attach the condenser to the roundbottom flask, and place the setup in the oil bath on top of the hot plate. Set the temperature to 55 °C, and the rotations per minute of the magnetic stirrer to 250. Leave the system to react for 1 hour after the temperature has reached 55 °C. Remove the flask from the oil bath and allow it to reach room temperature – this generally takes 15 minutes. The amine-silica nanoparticles can be purified by centrifuging at 14,000 xg for 15 minutes. The centrifugation and suspension procedure should be repeated three times to ensure that the majority of the unwanted reactants have been removed. The final amine-silica nanoparticles are resuspended in 2 mL of ethyl alcohol with the help of sonication and vortexing. The solution can then be used for further reaction procedures or analysis.

## ATTACHMENT OF PEG LIGANDS ONTO AMINE-SILICA NANOPARTICLES

November 20, 2013

Roshan Karunamuni

### SCOPE AND APPLICABILITY

This method is used to attach polyethylene glycol ligands with terminal N-Hydroxysuccinimide (NHS) groups to the surface of amine-silica nanoparticles. This can be used to make the silica nanoparticles hydrophilic and therefore transferable to biological applications.

### SUMMARY OF METHOD

The method is based on the tendency for NHS groups to react with primary amines. The amine-silica nanoparticles are mixed with an excess of PEG-NHS in ethanol for 1.5 hours, and then centrifuged and re-dispersed in research-grade de-ionized (RGDI) water. PEG-NHS is only partially soluble in ethanol, and will eventually precipitate out if the reaction is allowed to continue (beyond 1.5 hours).

### REFERENCES

### SAFETY

Care must be taken when cleaning glassware with nitric acid.

### MATERIALS AND SUPPLIES

#### Reagents

Nitric acid, 70% - CAS: 7697-37-2, Fisher Scientific (Stockroom): A200S212

Ethanol, 200 proof, Fisher Scientific (Stockroom), ETHANOL500ML

mPEG-SG (PEG-NHS), Creative PEG Works: PSB-220

Amine-silica nanoparticles

#### Apparatus

25 mL roundbottom flask

magnetic stir bar

Stir plate -

Centrifuge

1.5 mL microcentrifuge tubes

### METHOD

Clean all glassware and magnetic stirrers with 70% nitric acid and let sit for 15 – 30 minutes. Wash with DI water, followed by acetone. Place clean apparatus in oven for 10 minutes to dry. Place in fume hood, and allow to cool to room temperature. Cap glassware openings with septa in order to prevent contamination.

Determine the mass of the silica-silver nanoparticles to be aminated. This can be estimated by measuring the mass of the pellet that is formed after centrifugation. Use a 2 or 3 times excess (in grams) of PEG-NHS.

Dissolve the PEG-NHS in 200 proof ethanol to a final concentration of 10 mg/mL. This may require sonication. Immediately, add the solution to the 25 mL roundbottom flask. Re-disperse the amine-silica nanoparticles in 5 mL of ethanol and add to the roundbottom flask. Cover the flask with aluminum foil, and allow to mix for 1.5 hours. The nanoparticles can be purified by centrifuging at 14,000 xg for 15 minutes. The centrifugation and resuspension procedure should be repeated three times to ensure that the majority of the unwanted reactants have been removed. The particles can be further purified using a dialysis membrane with a molecular weight cutoff of 10,000 Daltons, and filtering with a 0.2  $\mu$ m surfactant-free- cellulose acetate (SFCA) syringe filter.

## REFERENCES

- <sup>1</sup> G. Ullman, M. Sandborg, D.R. Dance, M. Yaffe, and G. Alm Carlsson, "A search for optimal x-ray spectra in iodine contrast media mammography.," *Phys. Med. Biol.* **50**(13), 3143–52 (2005).
- <sup>2</sup> W.R. Brody *et al.*, "Dual-Energy Radiography : Inital Clinical Experience," *AJR. Am. J. Roentgenol.* **137**, 201–5 (1981).
- <sup>3</sup> B. Jacobson, "Dichromatic absorption radiography. Dichromotography," *Acta Radiol.* **39**, 437 (1953).
- <sup>4</sup> T.L. Houk, R.A. Kruger, and C.A. Mistretta, "Real-time digital k-edge subtraction flourscopy," *Invest. Radiol.* **14**, 270–8 (1979).
- <sup>5</sup> R.E. Alvarez and A. Macovski, "Energy-selective reconstructions in X-ray computerized tomography," *Phys. Med. Biol.* **21**(5), 733–44 (1976).
- <sup>6</sup> L.A. Lehmann, R.E. Alvarez, A. Macovski, and W.R. Brody, "Lehmann - Generalized image combinations in dual KVP digital radiography," *Med. Phys.* **8**(5), 659–667 (1981).
- <sup>7</sup> P.C. Johns, D.J. Drost, M. Yaffe, and A. Fenster, "Dual-energy mammography: Inital experimental results," *Med. Phys.* **12**(3), 297–304 (1985).
- <sup>8</sup> P.C. Johns and M. Yaffe, "Theoretical optimization of dual-energy x-ray imaging with application to mammography," *Med. Phys.* **12**(3), 289–296 (1985).
- <sup>9</sup> C. Paul *et al.*, "Dual Energy Mammographic Imaging," *SPIE Proc.* **419**, 201–208 (1983).
- <sup>10</sup> P.C. Johns and M.J. Yaffe, "X-ray characterisation of normal and neoplastic breast tissues," *Phys. Med. Biol.* **32**(6), 675–95 (1987).
- <sup>11</sup> G.N. Hounsfield, "Computerized transverse axial scanning description of system," *Br. J. Radiol.* **46**, 1016–1022 (1973).
- <sup>12</sup> S.J. Riederer and C.A. Mistretta, "Selective iodine imaging using K-edge energies in compterized x-ray tomography," *Med. Phys.* **4**(6), 474–481 (1977).
- <sup>13</sup> D.P. Chakraborty and G.T. Barnes, "An energy sensitive cassette for dual-energy mammography," *Med. Phys.* **16**(1), 7–13 (1988).
- <sup>14</sup> J.M. Boone, G.S. Shaber, and M. Tecotzky, "Dual-energy mammography: A detector analysis," *Med. Phys.* **17**(4), 665–675 (1990).
- <sup>15</sup> J.M. Boone, "Color mammography: image generation and receiver operating characteristic evaluation," *Invest. Radiol.* **26**(6), (1991).
- <sup>16</sup> A. Santamaria-Pang *et al.*, "Automated Liver Lesion Characterization using fast kVp switching Dual Energy Computed Tomography Imaging," *Proc SPIE* **7624**, 76240V–76240V–10 (2010).

- 17 K. Matsumoto, M. Jinzaki, Y. Tanami, A. Ueno, M. Yamada, and S. Kuribayashi, "Virtual Monochromatic Spectral Imaging with Fast Kilovoltage Switching: Improved Image Quality as Compared with That Obtained with Conventional 120-kVp CT," *Radiology* **259**(1), 257–262 (2011).
- 18 X. Wu *et al.*, "Monochromatic CT Image Representation via Fast Switching Dual kVp," **7258**, (2009).
- 19 M. Karçaaltıncaba and A. Aktaş, "Dual-energy CT revisited with multidetector CT: review of principles and clinical applications.," *Diagn. Interv. Radiol.* **17**(3), 181–94 (2011).
- 20 A.-K. Carton, C. Ullberg, and A.D.A. Maidment, "Optimization of a dual-energy contrast-enhanced technique for a photon-counting digital breast tomosynthesis system: II. An experimental validation," *Med. Phys.* **37**(11), 5908 (2010).
- 21 A.-K. Carton, C. Ullberg, K. Lindman, R. Acciavatti, T. Francke, and A.D.A. Maidment, "Optimization of a dual-energy contrast-enhanced technique for a photon-counting digital breast tomosynthesis system: I. A theoretical model," *Med. Phys.* **37**(11), 5896 (2010).
- 22 A.-K. Carton, S.C. Gavenonis, J. a Currivan, E.F. Conant, M.D. Schnall, and A.D.A. Maidment, "Dual-energy contrast-enhanced digital breast tomosynthesis--a feasibility study.," *Br. J. Radiol.* **83**(988), 344–50 (2010).
- 23 R. Iordache, M. Lohezic, G. Palma, and S. Puong, "Noise Reduction in Dual-Energy Contrast Enhanced Digital Breast Tomosynthesis Using Regularization," *LNCS 6136 IWDM 2010*, 92–99 (2010).
- 24 E. Fredenberg, M. Lundqvist, M. Åslund, M. Hemmendorff, B. Cederström, and M. Danielsson, "A photon-counting detector for dual-energy breast tomosynthesis," **7258**, (2009).
- 25 X. Chen, R.M. Nishikawa, S.-T. Chan, B. a. Lau, L. Zhang, and X. Mou, "Algorithmic scatter correction in dual-energy digital mammography for calcification imaging," **8313**, (2012).
- 26 M.R. Lemacks, S.C. Kappadath, C.C. Shaw, X. Liu, and G.J. Whitman, "A dual-energy subtraction technique for microcalcification imaging in digital mammography—A signal-to-noise analysis," *Med. Phys.* **29**(8), 1739 (2002).
- 27 S.C. Kappadath and C.C. Shaw, "Dual-energy digital mammography for calcification imaging: Scatter and nonuniformity corrections," *Med. Phys.* **32**(11), 3395 (2005).
- 28 S.C. Chen, A.K. Carton, M. Albert, E.F. Conant, M.D. Schnall, and A.D.A. Maidment, "Initial clinical experience with contrast-enhanced digital breast tomosynthesis," *Acad. Radiol.* **14**(2), 229–238 (2008).
- 29 M.I.S. Writers, *Contrast-Enhanced Spectral Mammography Offers Dual-Energy Image Acquisition*, 01 Nov (2011).
- 30 S. Molloy, *Spectral mammography using a photon counting detector provides a unique method for measurements of breast density* (2013).

- 31 E. Fredenberg, M. Lundqvist, B. Cederström, M. Åslund, and M. Danielsson, "Energy resolution of a photon-counting silicon strip detector," *Nucl. Instruments Methods Phys. Res. Sect. A Accel. Spectrometers, Detect. Assoc. Equip.* **613**(1), 156–162 (2010).
- 32 J.M. Lewin, P.K. Isaacs, V. Vance, and F.J. Larke, "Dual-energy contrast-enhanced digital subtraction mammography: feasibility," *Radiology* (January 2002), 261–268 (2003).
- 33 C. Dromain *et al.*, "Dual-energy contrast-enhanced digital mammography: initial clinical results of a multireader, multicase study.," *Breast Cancer Res.* **14**(3), R94 (2012).
- 34 M.S. Jochelson *et al.*, "Bilateral contrast-enhanced dual-energy digital mammography: feasibility and comparison with conventional digital mammography and MR imaging in women with known breast carcinoma.," *Radiology* **266**(3), 743–51 (2013).
- 35 V. Froeling *et al.*, "Correlation of contrast agent kinetics between iodinated contrast-enhanced spectral tomosynthesis and gadolinium-enhanced MRI of breast lesions.," *Eur. Radiol.* **23**(6), 1528–36 (2013).
- 36 B. Ren *et al.*, "Dual energy iodine contrast imaging with mammography and tomosynthesis," **8668**, (2013).
- 37 J.M. Idee, H. Beaufile, and B. Bonnemain, "Iodinated contrast media-induced nephropathy: pathophysiology, clinical aspects and prevention," *Fundam. Clin. Pharmacol.* **8**(3), 193–206 (1994).
- 38 M.R. Zalutsky, M.R. Noska, and S. Steven, "Characterization of liposomes containing iodine-125 labeled radiographic contrast agents," *Investig. Radiol.* **22**(2), 141–7 (1987).
- 39 B. Li, B. Li, J. Luo, P. Tang, J. Mao, and X. Wu, "Simultaneous reduction in noise and cross-contamination artifacts for dual-energy X-ray CT.," *Biomed Res. Int.* **2013**, 417278 (2013).
- 40 R.G. Grainger, "Intravascular contrast media - the past, the present and the future," *Br. J. Radiol.* **55**(649), 1–18 (1982).
- 41 P.M. Hickey and L. McClennan, "Ionic and Nonionic Iodinated Contrast Media:," *Am. J. Roentgenol.* **155**, 225–233 (1990).
- 42 T. Almen, "Contrast agent design: Some aspects on the synthesis of water soluble contrast agents of low osmolality," *J. Theor. Biol.* **24**(2), 216–226 (1969).
- 43 CRC, *Handbook of Chemistry and Physics*, 75th ed. (CRC Press, 1994).
- 44 H. Jönsson, P. Johnsson, P. Höglund, C. Alling, and S. Blomquist, "Elimination of S100B and renal function after cardiac surgery.," *J. Cardiothorac. Vasc. Anesth.* **14**(6), 698–701 (2000).
- 45 B. Olsson, A. Aulie, and K. Sveen, "Human pharmacokinetics of iohexol. A new ionic contrast medium," *Invest. Radiol.* **18**(2), 177–82 (1983).
- 46 W.H. Bush and D.P. Swanson, "Acute Reactions to Intravascular Contrast Media: Types, Risk Factors, Recognition, and Specific Treatment," *Am. J. Roentgenol.* **157**, 1153–1161 (1991).

- 47 J.R. Dillman, P.J. Strouse, J.H. Ellis, R.H. Cohan, and S.C. Jan, "Incidence and severity of acute allergic-like reactions to i.v. nonionic iodinated contrast material in children.," *Am. J. Roentgenol.* **188**(6), 1643–7 (2007).
- 48 C. Brasch, "Allergic Reactions Evidence," *Am. J. Roentgenol.* **134**, 797–801 (1979).
- 49 Center for Disease Control and Prevention, "Influenza vaccination coverage among children with asthma - United States, 2004-05 influenza season," *Morb. Mortal. Wkly. Rep.* **56**(9), 193–6 (2007).
- 50 B.J. Barrett, "Contrast Nephrotoxicity," *J. Am. Soc. Nephrol.* **5**, 125–137 (1994).
- 51 S.K. Morcos, P.W.G. Brown, S. Oldroyd, A.M. Nahas, and J.L. Haylor, "Relationship between the diuretic effect of radiocontrast media and their ability to increase renal vascular resistance," *Br. J. Radiol.* **68**(812), 850–3 (1995).
- 52 S.K. Morcos, F.H. Epstein, J. Haylor, and M. Dobrota, "Aspects of contrast media nephrotoxicity," *Eur. J. Radiol.* **23**(3), 178–184 (1996).
- 53 A. Nordby, K.E. Tvedt, J. Halgunset, and O.A. Haugen, "Intracellular penetration and accumulation of radiographic contrast media in the rat kidney," *Scanning Microscopy* **4**(3), 651–66 (1990).
- 54 M. Brezis, Z. Grenfield, J.J. Herman, S.N. Meyer, S.N. Heyman, and S. Rosen, "Experimental nephrotoxicity of radiocontrast agents iohexol, ioxaglate and iothalamate," *Invest. Radiol.* **26**(4), 325–31 (1991).
- 55 M.R. Rudnick, J.S. Berns, R.M. Cohen, and S. Goldfarb, "Nephrotoxic risks of renal angiography: contrast media-associated nephrotoxicity and atheroembolism - a clinical review," *Am. J. Kidney Dis.* **24**(4), 713–27 (1994).
- 56 S.J. Schwab, M.A. Hlatky, and K.S. Piper, "Contrast nephrotoxicity: a randomized controlled trial of a nonionic and ionic radiographic contrast agent," *N. Engl. J. Med.* **320**(3), 149–53 (1989).
- 57 M.R. Rudnik, S. Goldfarb, and L. Wexler, "Nephrotoxicity of ionic and nonionic contrast media in 1196 patients: a randomized trial," *Kidney Int.* **47**(1), 254–61 (1995).
- 58 L. Byrd and R.L. Sherman, "Radiocontrast-induced acute renal failure: a clinical and pathophysiologica review," *Medicine (Baltimore).* **58**(3), 270–9 (1979).
- 59 E. Samei *et al.*, "Micro-CT imaging of breast tumors in rodents using a liposomal, nanoparticle contrast agent.," *Int. J. Nanomedicine* **4**, 277–82 (2009).
- 60 R. Bhavane *et al.*, "Dual-energy computed tomography imaging of atherosclerotic plaques in a mouse model using a liposomal-iodine nanoparticle contrast agent.," *Circ. Cardiovasc. Imaging* **6**(2), 285–94 (2013).
- 61 J.F. Hainfeld, D.N. Slatkin, T.M. Focella, and H.M. Smilowitz, "Gold nanoparticles: a new X-ray contrast agent.," *Br. J. Radiol.* **79**(939), 248–53 (2006).
- 62 J.F. Hainfeld, M.J. O'Connor, F. a Dilmanian, D.N. Slatkin, D.J. Adams, and H.M. Smilowitz, "Micro-CT enables microlocalisation and quantification of Her2-targeted gold nanoparticles within tumour regions.," *Br. J. Radiol.* **84**(1002), 526–33 (2011).



- 63 O. Rabin, J. Manuel Perez, J. Grimm, G. Wojtkiewicz, and R. Weissleder, "An X-ray computed tomography imaging agent based on long-circulating bismuth sulphide nanoparticles.," *Nat. Mater.* **5**(2), 118–22 (2006).
- 64 E. Roessl and R. Proksa, "K-edge imaging in x-ray computed tomography using multi-bin photon counting detectors.," *Phys. Med. Biol.* **52**(15), 4679–96 (2007).
- 65 A. Abudurexiti *et al.*, "Demonstration of iodine K-edge imaging by use of an energy-discrimination X-ray computed tomography system with a cadmium telluride detector.," *Radiol. Phys. Technol.* **3**(2), 127–35 (2010).
- 66 U. Rode and R. Müller, "Transformation of the ionic X-ray contrast agent diatrizoate and related triiodinated benzoates by *Trametes versicolor*," *Appl. Environ. Microbiol.* **64**(8), 3114–7 (1998).
- 67 L.S. Weisberg, P.B. Kurnik, and B.R. Kurnik, "Risk of radiocontrast nephropathy in patients with and without diabetes mellitus," *Kidney Int.* **45**(1), 259–65 (1994).
- 68 R.G. Cigarroa, R. a Lange, R.H. Williams, and L.D. Hillis, "Dosing of contrast material to prevent contrast nephropathy in patients with renal disease," *Am. J. Med.* **86**(6 Pt 1), 649–52 (1989).
- 69 Z. Liu *et al.*, "Long-circulating Er<sup>3+</sup>-doped Yb<sub>2</sub>O<sub>3</sub> up-conversion nanoparticle as an in vivo X-Ray CT imaging contrast agent," *Biomaterials* **33**(28), 6748–57 (2012).
- 70 Y. Liu, K. Ai, J. Liu, Q. Yuan, Y. He, and L. Lu, "A high-performance ytterbium-based nanoparticulate contrast agent for in vivo X-ray computed tomography imaging," *Angew. Chem. Int. Ed. Engl.* **51**(6), 1437–42 (2012).
- 71 C.-C. Chien *et al.*, "Gold nanoparticles as high-resolution X-ray imaging contrast agents for the analysis of tumor-related micro-vasculature," *J. Nanobiotechnology* **10**(1), 10 (2012).
- 72 N. Lee *et al.*, "Multifunctional Fe<sub>3</sub>O<sub>4</sub> /TaO Core/Shell nanoparticles for simultaneous magnetic resonance imaging and x-ray computed tomography," *J. Am. Chem. Soc.* **134**, 10309–10312 (2012).
- 73 C. Peng *et al.*, "PEGylated dendrimer-entrapped gold nanoparticles for in vivo blood pool and tumor imaging by computed tomography.," *Biomaterials* **33**(4), 1107–19 (2012).
- 74 F.J.P. Richard, P.R. Bakic, A.D.A. Maidment, and S. Member, "Mammogram Registration : A Phantom-Based Evaluation of Compressed Breast," **25**(2), 188–197 (2006).
- 75 M. Wang and M. Thanou, "Targeting nanoparticles to cancer.," *Pharmacol. Res.* **62**(2), 90–9 (2010).
- 76 J. Liu and R.H. Hurt, "Ion release kinetics and particle persistence in aqueous nano-silver colloids.," *Environ. Sci. Technol.* **44**(6), 2169–75 (2010).
- 77 A. Nabikhan, K. Kandasamy, A. Raj, and N.M. Alikunhi, "Synthesis of antimicrobial silver nanoparticles by callus and leaf extracts from saltmarsh plant, *Sesuvium portulacastrum* L.," *Colloids Surf. B. Biointerfaces* **79**(2), 488–93 (2010).
- 78 V.C. Verma, R.N. Kharwar, and A.C. Gange, "Biosynthesis of antimicrobial silver nanoparticles by the endophytic fungus *Aspergillus clavatus*," *Nanomedicine* **5**(1), 33–40 (2010).

- 79 J. Musarrat, S. Dwivedi, B.R. Singh, A.A. Al-Khedhairi, A. Azam, and A. Naqvi, "Production of antimicrobial silver nanoparticles in water extracts of the fungus *Amylomyces rouxii* strain KSU-09.," *Bioresour. Technol.* **101**(22), 8772–6 (2010).
- 80 S. Mehra, M.G. Christoforo, P. Peumans, and A. Salleo, "Solution processed zinc oxide nanopyramid/silver nanowire transparent network films with highly tunable light scattering properties.," *Nanoscale* **5**(10), 4400–3 (2013).
- 81 C. Mustafa and M. Kahraman, "Label-Free Detection of Proteins from Structures using Surface-Enhanced Raman Scattering," **82**(18), 7596–7602 (2010).
- 82 L.Q. Chen *et al.*, "Aptamer-based silver nanoparticles used for intracellular protein imaging and single nanoparticle spectral analysis.," *J. Phys. Chem. B* **114**(10), 3655–9 (2010).
- 83 S.-H. Lee, R. Deshpande, D. Benhammou, P. a. Parilla, a. H. Mahan, and A.C. Dillon, "Metal oxide nanoparticles for advanced energy applications," *Thin Solid Films* **517**(12), 3591–3595 (2009).
- 84 S.-H. Lee, C.E. Tracy, Y. Yan, J.R. Pitts, and S.K. Deb, "Solid-State Nanocomposite Electrochromic Pseudocapacitors," *Electrochem. Solid-State Lett.* **8**(4), A188 (2005).
- 85 B. Yoon and C.M. Wai, "Microemulsion-templated synthesis of carbon nanotube-supported pd and rh nanoparticles for catalytic applications.," *J. Am. Chem. Soc.* **127**(49), 17174–5 (2005).
- 86 Y. Wang, J.Y. Lee, and T.C. Deivaraj, "Tin Nanoparticle Loaded Graphite Anodes for Li-Ion Battery Applications," *J. Electrochem. Soc.* **151**(11), A1804 (2004).
- 87 G. Xi, Y. Peng, W. Yu, and Y. Qian, "Synthesis, characterization, and growth mechanism of tellurium nanotubes," *Cryst. Growth Des.* **5**(1), 325–328 (2005).
- 88 N. Nuraje *et al.*, "Room Temperature Synthesis of Ferroelectric Barium Titanate Nanoparticles Using Peptide Nanorings as Templates," *Adv. Mater.* **18**(6), 807–811 (2006).
- 89 D.S. Brettell and A.R. Cowen, "Dual-energy digital mammography utilizing stimulated phosphor computed radiography.," *Phys. Med. Biol.* **39**(11), 1989–2004 (1994).
- 90 X. Wu and H. Liu, "A new theory of phase-contrast x-ray imaging based on Wigner distributions," *Med. Phys.* **31**(9), 2378 (2004).
- 91 H. Han and M.E. Davis, "Single-Antibody, Targeted Nanoparticle Delivery of Camptothecin.," *Mol. Pharm.* (2013).
- 92 E. Vlashi, L.E. Kelderhouse, J.E. Sturgis, and P.S. Low, "Effect of Folate-Targeted Nanoparticle Size on Their Rates of Penetration into Solid Tumors," *ACS Nano* **7**(10), 8573–8582 (2013).
- 93 C. Fang, B. Shi, Y.-Y. Pei, M.-H. Hong, J. Wu, and H.-Z. Chen, "In vivo tumor targeting of tumor necrosis factor- $\alpha$ -loaded stealth nanoparticles: effect of MePEG molecular weight and particle size.," *Eur. J. Pharm. Sci.* **27**(1), 27–36 (2006).
- 94 L. Cheng, K. Yang, Q. Chen, and Z. Liu, "Organic stealth nanoparticles for highly effective in vivo near-infrared photothermal therapy of cancer.," *ACS Nano* **6**(6), 5605–13 (2012).

- 95 M. Marra *et al.*, “New self-assembly nanoparticles and stealth liposomes for the delivery of zoledronic acid: a comparative study.,” *Biotechnol. Adv.* **30**(1), 302–9 (2012).
- 96 A.D.A. Maidment and R. Karunamuni, “Search for novel contrast materials in dual-energy x-ray breast imaging using theoretical modeling of contrast-to-noise ratio [submitted],” *Phys. Med. Biol.* (n.d.).
- 97 R. Vaidyanathan, S. Gopalram, K. Kalishwaralal, V. Deepak, S.R.K. Pandian, and S. Gurunathan, “Enhanced silver nanoparticle synthesis by optimization of nitrate reductase activity.,” *Colloids Surf. B. Biointerfaces* **75**(1), 335–41 (2010).
- 98 P. Silvert, N. Duvauchelle, V. Vijayakrishnan, and K.T. Elhsissen, “Preparation of colloidal silver dispersions by the polyol process,” *J. Mater. Chem.* **6**(4), 573–577 (1996).
- 99 B. Wiley, T. Herricks, Y. Sun, and Y. Xia, “Polyol Synthesis of Silver Nanoparticles: Use of Chloride and Oxygen to Promote the Formation of Single-Crystal, Truncated Cubes and Tetrahedrons,” *Nano Lett.* **4**(9), 1733–1739 (2004).
- 100 A. Kumar, P.K. Vemula, P.M. Ajayan, and G. John, “Silver-nanoparticle-embedded antimicrobial paints based on vegetable oil.,” *Nat. Mater.* **7**(3), 236–41 (2008).
- 101 A.D. McFarland and R.P. Van Duyne, “Single Silver Nanoparticles as Real-Time Optical Sensors with Zeptomole Sensitivity,” *Nano Lett.* **3**(8), 1057–1062 (2003).
- 102 J.M. Boone, T.R. Fewell, and R.J. Jennings, “Molybdenum, rhodium, and tungsten anode spectral models using interpolating polynomials with application to mammography.,” *Med. Phys.* **24**(12), 1863–74 (1997).
- 103 N.W. Marshall, P. Monnin, H. Bosmans, F.O. Bochud, and F.R. Verdun, “Image quality assessment in digital mammography: part I. Technical characterization of the systems.,” *Phys. Med. Biol.* **56**(14), 4201–20 (2011).
- 104 R. Karunamuni *et al.*, “An Examination of Silver as a Radiographic Contrast Agent in Dual-Energy Breast X-ray Imaging,” *LNCS - IWDM 2012* **7361**, 418–425 (2012).
- 105 E. Navarro *et al.*, “Toxicity of silver nanoparticles to *Chlamydomonas reinhardtii*.,” *Environ. Sci. Technol.* **42**(23), 8959–64 (2008).
- 106 J.S. Kim *et al.*, “Antimicrobial effects of silver nanoparticles.,” *Nanomedicine* **3**(1), 95–101 (2007).
- 107 S. Pal, Y.K. Tak, and J.M. Song, “Does the antibacterial activity of silver nanoparticles depend on the shape of the nanoparticle? A study of the Gram-negative bacterium *Escherichia coli*.,” *Appl. Environ. Microbiol.* **73**(6), 1712–20 (2007).
- 108 C.H.M.W. Wood, R.I.C.P. Layle, and C.H.H. Ogstrand, “Physiology and Modeling of Mechanisms of Silver Uptake and Toxicity in Fish (Annual Review),” *Environ. Toxicol. Chem.* **18**(1), 71–83 (1999).
- 109 S.M. Hussain, K.L. Hess, J.M. Gearhart, K.T. Geiss, and J.J. Schlager, “In vitro toxicity of nanoparticles in BRL 3A rat liver cells.,” *Toxicol. In Vitro* **19**(7), 975–83 (2005).

- 110 C. Graf, D.L.J. Vossen, A. Imhof, and A. van Blaaderen, "A General Method To Coat Colloidal Particles with Silica," *Langmuir* **19**(17), 6693–6700 (2003).
- 111 R. Gref *et al.*, "'Stealth' corona-core nanoparticles surface modified by polyethylene glycol (PEG): influences of the corona (PEG chain length and surface density) and of the core composition on phagocytic uptake and plasma protein adsorption.," *Colloids Surf. B. Biointerfaces* **18**(3-4), 301–313 (2000).
- 112 T. Niidome *et al.*, "PEG-modified gold nanorods with a stealth character for in vivo applications.," *J. Control. Release* **114**(3), 343–7 (2006).
- 113 F. Alexis, E. Pridgen, L.K. Molnar, and O.C. Farokhzad, "Factors Affecting the Clearance and Biodistribution of Polymeric Nanoparticles," *Mol. Pharm.* **5**(4), 505–515 (2008).
- 114 P. Aggarwal, J.B. Hall, C.B. McLeland, M. a Dobrovolskaia, and S.E. McNeil, "Nanoparticle interaction with plasma proteins as it relates to particle biodistribution, biocompatibility and therapeutic efficacy.," *Adv. Drug Deliv. Rev.* **61**(6), 428–37 (2009).
- 115 G. Sonavane, K. Tomoda, and K. Makino, "Biodistribution of colloidal gold nanoparticles after intravenous administration: effect of particle size.," *Colloids Surf. B. Biointerfaces* **66**(2), 274–80 (2008).
- 116 T. Cedervall *et al.*, "Detailed identification of plasma proteins adsorbed on copolymer nanoparticles.," *Angew. Chem. Int. Ed. Engl.* **46**(30), 5754–6 (2007).
- 117 S. Hirn *et al.*, "Particle size-dependent and surface charge-dependent biodistribution of gold nanoparticles after intravenous administration.," *Eur. J. Pharm. Biopharm.* **77**(3), 407–16 (2011).
- 118 J.S. Souris *et al.*, "Surface charge-mediated rapid hepatobiliary excretion of mesoporous silica nanoparticles.," *Biomaterials* **31**(21), 5564–74 (2010).
- 119 A. Al Zaki *et al.*, "Gold-Loaded Polymeric Micelles for Computed Tomography-Guided Radiation Therapy Treatment," *ACS Nano* **8**(1), 104–112 (2014).
- 120 J.M. Tam *et al.*, "Controlled Assembly of Biodegradable Plasmonic Nanoclusters for Near-Infrared Imaging and Therapeutic Applications," **4**(4), (n.d.).
- 121 P. Milioni de Carvalho, A.-K. Carton, S. Saab-Puong, R. Iordache, and S. Muller, "Spectra optimization for dual-energy contrast-enhanced breast CT," **8668**, 86681Z–86681Z–9 (2013).
- 122 P. Monnin, N.W. Marshall, H. Bosmans, F.O. Bochud, and F.R. Verdun, "Image quality assessment in digital mammography: part II. NPWE as a validated alternative for contrast detail analysis.," *Phys. Med. Biol.* **56**(14), 4221–38 (2011).
- 123 M.E. Samberg, S.J. Oldenburg, and N. a Monteiro-Riviere, "Evaluation of silver nanoparticle toxicity in skin in vivo and keratinocytes in vitro.," *Environ. Health Perspect.* **118**(3), 407–13 (2010).
- 124 P. V Asharani, Y. Lian Wu, Z. Gong, and S. Valiyaveetil, "Toxicity of silver nanoparticles in zebrafish models.," *Nanotechnology* **19**(25), 255102 (2008).

- 125 T. Li *et al.*, “Comparative toxicity study of Ag, Au, and Ag-Au bimetallic nanoparticles on *Daphnia magna*,” *Anal. Bioanal. Chem.* **398**(2), 689–700 (2010).
- 126 J.F. Hainfeld, D.N. Slatkin, and H.M. Smilowitz, “The use of gold nanoparticles to enhance radiotherapy in mice,” *Phys. Med. Biol.* **49**(18), N309–N315 (2004).
- 127 G. Zhang *et al.*, “Influence of anchoring ligands and particle size on the colloidal stability and in vivo biodistribution of polyethylene glycol-coated gold nanoparticles in tumor-xenografted mice,” *Biomaterials* **30**(10), 1928–36 (2009).
- 128 D. Kim, S. Park, J.H. Lee, Y.Y. Jeong, and S. Jon, “Antibiofouling polymer-coated gold nanoparticles as a contrast agent for in vivo X-ray computed tomography imaging,” *J. Am. Chem. Soc.* **129**(24), 7661–5 (2007).
- 129 Y. Cao, R. Jin, and C. a Mirkin, “DNA-modified core-shell Ag/Au nanoparticles,” *J. Am. Chem. Soc.* **123**(32), 7961–2 (2001).
- 130 K.K. Sandhu, C.M. McIntosh, J.M. Simard, S.W. Smith, and V.M. Rotello, “Gold nanoparticle-mediated transfection of mammalian cells,” *Bioconjug. Chem.* **13**(1), 3–6 (2002).
- 131 G. Raschke *et al.*, “Biomolecular Recognition Based on Single Gold Nanoparticle Light Scattering,” *Nano Lett.* **3**(7), 935–938 (2003).
- 132 N. Nath and A. Chilkoti, “A colorimetric gold nanoparticle sensor to interrogate biomolecular interactions in real time on a surface,” *Anal. Chem.* **74**(3), 504–9 (2002).
- 133 S. Kühn, U. Håkanson, L. Rogobete, and V. Sandoghdar, “Enhancement of Single-Molecule Fluorescence Using a Gold Nanoparticle as an Optical Nanoantenna,” *Phys. Rev. Lett.* **97**(1), 017402 (2006).
- 134 A.G. Tkachenko *et al.*, “Multifunctional gold nanoparticle-peptide complexes for nuclear targeting,” *J. Am. Chem. Soc.* **125**(16), 4700–1 (2003).
- 135 C.M. Goodman, C.D. McCusker, T. Yilmaz, and V.M. Rotello, “Toxicity of gold nanoparticles functionalized with cationic and anionic side chains,” *Bioconjug. Chem.* **15**(4), 897–900 (2004).
- 136 C.J. Murphy *et al.*, “Gold nanoparticles in biology: beyond toxicity to cellular imaging,” *Acc. Chem. Res.* **41**(12), 1721–30 (2008).
- 137 E.E. Connor, J. Mwamuka, A. Gole, C.J. Murphy, and M.D. Wyatt, “Gold nanoparticles are taken up by human cells but do not cause acute cytotoxicity,” *Small* **1**(3), 325–7 (2005).
- 138 E. Boisselier and D. Astruc, “Gold nanoparticles in nanomedicine: preparations, imaging, diagnostics, therapies and toxicity,” *Chem. Soc. Rev.* **38**(6), 1759–82 (2009).
- 139 Y. Pan *et al.*, “Size-dependent cytotoxicity of gold nanoparticles,” *Small* **3**(11), 1941–9 (2007).
- 140 A.M. Alkilany and C.J. Murphy, “Toxicity and cellular uptake of gold nanoparticles: what we have learned so far?,” *J. Nanopart. Res.* **12**(7), 2313–2333 (2010).

- <sup>141</sup> K.C. Grabar, R.G. Freeman, M.B. Hommer, and M.J. Natan, "Preparation and Characterization of Au Colloid Monolayers," *Anal. Chem.* **67**(4), 1217–1225 (1995).
- <sup>142</sup> M. Brust, M. Walker, D. Bethell, D.J. Schiffrin, and R. Whyman, "Synthesis of Thiol-derivatised Gold Nanoparticles in Two-phase Liquid-Liquid System," *J Chem Soc, Chem Commun.* 801–802 (1994).
- <sup>143</sup> S.L. Westcott, S.J. Oldenburg, T.R. Lee, and N.J. Halas, "Formation and Adsorption of Clusters of Gold Nanoparticles onto Functionalized Silica Nanoparticle Surfaces," *Langmuir* **7463**(12), 5396–5401 (1998).